

UNIVERSITY OF READING

Molecular dynamics study of polymer melts

by

Jing Cao

A thesis submitted in partial fulfillment for the
degree of Doctor of Philosophy

in the

Faculty of Science

Department of Mathematics and Statistics

June 2011

Declaration of Authorship

I, JING CAO, declare that this thesis titled, ‘Molecular dynamics study of polymer melts’ and the work presented in it are my own. I confirm that:

- This work was done wholly or mainly while in candidature for a research degree at this University.
- Where any part of this thesis has previously been submitted for a degree or any other qualification at this University or any other institution, this has been clearly stated.
- Where I have consulted the published work of others, this is always clearly attributed.
- Where I have quoted from the work of others, the source is always given. With the exception of such quotations, this thesis is entirely my own work.
- I have acknowledged all main sources of help.
- Where the thesis is based on work done by myself jointly with others, I have made clear exactly what was done by others and what I have contributed myself.

Signed:

Date:

“Where there is a will , there is a way.”

Thomas Edison

Acknowledgements

This thesis would not have been possible without the essential and gracious support of many individuals. First and foremost I offer my sincerest gratitude to my supervisor, Professor Alexei E. Likhtman, who has supported me throughout my thesis with his patience and knowledge whilst allowing me to work in my own way. Owing to his guidance, a freshman of polymer physics becomes a person who has a basic comprehension of the field. Many thanks to Dr Zuowei Wang for reading my thesis and offering valuable advice. Dr Jorge Ramirez and Dr Bart Vorselaars provided me many useful suggestions of computer programming, which make me work more efficiently. I also need to thank all PhD students in our group, Mohamad Shukor Talib, Tim Palmer, Tom Beardsley, who always have a relaxing chat on physical and non-physical problems. Also thanks Katrina Likhtman to provide homey parties and delicious food. Finally, I thank my parents for supporting me throughout all my studies abroad and never enough thanks to my girl friend, Lei Wang, for listening and supporting.

Contents

Declaration of Authorship	i
Acknowledgements	iii
List of Figures	viii
List of Tables	xiv
Abbreviations	xv
Symbols	xvi
1 Introduction to Molecular Rheology	1
1.1 Overview	1
1.2 Microscopic definition of stress	3
1.3 Strain	4
1.4 Orientation	5
1.5 Viscoelasticity	5
1.5.1 Linear Viscoelasticity	6
1.5.2 Stress relaxation after a step strain	7
1.5.3 The Boltzmann superposition principle	7
1.5.4 Steady shear	8
1.5.5 Oscillatory shear	9
1.6 Brownian motion	11
1.6.1 Random force	12
1.6.2 Friction force	12
1.6.3 Fluctuation-dissipation theorem	13
1.6.4 Langevin equation	15
1.7 Gaussian chains	16
1.7.1 Gaussian chain model	16
1.7.2 Continuous limit	17
1.7.3 Rouse model	18
1.8 Doi-Edwards model of entangled polymers	19

1.8.1	Primitive chain	21
1.8.2	Reptation	22
1.8.3	Contour length fluctuation(CLF)	24
1.8.4	Constraint release(CR)	25
1.9	Microscopic molecular dynamics simulation	25
1.9.1	Periodic boundary condition	26
1.9.2	Pair interactions	27
1.9.3	Equations of motion	28
1.9.4	Other parameters	29
1.10	Motivation	29
2	Orientational relaxation and coupling in equilibrium polymer melts	31
2.1	Overview	31
2.2	Definition of the orientational correlation function	34
2.3	Stress optical law	36
2.4	Monodisperse melts	37
2.4.1	Monomer mean-square displacement	37
2.4.2	Storage and loss moduli	38
2.4.3	Orientational relaxation	40
2.5	Bidisperse melts	42
2.5.1	Monomer mean-square displacement	42
2.5.2	Storage and loss moduli of semi-flexible chains	43
2.5.3	Orientational relaxation	45
2.5.4	End-to-end vector relaxation	48
2.6	Orientational coupling	49
2.6.1	Dumbbell	52
2.6.2	Short-range orientational coupling	54
2.6.3	Time-dependent coupling parameter in flexible systems	55
2.6.4	Coupling effects in monodisperse melts at different densities	56
2.6.5	Coupling effects by entanglements	58
2.6.6	Universality of our coupling parameter	60
2.6.7	Usage of the universal coupling parameter in monodisperse melts	64
2.6.8	Usage of the universal coupling parameter in binary blends	64
2.6.9	Coupling between the coarse-grained blobs	68
2.7	Conclusions	68
3	Microscopic simulations of melts in start-up shear	70
3.1	Overview	70
3.2	Model and algorithms	72
3.2.1	Periodic boundary conditions and equation of motion	72
3.2.2	Thermostat methods	77
3.2.2.1	Andersen method	78
3.2.2.2	Constraint method	78

3.2.2.3	Nosé-Hoover thermostat	79
3.2.2.4	Berendsen thermostat	79
3.2.2.5	Dissipative particle dynamics (DPD) method	79
3.2.3	Steady-state properties from the test run	81
3.2.4	Averaging methods	85
3.3	Monodisperse melts under shear	86
3.3.1	Simulation results	86
3.3.2	Cox-Merz rule	90
3.3.3	Stress-optical law in monodisperse melts	91
3.3.4	Orientation from mean path	93
3.3.5	Configuration of polymer chain in transient state and steady state	93
3.3.6	Comparing semi-flexible chain with the experiments	95
3.4	Conclusions	98
4	Coarse-grained simulation of polymer melts	100
4.1	Overview	100
4.2	Force Projection Method	102
4.3	Rouse model between two walls	103
4.3.1	Microscopic simulation	104
4.3.2	Coarse-grained simulation	106
4.4	Single Kremer-Grest chain between two walls	106
4.5	Kremer-Grest model in vacuum	107
4.5.1	Two chains model	108
4.5.2	Three chains model	110
4.6	Kremer-Grest model in the melt	112
4.6.1	Radius of gyration of chains in systems with different densities	112
4.6.2	Projection force in the systems with different densities	113
4.6.3	Three-body effects in the melt	115
4.6.4	Four-body effects	118
4.7	Coarse-Grained Simulations in Melts	120
4.7.1	Mean field method	120
4.7.2	Vacuum projection force method	121
4.7.3	Melts projection force method	122
4.7.4	Pairwise force plus three-body effects	123
4.8	Conclusions	125
5	Conclusions	127
5.1	Orientation relaxation in monodisperse and bidisperse melts	127
5.2	Start-up shear in the melts	128
5.3	Coarse-grained simulations in the melts	128
A	Normal modes	129

B Percus-Yevick and Hypernetted-chain closure	134
B.1 Ornstein-Zernike equation	134
B.2 Percus-Yevick equation	136
B.3 Hypernetted-chain equation	137
B.4 Coarse-grained simulation by using potentials obtained from PY and HNC closure	138
 Bibliography	 139

List of Figures

1.1	Linear chain conformation.	2
1.2	Microscopic definition of the stress.	2
1.3	Relationship between friction and random forces	15
1.4	Gaussian chain model. The dashed line is bond vectors with unit length.	17
1.5	Rouse model for polymers.	18
1.6	The tube model	20
1.7	The relaxation of the primitive chain.	22
1.8	Periodic boundary condition.	27
2.1	Stress (lines) and orientation (open symbols) relaxation functions in monodisperse melts and their binary blends. The reason of the oscillations of stress relaxation at short times is bond length relaxation.	36
2.2	Stress-optical coefficient α times density ρ as a function of density in flexible(square) and semi-flexible(circle) systems. The results from flexible system are shifted upward by 10 to compare with counterpart of semi-flexible system.	36
2.3	Mean-square displacement of chain ends and middle for flexible chains.	38
2.4	Mean-square displacement of chain ends and middle for semi-flexible chains.	38
2.5	G' of monodisperse melts of flexible chains.	39
2.6	G'' of monodisperse melts of flexible chains.	39
2.7	G' of monodisperse melts of semi-flexible chains.	39
2.8	G'' of monodisperse melts of semi-flexible chains.	39
2.9	$S(t)$ (line), $A(t)$ (open symbol) and $C(t)$ (dashed line) of monodisperse melts of flexible chains.	41
2.10	$S(t)$ (line), $A(t)$ (open symbol) and $C(t)$ (dashed line) of monodisperse melts of semi-flexible chains.	41
2.11	τ_d of flexible and semi-flexible chains as a function of chain lengths.	41
2.12	Cross-correlation functions of flexible chains $N=100$ at different densities.	41
2.13	Mean-square displacement of short(lines) and long(symbols) components in semi-flexible binary blends of $N_1=30$, $N_2=150$	43
2.14	Mean-square displacement of long chains in semi-flexible binary blends with $N_2=150$, $\varphi_l=90\%$	43

2.15	G' of binary blends of semi-flexible chains with $N_1=30, N_2=150$	44
2.16	G'' of binary blends of semi-flexible chains with $N_1=30, N_2=150$ where τ_{ds} and τ_{dl} are terminal time of short and long components respectively.	44
2.17	G' of binary blends of semi-flexible chains with $N_1=75, N_2=150$	45
2.18	G'' of binary blends of semi-flexible chains with $N_1=75, N_2=150$ where τ_{ds} and τ_{dl} are terminal time of short and long components respectively.	45
2.19	Viscosity η_0 as a function of concentration for different binary blends.	45
2.20	Terminal relaxation time τ_d as a function of concentration for different binary blends.	45
2.21	Total orientational relaxation function in binary blends of flexible chains for different compositions.	46
2.22	Total orientational relaxation function in binary blends of semi-flexible chains for different compositions.	46
2.23	All components of orientation relaxation function of binary blend of flexible chains.	47
2.24	All components of orientation relaxation function of binary blend of semi-flexible chains.	47
2.25	$A_s(t)$ (symbols) and $E_s(t)$ (lines) of short chains. Different colours are for different concentrations of the long chains.	47
2.26	$A_l(t)$ (symbols) and $E_l(t)$ (lines) of long chains. Different colours are for different concentrations of the long chains.	47
2.27	End-to-end vector relaxation of short component in binary blends with different conformations. After shifting the data according to Eq.(2.21), all figures collapse onto a master curve(inset).	49
2.28	End-to-end vector relaxation of long component in binary blends with different conformations.	49
2.29	$g(r, \theta)$ of the system with $\rho=0.6\sigma^{-3}$	53
2.30	$g(r, \theta)$ of the system with $\rho=0.85\sigma^{-3}$	53
2.31	$g(r, \theta)$ of the system with $\rho=1.15\sigma^{-3}$	53
2.32	Bonds positions in the simulation box of the system with $\rho = 1.15\sigma^{-3}$	53
2.33	Coupling parameter ε in binary blends of flexible chains.	55
2.34	Coupling parameter ε in binary blends of semi-flexible chains.	55
2.35	Coupling parameter $\kappa(t)$ in monodisperse melts.	56
2.36	Coupling parameter $\kappa(t)$ in bidisperse melts.	56
2.37	Total orientation relaxation function $S(t)$ in monodisperse melts with different densities.	57
2.38	Total orientation relaxation function $S(t)$ in monodisperse melts with different densities.	57
2.39	Coupling parameter $\kappa(t)$ in monodisperse melts with different densities.	57

2.40	Average squared internal distances of the polymer chain in different systems.	59
2.41	Coupling parameter $\kappa(t)$ of soft potential in monodisperse melts. . .	59
2.42	Total relaxation function of orientation in original hard and soft systems.	59
2.43	Mean-square displacement of middle and end monomers of Rouse model and soft systems.	59
2.44	Coupling parameter $\kappa(t)$ of soft potential in monodisperse melts of semi-flexible chains.	60
2.45	Prediction from Eq.(2.30)(lines) and the measured total relaxation(symbols) of binary blend of flexible systems.	60
2.46	Auto-correlation function of long component $A_l(t)$ in binary blends and monodisperse melt.	61
2.47	Components of Cross-correlation functions from simulations(lines) and predictions from Eqs.2.34, 2.31, 2.32(open symbols).	61
2.48	$\kappa(t)$ of flexible and semi-flexible chains.	63
2.49	Total relaxation functions(symbols) and the prediction(lines) of flexible chains from Eq.2.38.	63
2.50	Total relaxation functions(symbols) and the prediction(lines) of semi-flexible chains from Eq.2.38.	63
2.51	Total relaxation functions(symbols) and the prediction(lines) of flexible chains from Eq.2.39.	65
2.52	Total relaxation functions(symbols) and the prediction(lines) of semi-flexible chains from Eq.2.39.	65
2.53	Total relaxation functions(symbols) and the prediction(lines) of flexible chains.	66
2.54	Total relaxation functions(symbols) and the prediction(lines) of semi-flexible chains.	66
2.55	Auto-correlation function $A_l(t)$ of long chains in binary blends(symbols) and solutions(lines).	67
2.56	Total relaxation functions(symbols) and the prediction(lines) of flexible chains.	67
2.57	Coupling parameter $\kappa(t)$ of flexible chains at different coarse-graining level. The starting point $\kappa(0)$ drops from 11% to 3% as the coarse-graining level increases.	67
2.58	Coupling parameter $\kappa(t)$ of semi-flexible chains at different coarse-graining levels.	67
3.1	2-dimensional representation of simulation box vectors. As $t \rightarrow \infty$, $\theta(t) \rightarrow 0$ and $ \mathbf{L}_2 \rightarrow \infty$, whereas $ \mathbf{L}_1 $ remains the same.	75
3.2	Lagrangian-Rhomboid and Sliding-Brick periodic boundary conditions.	76
3.3	Velocity profile of different chain lengths. np is the number of the particles in the system.	82
3.4	Temperature profile of different chain lengths.	82
3.5	Velocity profile of different number of chains.	82

3.6	Temperature profile of different number of chains.	82
3.7	Velocity profile of different shear rate.	82
3.8	Temperature profile of different shear rate.	82
3.9	Velocity profile of different inertial terms.	83
3.10	Temperature profile of different inertial terms.	83
3.11	Velocity profile of different equations of motion.	83
3.12	Temperature profile of different equations of motion.	83
3.13	σ_{xy} and two normal stress in different simulation boxes.	85
3.14	σ_{xy} in one single run and averaged over ten jobs.	85
3.15	Viscosity η in different shear rate $\dot{\gamma}$ for $N=150$	88
3.16	Viscosity η in different shear rate $\dot{\gamma}$ for $N=30$	88
3.17	First normal stress $\sigma_{xx}-\sigma_{yy}$ in different shear rate for $N=150$	88
3.18	First normal stress $\sigma_{xx}-\sigma_{yy}$ in different shear rate for $N=30$	88
3.19	Second normal stress $\sigma_{zz}-\sigma_{yy}$ in different shear rate for $N=150$	88
3.20	Second normal stress $\sigma_{zz}-\sigma_{yy}$ in different shear rate for $N=30$	88
3.21	Shear-stress maximum as a function of $\dot{\gamma}N^2$	89
3.22	Strain at shear-stress maximum as a function of $\dot{\gamma}N^2$	89
3.23	Shear stress σ_{xy} in steady-state as a function of $\dot{\gamma}\eta_0/G_e$, where $G_e=0.073$	89
3.24	First normal stress as a function of $\dot{\gamma}N^2$	89
3.25	Second normal stress as a function of $\dot{\gamma}N^2$	89
3.26	Ratio of first and second normal stresses as a function of $\dot{\gamma}N^2$	89
3.27	$\sigma_{xy}(t)$ of semi-flexible chain with $N=150$ at different shear rates $\dot{\gamma}$	91
3.28	Cox-Merz rule in our simulations. Solid symbols are stress at steady state. lines are complex viscosity times shear rate $\dot{\gamma}$	91
3.29	Stress and orientation relaxation functions in the equilibrium where α called stress-optical coefficient is 1.28.	92
3.30	Stress σ_{xy} (lines) and orientation S_{xy} (symbols) as a function of time at different shear rates, where $\alpha = 1.28$ is the stress-optical coefficient from the equilibrium simulation.	92
3.31	Instantaneous position(a) and mean path(b) of a polymer chain with chain length equal to 150 and bending energy equal to 3.	92
3.32	Orientation from instantaneous positions is compared to the one obtained from mean path.	92
3.33	Configuration of the polymer chain at different state during shear.	94
3.34	The corresponding conformation of the chain during tumbling in steady state at shear rate $\dot{\gamma} = 0.00032\tau^{-1}$	94
3.35	End-to-end vector \mathbf{R}_e of one chain and orientation of the system in shear.	94
3.36	G' , G'' of PI-30k(symbols) in experiment and $N=93$ with $k_b=3$ (lines) in the simulation.	96
3.37	$\tan \delta$ of PI-30k(symbols) in experiments and $N=93$ with $k_b=3$ (lines) in the simulation.	96
3.38	Comparing PI-2k shear experiments(symbols) with $N=7$ simulation results(lines) according to the same Weissenberg number.	97

3.39	Comparing PI-4k shear experiments(symbols) with $N=15$ simulation results(lines) according to the same Weissenberg number. . . .	97
3.40	Comparing PI-14k shear experiments(symbols) with $N=38$ simulation results(lines) according to the same Weissenberg number. . . .	97
3.41	Comparing PI-30k shear experiments(symbols) with $N=93$ simulation results(lines) according to the same Weissenberg number. . . .	97
4.1	The center-of-mass distribution function of the Rouse chain between two walls in microscopic(red line) and coarse-grained(open symbols) simulation.	105
4.2	Projection force function $\mathbf{f}(r)$ of Rouse chain from solid wall in log-linear(left) and linear-linear(right) plots. The line is the best fit data which has the expression as Eq.(4.6).	105
4.3	The center-of-mass distribution function of a Kremer-Grest chain between two walls from microscopic simulation(red line) and from coarse-grained simulation(open symbols).	106
4.4	Magnitude of the projection force function $\mathbf{f}(r)$ of Kremer-Grest chain from solid wall in log-linear plots. The line is the best fit data which has the expression as Eq.(4.8).	106
4.5	Mean square internal distance function of chain length $N = 100$ in vacuum.	108
4.6	Radius of gyration of chains with different lengths in vacuum. . . .	108
4.7	Vacuum projection force for different chain lengths.	109
4.8	Normalized vacuum projection force for different chain lengths. . . .	109
4.9	Three chains model.	110
4.10	$\Delta f_{vac}(r_{12}; x_3, y_3)$ where $r_{12}=0.2\sigma$	111
4.11	$\Delta f_{vac}(r_{12}; x_3, y_3)$ in contour where $r_{12}=0.2\sigma$	111
4.12	$\Delta f_{vac}(r_{12}; x_3, y_3)$ where $r_{12}=1.0\sigma$	112
4.13	$\Delta f_{vac}(r_{12}; x_3, y_3)$ in contour where $r_{12}=1.0\sigma$	112
4.14	$\Delta f_{vac}(r_{12}; x_3, y_3)$ where $r_{12}=2.0\sigma$	112
4.15	$\Delta f_{vac}(r_{12}; x_3, y_3)$ in contour where $r_{12}=2.0\sigma$	112
4.16	$\Delta f_{vac}(r_{12}; x_3, y_3)$ where $r_{12}=3.0\sigma$	112
4.17	$\Delta f_{vac}(r_{12}; x_3, y_3)$ in contour where $r_{12}=3.0\sigma$	112
4.18	Radius gyration as a function of chain lengths.	113
4.19	Radius gyration as a function of density of the system.	113
4.20	Projection force of $N=10$ at different densities.	114
4.21	Normalized projection force of $N=10$ at different densities.	114
4.22	Projection force of $N=20$ at different densities.	114
4.23	Normalized projection force of $N=20$ at different densities.	114
4.24	Shifted normalized projection force of $N=20$ at different densities. . .	115
4.25	Maximum of projection force(solid symbols) and pressure(open symbols) at different densities. Lines are the best fit of the projection force maximum.	115
4.26	$\Delta f_{mel}(r_{12}; x_3, y_3)$ where $r_{12}=0.75\sigma$	116
4.27	$\Delta f_{mel}(r_{12}; x_3, y_3)$ in contour where $r_{12}=0.75\sigma$	116

4.28	$\Delta f_{mel}(r_{12}; x_3, y_3)$ where $r_{12}=1.75\sigma$.	116
4.29	$\Delta f_{mel}(r_{12}; x_3, y_3)$ in contour where $r_{12}=1.75\sigma$.	116
4.30	$\Delta f_{mel}(r_{12}; x_3, y_3)$ where $r_{12}=2.75\sigma$.	117
4.31	$\Delta f_{mel}(r_{12}; x_3, y_3)$ in contour where $r_{12}=2.75\sigma$.	117
4.32	$\Delta f_{mel}(r_{12}; x_3, y_3)$ where $r_{12}=3.75\sigma$.	117
4.33	$\Delta f_{mel}(r_{12}; x_3, y_3)$ in contour where $r_{12}=3.75\sigma$.	117
4.34	$\Delta f_{mel}(r_{12}; x_3, y_3)$ where $r_{12}=4.75\sigma$.	117
4.35	$\Delta f_{mel}(r_{12}; x_3, y_3)$ in contour where $r_{12}=4.75\sigma$.	117
4.36	Three-body correction forces $\Delta f(1.75; x, 0)$ in vacuum and the melts.	118
4.37	Three-body correction forces $\Delta f(2.75; x, 0)$ in vacuum and the melts.	118
4.38	Three-body correction forces $\Delta f(3.75; x, 0)$ in vacuum and the melts.	118
4.39	Three-body correction forces $\Delta f(4.75; x, 0)$ in vacuum and the melts.	118
4.40	Four-body effects in polymer melt.	119
4.41	$g(r)$ obtained from MD simulation and from mean field method in coarse-grained simulation.	119
4.42	$g(r)$ from microscopic(lines) and coarse-grained(open symbols) simulations at different densities with $N=10$ by using vacuum projection force.	121
4.43	$g(r)$ from microscopic(lines) and coarse-grained(open symbols) simulations at different densities with $N=20$ by using vacuum projection force.	121
4.44	$g(r)$ in microscopic(line) and coarse-grained simulations. Square symbols are from mean field method. Circle symbols are from projection force in vacuum. Triangle symbols are from the projection force at $\rho=0.85\sigma^{-3}$.	122
4.45	$g(r)$ in microscopic(line) and coarse-grained simulations with(blue circle) and without(red square) three-body effects from the vacuum.	124
4.46	$g(r)$ in microscopic(line) and coarse-grained simulations with(blue circle) and without(red square) three-body effect from the melt.	124
4.47	$g(r)$ in microscopic(line) and coarse-grained simulations with(blue circle) and without(red square) scaled three-body effects from the melts.	124
4.48	Projection force from pure repulsive Lennard-Jones potential(black line) and attractive Lennard-Jones potential(red line).	124
B.1	$h(r)$ and $c(r)$ of the “blobs” in the system with $\rho = 0.85\sigma^{-3}$.	138
B.2	Direct interaction potential in PY and HNC closure.	138
B.3	$g(r)$ in microscopic simulation, coarse-grained simulation by using vacuum projection force, mean force and the potential obtained from HNC closure.	138

List of Tables

1.1	Summary of the transformation from a discrete system to a continuous variable.	17
2.1	Terminal time τ_d of different chain lengths of flexible and semi-flexible chains.	40
3.1	Mapping between the experiments and the simulations.	95
4.1	Fitting parameter of vacuum projection force for chain length $N=10$ and $N=20$	109

Abbreviations

SDE	Stochastic Differential Equation
RDF	Radial Distribution Function
CLF	Contour Length Fluctuation
CR	Constraint Release
VPF	Vacuum Projection Force
PY	Percus-Yevick
HNC	HyperNetted Chain

Symbols

G	stress relaxation modulus	
\mathbf{R}	monomer position vector	
\mathbf{r}	bond vector	
T	temperature	$^{\circ}C$
m	mass	kg
t	time	s
U	potential	$kg \cdot m^2 / s^2$
σ	stress tensor	$N \cdot m^{-2}$
γ	strain	
η	viscosity	$Pa \cdot s$
ξ	friction coefficient	$N \cdot s / m$
$\dot{\gamma}$	shear rate	s^{-1}
W	Wiesenberg number($\dot{\gamma}\tau$)	

To my family

Chapter 1

Introduction to Molecular Rheology

1.1 Overview

Polymer is a very large molecule which consists of many identical repeating units called segments, which are joined together by very strong covalent bonds. The degree of polymerization is the number of monomers, N , that constitutes the polymer. It is usually a large number, ranging from 10^2 to 10^6 (or even more in some natural polymers). The polymer architecture refers to the topology of the branching structure of the macromolecule. There are many possible types, such as linear, ring, star, comb, dendrimer and randomly branched. A polymer whose repeating units are all the same is called a homopolymer. If there are different types of monomers in the same chain, then it is called heteropolymer. The configuration of a polymer refers to its chemistry, architecture, degree of polymerization and chemical composition in the case of a heteropolymers. It is fixed by chemical reaction and usually cannot change afterwards. The conformation of a polymer refers to the relative location of all its monomers. In this thesis, we concentrate only on linear polymers.

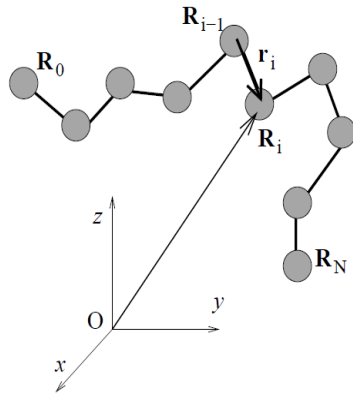


FIGURE 1.1: Linear chain conformation.

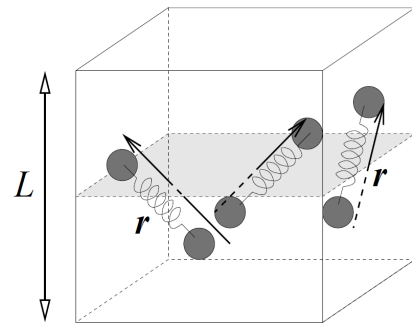


FIGURE 1.2: Microscopic definition of the stress.

The conformation of a linear chain is fully determined if we provide the set of position vectors of all the monomers (Fig. 1.1).

$$\{\mathbf{R}_i\} = (\mathbf{R}_0, \mathbf{R}_1, \dots, \mathbf{R}_N)$$

Alternatively, we can provide the set of bond vectors $\mathbf{r}_i = \mathbf{R}_i - \mathbf{R}_{i-1}$:

$$\{\mathbf{r}_i\} = (\mathbf{r}_1, \mathbf{r}_2, \dots, \mathbf{r}_N)$$

The end-to-end vector is the sum of all N bond vectors in the chain:

$$\mathbf{R}_e = \sum_{i=1}^N \mathbf{r}_i \quad (1.1)$$

And the mean-square end-to-end distance is

$$\begin{aligned} \langle \mathbf{R}_e^2 \rangle &= \left\langle \left(\sum_{i=1}^N \mathbf{r}_i \right) \cdot \left(\sum_{j=1}^N \mathbf{r}_j \right) \right\rangle \\ &= \sum_{i=1}^N \sum_{j=1}^N \langle \mathbf{r}_i \cdot \mathbf{r}_j \rangle \end{aligned} \quad (1.2)$$

which is a normal measure of the linear chain size.

1.2 Microscopic definition of stress

As we know, force can be exerted externally on a body in two particular ways. The gravity and inertia can be thought of as *body forces* since they act directly on all individual particles in the body. The other type are *surface forces* which act only on the surface of a body, but their effect is transmitted to the particles inside the body through the atomic and molecular bonds. In order to define the state of stress at a point within the body we consider the surface forces acting on a small cube of material around that point. We define the **stress** as the ratio of the force and the cross-sectional area. Both the force and the cross-sectional area have direction and magnitude (the direction of the cross-sectional area being described by its normal unit vector), which make the stress a tensor. The $\alpha\beta$ -component of the **stress tensor** is the force applied in the β direction per unit of the cross-sectional area of a network perpendicular to the α axis from outside. In most material the stress tensor is symmetric. We will only consider symmetric stress tensors in this thesis.

$$\boldsymbol{\sigma} = \begin{pmatrix} \sigma_{xx} & \sigma_{xy} & \sigma_{xz} \\ \sigma_{xy} & \sigma_{yy} & \sigma_{yz} \\ \sigma_{xz} & \sigma_{yz} & \sigma_{zz} \end{pmatrix} \quad (1.3)$$

In the consideration of the mechanical properties of the polymers, it is useful to divide the stress tensor into its hydrostatic and deviatoric components. The hydrostatic pressure p is given by

$$p = \frac{1}{3}(\sigma_{xx} + \sigma_{yy} + \sigma_{zz}) \quad (1.4)$$

and the deviatoric stress tensor $\boldsymbol{\sigma}'$ is found by subtracting the hydrostatic stress components from the overall tensor such that

$$\boldsymbol{\sigma}' = \begin{pmatrix} (\sigma_{xx} - p) & \sigma_{xy} & \sigma_{xz} \\ \sigma_{xy} & (\sigma_{yy} - p) & \sigma_{yz} \\ \sigma_{xz} & \sigma_{yz} & (\sigma_{zz} - p) \end{pmatrix} \quad (1.5)$$

The rheological constitutive equations make the predictions of the stress tensor $\boldsymbol{\sigma}$. Now we would like to know how to derive the stress of the system from the microscopic point of view. In Fig.1.2, several dumbbells are placed in a cube of side length L . We can define the component $\alpha\beta$ of the stress tensor as

$$\sigma_{\alpha\beta} = -\frac{1}{V} \sum_i f_i^\alpha R_i^\beta = -\frac{1}{2V} \sum_i \sum_{j \neq i} f_{ij}^\alpha r_{ij}^\beta.$$

where V is the volume of the simulation box, \mathbf{f}_i and \mathbf{R}_i are the force and the position vector of bead i , \mathbf{f}_{ij} and $\mathbf{r}_{ij} = \mathbf{R}_i - \mathbf{R}_j$ are the force and the bond vector from bead j to bead i .

1.3 Strain

When an external force is applied to a material, the atoms change their positions in response to the force and this change is known as *strain*. A simple example is that of a thin rod of material of length l , which is extended a small amount Δl by an externally applied stress. In this case, the strain e could be represented by

$$e = \frac{\Delta l}{l} \tag{1.6}$$

For a general type of deformation consisting of shear, extension and compression in different directions, the situation becomes more complicated. Namely the strain tensor is defined as

$$E_{\alpha\beta} = \frac{1}{2} \left(\frac{\partial u_\alpha}{\partial x_\beta} + \frac{\partial u_\beta}{\partial x_\alpha} \right) \tag{1.7}$$

where α, β are the Cartesian coordinates and \mathbf{u} is the displacement vector. The shear rate tensor κ is defined as

$$\kappa_{\alpha\beta} = \frac{1}{2} \left(\frac{\partial v_\alpha}{\partial x_\beta} + \frac{\partial v_\beta}{\partial x_\alpha} \right) \tag{1.8}$$

where \mathbf{v} is the velocity of moving plates.

1.4 Orientation

During the deformation of the material, chain bonds may orient themselves in the draw direction. The **degree of the orientation** is often difficult to measure and the distribution of the orientation is usually impossible to determine in experiments. The orientation can be measured by the velocity of the sound, infrared dichroism, X-ray wide angle measurements, or optical birefringence. The **uniaxial order parameter** $q_{orient} = (3\langle \cos^2 \beta \rangle - 1)/2$ is calculated from the orientation angle β , which is defined as the angle between the draw direction and the main optical axis. The order parameter becomes unity for a complete orientation in the draw direction ($\beta = 0^\circ$), $-\frac{1}{2}$ for a complete orientation perpendicular to the draw direction ($\beta = 90^\circ$), and zero corresponds to a completely random or isotropic distribution of molecular orientation.

The orientation in transparent materials can also be characterized by **optical birefringence**. A transparent material exhibits refractive indices n_x , n_y and n_z along the three main axes x , y and z . At least two of these refractive indices are different for optical anisotropic materials. The difference between any two of these refractive indices is called the **birefringence** Δn . The polymer solutions or melts are isotropic at equilibrium. Once an external field is applied to the system, the statistical distribution of the polymers deviates from isotropic, and the optical properties of the material become anisotropic. The birefringence of polymer solutions has two origins. First, orientation of bond vectors of the main chain causes birefringence, called **intrinsic birefringence**. Second, the anisotropy of the shape of the polymer coil creates an anisotropic internal field, which is called **form birefringence**[\[1\]](#).

1.5 Viscoelasticity

A distinctive feature of mechanical behaviour of polymers is the way in which their response to an applied stress or strain depends upon the deformation rate and the

history. This dependence is in remarkable contrast to the behaviour of elastic solids such as metals and ceramics which, at least at low strains, obey the *Hooke's Law*: $\sigma = GE$ meaning the stress is proportional to the strain and independent of the loading rate, where E is the deformation gradient tensor. On the other hand, the mechanical behaviour of viscous liquids is time-dependent. It is possible to represent their behaviour at low rates of strain by *Newton's Law* whereby the stress is proportional to the strain rate and independent of the strain $\sigma = \eta\kappa$. The behaviour of most polymers is in between that of elastic solids and viscous liquids, and the polymer response to the deformation can be divided into elastic and viscous contributions.

1.5.1 Linear Viscoelasticity

Consider the deformation geometry of simple shear where material is sandwiched between two plates perpendicular to y direction. The adhesion between the material and the surfaces is assumed to be strong enough so that there is no slippage at either surface. The bottom surface is held so that it does not move, and the upper surface is free to move in x direction, apart from the fact that the material between the surfaces may resist that motion. The shear stress σ_{xy} in this simple shear is defined as the ratio of the applied force f_x and the cross-sectional area of the surface A_y , which is also the area of any plane perpendicular to the y direction within the material being sheared: $\sigma_{xy} = f_x/A_y$. The shear strain γ is defined as the displacement of the top plate Δx relative to the thickness of the sample h : $\gamma = \Delta x/h$. If the material between the surfaces is a perfectly elastic solid, the shear stress σ_{xy} and strain γ are proportional. The ratio is defined as **shear modulus** $G = \sigma_{xy}/\gamma$. On the other hand, if the material between the surfaces is a simple liquid, the stress is identically zero at any constant strain γ . In liquids, the stress is determined by the deformation rate $\dot{\gamma} = d\gamma/dt$. For simple liquids, the shear stress σ_{xy} is linearly proportional to shear rate $\dot{\gamma}$. The **shear viscosity** is defined as

$$\eta = \frac{\sigma_{xy}}{\dot{\gamma}} \quad (1.9)$$

The simplest model of viscoelasticity is the **Maxwell model**[1], which combines a perfectly elastic element with a perfectly viscous element in series. Since the elements are in series, the total shear strain γ is the sum of the shear strain in each element $\gamma = \gamma_e + \gamma_v$, both of the elements must bear the same stress $\sigma = G\gamma_e = \eta \frac{d\gamma_v}{dt}$. The ratio of the viscosity η and the modulus G defines characteristic time scale, called the relaxation time $\tau = \eta/G$.

1.5.2 Stress relaxation after a step strain

When a step strain was applied at time $t = 0$, the stress relaxation modulus $G(t)$ is defined as the ratio of the stress remaining at time t and the magnitude of this step strain γ : $G(t) = \sigma(t)/\gamma$. For viscoelastic solids, $G(t)$ relaxes to a finite value, called the **equilibrium shear modulus** $G_{eq} = \lim_{t \rightarrow \infty} G(t)$. For viscoelastic liquids, the Maxwell model can be used to understand the stress relaxation modulus. After solving a first order differential equation of the time-dependent strain in the viscous element, the stress relaxation modulus in this case has a simple exponential decay:

$$G(t) = \frac{\sigma(t)}{\gamma} = G_0 \exp(-t/\tau) \quad (1.10)$$

The relaxation time τ is a fundamental dynamic property of all viscoelastic liquids. Polymer liquids normally have multiple relaxation modes, each with its own relaxation time. Any stress relaxation modulus can be described by a combination of serial Maxwell elements. Most materials have a region of **linear response** at sufficiently small values of applied strain, where the relaxation modulus is independent of strain.

1.5.3 The Boltzmann superposition principle

The Boltzmann superposition principle states that the stress from any combination of small step strains is simply the linear combination of stresses resulting from each

individual step $\delta\gamma_i$ applied at time t_i .

$$\sigma(t) = \sum_i G(t - t_i)\delta\gamma_i \approx \sum_i G(t - t_i)\dot{\gamma}_i\delta t_i \quad (1.11)$$

where $\dot{\gamma}_i$ is constant. In other words, the system remembers the deformations that were imposed on it earlier, and continues to relax from each earlier deformation as the new ones are applied. The stress from any smooth strain history can be written as an integral over the strain history.

$$\sigma(t) = \int_{-\infty}^t G(t - t')\dot{\gamma}(t')dt' \quad (1.12)$$

The stress in viscoelastic material is the result of all past deformations. The memory of each past deformation only decays as the relaxation modulus decays over the elapsed time $t - t'$ from the application of that deformation.

1.5.4 Steady shear

In steady shear, the shear rate $\dot{\gamma}$ is a time-independent constant that can be taken out of the Boltzmann superposition integral:

$$\sigma(t) = \dot{\gamma} \int_0^t G(t - t')dt' = \dot{\gamma} \int_0^t G(s)ds \quad (1.13)$$

$$\sigma_{ss} = \lim_{t \rightarrow +\infty} \sigma(t) \quad (1.14)$$

where σ_{ss} is the steady state stress. The relaxation modulus $G(t)$ eventually decays to zero fast enough that the integral is finite for any liquid. Thus the stress at long times in steady shear is constant, and proportional to the shear rate $\dot{\gamma}$. Newton's law of viscosity(Eq.1.9) defined the viscosity in steady shear as the ratio of shear stress and shear rate. Therefore, the viscosity of any liquid in the linear regime is the integral of its stress relaxation modulus:

$$\eta = \int_0^{\infty} G(t)dt. \quad (1.15)$$

If the applied shear rate is too large for linear response, Boltzmann superposition no longer holds. Most polymeric liquids exhibit **shear thinning** of the apparent viscosity at large shear rates, which means that the viscosity decreases with increasing the shear rate. The apparent viscosity has also been observed to increase with the shear rate increase for some materials, which is called **shear thickening**.

1.5.5 Oscillatory shear

In practice, the simplest linear viscoelastic measurement is oscillatory shear[2]. A harmonic oscillation of strain with angular frequency ω is applied to a sample in simple shear: $\gamma(t) = \gamma_0 \cos(\omega t)$. The principal advantage of this technique is that the viscoelastic response of any material can be probed directly on different time scale of interest $t \approx 1/\omega$ by varying the angular frequency ω . If the material studied is a perfectly elastic solid, then the stress in the sample will be related to the strain through Hooke's law:

$$\sigma(t) = G_0 \gamma_0 \cos(\omega t). \quad (1.16)$$

The stress in this case is perfectly in-phase with the strain. On the other hand, if the material is a Newtonian liquid, the stress in the liquid will be related to the shear rate through Newton's law:

$$\sigma(t) = \eta \frac{d\gamma(t)}{dt} = -\eta \gamma_0 \omega \sin(\omega t) = \eta \gamma_0 \omega \cos(\omega t + \frac{\pi}{2}). \quad (1.17)$$

More generally, the linear response of a viscoelastic material consists of the stress oscillations at the same frequency as the applied strain, but the stress leads the strain by a phase angle δ

$$\sigma(\omega, t) = \sigma_0(\omega) \cos(\omega t + \delta).$$

By using Boltzmann superposition integral(Eq.1.12),

$$\begin{aligned}
\sigma(\omega, t) &= \int_{-\infty}^t G(t-t')\dot{\gamma}(t')dt' \\
&= - \int_{-\infty}^t G(t-t')\gamma_0\omega \sin(\omega t')dt' \\
&= \mathbf{Re} \left[\int_{-\infty}^t G(t-t')\gamma_0\mathbf{i}\omega \exp(\mathbf{i}\omega t')dt' \right] \\
&= \mathbf{Re} [\gamma_0 G^*(\omega) \exp(\mathbf{i}\omega t)]
\end{aligned} \tag{1.18}$$

where the **complex modulus** $G^*(\omega)$ is defined by:

$$G^*(\omega) = \mathbf{i}\omega \int_0^{\infty} G(t) \exp(-\mathbf{i}\omega t) dt \tag{1.19}$$

The form of Eq.(1.18) means that the stress will also be oscillatory at frequency ω , but not in phase with the strain. If we write $G^*(\omega) = G'(\omega) + \mathbf{i}G''(\omega)$, then we can identify the real part G' , called the storage modulus, as the in-phase part of the modulus and the imaginary part G'' , called loss modulus, as the out-of-phase part. Assume $G(t) \rightarrow 0$ as $t \rightarrow +\infty$.

$$G'(\omega) = \omega \int_0^{\infty} G(t) \sin(\omega t) dt \tag{1.20}$$

$$G''(\omega) = \omega \int_0^{\infty} G(t) \cos(\omega t) dt \tag{1.21}$$

In general both will be frequency-dependent, crossing over from viscous behavior at low frequencies to elastic behavior at high frequencies. Then Eq.(1.18) can be written as following:

$$\begin{aligned}
\sigma(\omega, t) &= \mathbf{Re} [\gamma_0 G^*(\omega) \exp(\mathbf{i}\omega t)] \\
&= \mathbf{Re} [\gamma_0 (G'(\omega) + \mathbf{i}G''(\omega)) (\cos(\omega t) + \mathbf{i} \sin(\omega t))] \\
&= \gamma_0 (G'(\omega) \cos(\omega t) - G''(\omega) \sin(\omega t))
\end{aligned} \tag{1.22}$$

According to Eq.(1.17) and Eq.(1.22), the ideal Newtonian fluids have a shear stress that is simply proportional to the current shear rate.

$$\sigma(t) = \eta \frac{\partial \gamma}{\partial t} = \mathbf{Re} [\eta i \omega \gamma_0 \exp(i \omega t)] \Rightarrow \begin{cases} G'(\omega) = 0 \\ G''(\omega) = \eta \omega \end{cases} \quad (1.23)$$

At the opposite material extreme, the ideal elastic solids have a shear stress that is simply proportional to the current shear strain.

$$\sigma(t) = G_0 \gamma = G_0 \gamma_0 \mathbf{Re} [\exp(i \omega t)] \Rightarrow \begin{cases} G'(\omega) = G_0 \\ G''(\omega) = 0 \end{cases} \quad (1.24)$$

For the single Maxwell model of a viscoelastic fluid $G(t) = G_0 \exp(-t/\tau)$, the integral over $G(t)$ can be done exactly to obtain

$$G'(\omega) = G_0 \frac{\omega^2 \tau^2}{1 + \omega^2 \tau^2}$$

$$G''(\omega) = G_0 \frac{\omega \tau}{1 + \omega^2 \tau^2}$$

Until now we introduced some macroscopic variables in polymer physics according to experimental measurements. Later we would like to introduce some microscopic variables which give rise to those macroscopic phenomenons.

1.6 Brownian motion

Originally, Brownian motion term was used to describe the random motion of particles suspended in a fluid. It was first observed by Robert Brown in 1827, while studying the motion of pollen particles floating in water under the microscope. The particles in suspension are much bigger than the molecules of the fluid. The small molecules hit the Brownian particles at different times in all possible directions with different forces, resulting in a random motion of the particles. The dynamics

of the Brownian particles are governed by Newton's law: $\mathbf{f} = m\mathbf{a} = m\ddot{\mathbf{r}}$, where \mathbf{a} is the acceleration vector of the particle. \mathbf{f} represents the forces acting on the particle, which can be divided in random force \mathbf{f}_R and friction force \mathbf{f}_F . Note that now the Brownian motion term is used to describe the random motion of molecules and atoms as well.

1.6.1 Random force

The random force \mathbf{f}_R acting on a particle is due to many collisions with the other molecules surrounding it. The collisions take place very fast and are unpredictable in nature, so we will consider each of them, \mathbf{f}_{Ri} , to take place in a random direction and with a random amplitude. We are interested in the accumulated effect of these collisions, so that $\mathbf{f}_R = \sum_{i=1}^{N_i} \mathbf{f}_{Ri}$, where N_i is the number of collisions related to a particle i . If \mathbf{f}_{Ri} are independent of each other, by the central limit theorem the probability distribution of \mathbf{f}_R must be Gaussian. By symmetry, $\langle \mathbf{f}_R \rangle = \mathbf{0}$. We assume that the distribution has a variance σ^2 , and the random forces \mathbf{f}_R at different moments of time t and t' are uncorrelated. The diffusion of a particle caused by random force can be modelled by Wiener process

$$\mathbf{f}_R dt = \sigma d\mathbf{W} \quad (1.25)$$

where $d\mathbf{W}$ is differential of a Wiener process[3].

1.6.2 Friction force

The friction forces are due to the resistance felt by the Brownian particle in its motion through the sea of small molecules. This friction is also produced by the continuous collisions between the particle and the small molecules, so it has a similar origin as the random forces. The friction force can be considered to be proportional to the velocity vector \mathbf{v} of the particle. The amplitude of the friction force divided by velocity is referred to as the friction coefficient ξ . Therefore, we

have

$$\mathbf{f}_F = -\xi \mathbf{v} = -\xi \frac{d\mathbf{r}}{dt} \quad (1.26)$$

1.6.3 Fluctuation-dissipation theorem

Consider a time-dependent external field $h(t)$ is applied to a system in equilibrium. A physical observable A is called conjugate to the field h if the change of Hamiltonian due to the field h can be written as $\Delta H = hA$. If the field is weak, the change in physical quantity $A(t)$ conjugate to the field $h(t)$ is a linear function of the field.

$$\langle A(t) \rangle_h - \langle A_0 \rangle = \int_{-\infty}^t \mu(t-t') h(t') dt' \quad (1.27)$$

where $\langle A(t) \rangle_h$ is the value of A at time t when the field is applied, $\langle A_0 \rangle$ is the equilibrium value of A without the field and $\mu(t)$ is called the response function. This is a more general statement of the Boltzmann superposition principle (Eq. 1.12). The response function is related to the time correlation function of $A(t)$ by

$$\mu(t) = -\frac{1}{k_B T} \frac{d}{dt} C_{AA}(t) \quad (1.28)$$

which is called the fluctuation-dissipation theorem, where T is the temperature, k_B is the Boltzmann constant and $C_{AA}(t) = \langle A(t+t')A(t') \rangle$ averaged over t' and over ensemble without any external field.

If we consider the situation that a constant field h is applied for a long time until the system reaches steady state and then the field is switched off at $t = 0$, Eq.(1.27) turns into

$$\langle A(t) \rangle_h - \langle A_0 \rangle = h \int_t^{+\infty} \mu(t') dt' \quad (1.29)$$

From Eqs.(1.28) and (1.29), we can derive

$$\langle A(t) \rangle_h - \langle A_0 \rangle = h \frac{1}{k_B T} (C_{AA}(t) - C_{AA}(+\infty)) \quad (1.30)$$

On the other hand, if we apply a sudden step field on an equilibrium system at $t=0$, Eq.(1.27) turns into

$$\langle A(t) \rangle_h - \langle A_0 \rangle = h \int_0^t \mu(t') dt' \quad (1.31)$$

From Eqs.(1.28) and (1.31), we can derive

$$\langle A(t) \rangle_h - \langle A_0 \rangle = \frac{h}{k_B T} (C_{AA}(0) - C_{AA}(t)) \quad (1.32)$$

$$= \frac{h}{2k_B T} \langle (A(t) - A(0))^2 \rangle \quad (1.33)$$

The fluctuation-dissipation theorem connects the relaxation from a non-equilibrium state, which is not far from the equilibrium state, i.e. in linear regime, with the spontaneous microscopic dynamics in the equilibrium system.

So far, we have the following expression for the forces acting on the Brownian particles:

$$\mathbf{f}(t)dt = (\mathbf{f}_R(t) + \mathbf{f}_F(t))dt = \sigma d\mathbf{W} - \xi d\mathbf{r} \quad (1.34)$$

It is usual to work in the limit of strong friction where inertia term $m\ddot{\mathbf{r}}$ can be neglected, and therefore the above equation can be simplified to

$$\xi d\mathbf{r} = \sigma d\mathbf{W} \quad (1.35)$$

The fluctuation-dissipation theorem establishes a relationship between the random forces and the friction forces so that the right distribution is recovered when a dynamic system is governed by Brownian motion. It provides a direct relation between the amplitude of the random force σ and the amplitude of the friction force ξ . If the particle is stationary in space in average (Fig.1.3 left), the probability of collision with small molecules is the same from all directions. However, if the particle moves to the right (Fig.1.3 right), the probability of random collisions with molecules coming from the right is higher, and this gives rise to a higher friction force which opposes the motion of the particle. Because the two types of the forces have the same origin, there must be a relationship between them.

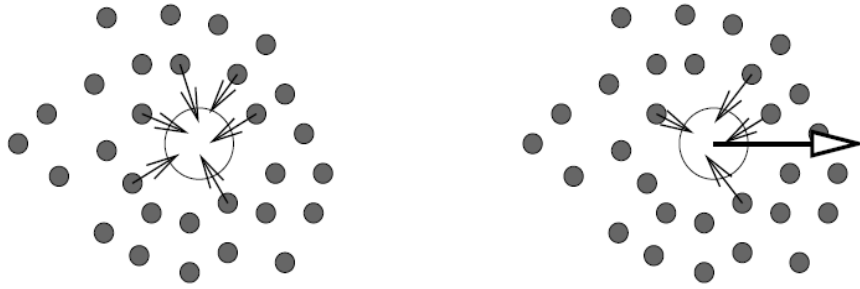


FIGURE 1.3: Relationship between friction and random forces

From Eq.(1.33) and the property of Wiener process in one-dimension $\langle (d\mathbf{r})^2 \rangle = 2D dt$ where $d\mathbf{r}$ is the displacement of the particle during dt and D is the diffusion coefficient, the following equation can be derived using $h = \mathbf{f}$ and $A = \mathbf{r}$

$$\langle d\mathbf{r} \rangle = \frac{\mathbf{f}}{2k_B T} \langle (d\mathbf{r})^2 \rangle = \frac{\mathbf{v}\xi}{2k_B T} 2D dt \quad (1.36)$$

$$\Rightarrow D = \frac{k_B T}{\xi}. \quad (1.37)$$

Eq.(1.37) is called the Einstein formula. Then the amplitudes σ and ξ have the following temperature dependent relationship given by the fluctuation-dissipation theorem:

$$\sigma^2 = 2k_B T \xi \quad (1.38)$$

Following from Eq.(1.35) we obtain the evolution equation for the Brownian particles:

$$\xi d\mathbf{r} = \sqrt{2k_B T \xi} d\mathbf{W} \quad (1.39)$$

1.6.4 Langevin equation

The simplest polymer model is a single chain model, where Newton's equation of motion for each monomer include regular forces due to interaction with other monomers of the same chain, as well as random and friction forces due to interaction with the surrounding media:

$$m \frac{d^2 \mathbf{R}_i}{dt^2} = - \frac{\partial U(\{\mathbf{R}_i\})}{\partial \mathbf{R}_i} dt - \xi d\mathbf{R}_i + \sqrt{2k_B T \xi} d\mathbf{W}_i \quad (1.40)$$

where ξ is the friction coefficient, m is the monomer mass, $U(\{\mathbf{R}_i\})$ is the intra-chain interaction potential, and \mathbf{W}_i is a Wiener process for particle i .

1.7 Gaussian chains

1.7.1 Gaussian chain model

In the Gaussian chain model, we forget about the local details of the chain, and assume that every bond \mathbf{r}_i is actually the sum of many bond vectors, so that the probability distribution of \mathbf{r}_i is Gaussian. The assumption is that the different bonds along the chain are independent of each other, $\langle \mathbf{r}_i \cdot \mathbf{r}_j \rangle = \langle \mathbf{r}_i \rangle \cdot \langle \mathbf{r}_j \rangle$ if $i \neq j$. The bond length is not constant. Each bond is flexible and follows a Gaussian distribution:

$$p(\mathbf{r}) = \left(\frac{3}{2\pi b^2} \right)^{\frac{3}{2}} \exp \left(-\frac{3\mathbf{r}^2}{2b^2} \right) \quad (1.41)$$

with $\langle \mathbf{r} \rangle = 0$ and $\langle \mathbf{r}^2 \rangle = b^2$. The probability distribution of a given conformation $\{\mathbf{r}_i\} = \{\mathbf{r}_1, \dots, \mathbf{r}_N\}$ is:

$$\Psi(\{\mathbf{r}_i\}) = \prod_{i=1}^N p(\mathbf{r}_i) = \left(\frac{3}{2\pi b^2} \right)^{\frac{3N}{2}} \exp \left(-\frac{3}{2b^2} \sum_{i=1}^N \mathbf{r}_i^2 \right) \quad (1.42)$$

It has an important property that the distribution function of the vector between any two beads of the Gaussian chain is also Gaussian with $\langle \mathbf{R}_i - \mathbf{R}_j \rangle = 0$ and $\langle (\mathbf{R}_i - \mathbf{R}_j)^2 \rangle = |i - j|b^2$.

$$p(\mathbf{R}_i - \mathbf{R}_j) = \left(\frac{3}{2\pi b^2 |i - j|} \right)^{\frac{3}{2}} \exp \left(-\frac{3(\mathbf{R}_i - \mathbf{R}_j)^2}{2|i - j|b^2} \right) \quad (1.43)$$

In Eq.(1.43), if we set $i = N$ and $j = 0$, the equation turns into

$$p(\mathbf{R}_N - \mathbf{R}_0) = p(\mathbf{R}_e) = \left(\frac{3}{2\pi N b^2} \right)^{\frac{3}{2}} \exp \left(-\frac{3\mathbf{R}_e^2}{2N b^2} \right) \quad (1.44)$$

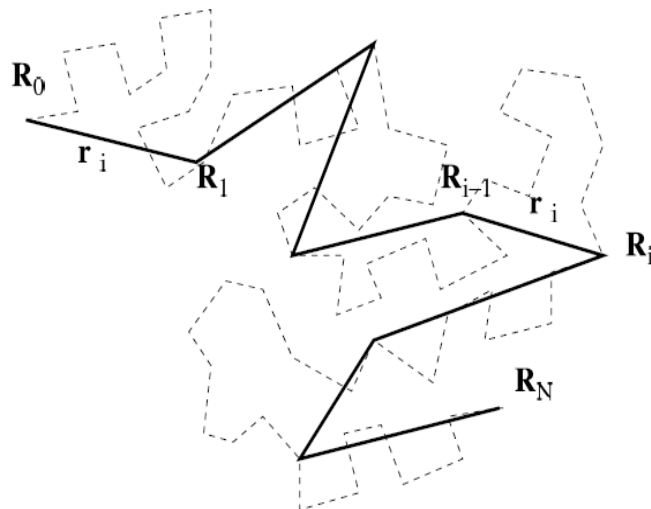


FIGURE 1.4: Gaussian chain model. The dashed line is bond vectors with unit length.

The Gaussian chain model does not describe the local structure of the polymer correctly. However, it does correctly describe the properties on large length-scales if the excluded volume and other non-bonded interactions can be neglected. The advantage of the Gaussian chain model is that it is mathematically much easier to handle than any other models. However, the Gaussian chain model has no mechanism to prevent monomers from passing through each other.

1.7.2 Continuous limit

Sometimes it is more convenient to describe a chain contour by using continuous variables instead of using a set of discrete variables. When describing a Rouse chain by a set of N beads, the system should be independent of the number of beads. Here are notations used in discrete and continuous formats respectively:

Discrete		Continuous
\mathbf{R}_n	\Rightarrow	$\mathbf{R}(n)$
$\mathbf{R}_n - \mathbf{R}_{n-1}$	\Rightarrow	$\frac{\partial \mathbf{R}}{\partial n}$
$\mathbf{R}_{n+1} + \mathbf{R}_{n-1} - 2\mathbf{R}_n$	\Rightarrow	$\frac{\partial^2 \mathbf{R}}{\partial n^2}$
δ_{nm}	\Rightarrow	$\delta(n - m)$
$\sum_{n=m}^{m'}$	\Rightarrow	$\int_m^{m'} dn$

TABLE 1.1: Summary of the transformation from a discrete system to a continuous variable.

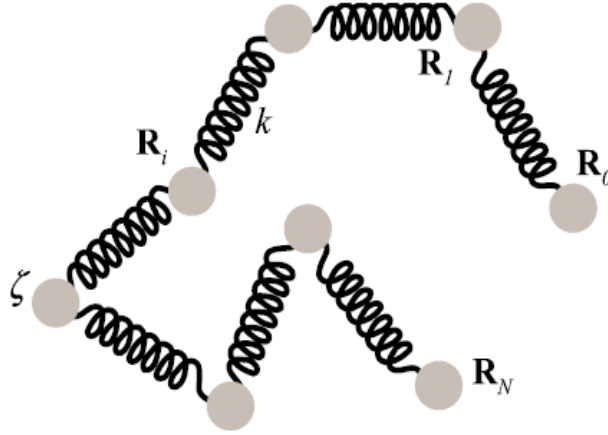


FIGURE 1.5: Rouse model for polymers.

1.7.3 Rouse model

Rouse model, which is a cornerstone of polymer dynamics, was originally proposed by Rouse[4] in 1953. The model is treated as a collection of $N + 1$ beads connected by harmonic springs(Fig.1.5), which is defined by the equation of motion Eq.(1.40) without inertia with the simplest possible potential

$$U(\{\mathbf{R}_i\}) = \frac{3k_B T}{2b^2} \sum_{i=0}^{N-1} (\mathbf{R}_{i+1} - \mathbf{R}_i)^2 \quad (1.45)$$

Each bead is characterized by its own independent friction force with the friction coefficient ξ . The total friction coefficient of the whole Rouse chain is the sum of the contributions of each of the $N + 1$ beads: $\xi_{chain} = (N + 1)\xi$. We can write the stochastic differential equation for each bead along the chain:

$$\xi d\mathbf{R}_0 = \frac{3k_B T}{b^2} (\mathbf{R}_1 - \mathbf{R}_0) dt + \sqrt{2k_B T \xi} d\mathbf{W}_{t0} \quad (1.46)$$

$$\vdots = \vdots$$

$$\xi d\mathbf{R}_i = \frac{3k_B T}{b^2} (\mathbf{R}_{i+1} + \mathbf{R}_{i-1} - 2\mathbf{R}_i) dt + \sqrt{2k_B T \xi} d\mathbf{W}_{ti} \quad (1.47)$$

$$\vdots = \vdots$$

$$\xi d\mathbf{R}_N = \frac{3k_B T}{b^2} (\mathbf{R}_{N-1} - \mathbf{R}_N) dt + \sqrt{2k_B T \xi} d\mathbf{W}_{tN} \quad (1.48)$$

where \mathbf{W}_{ti} is a vector Wiener processes in terms of the bead number i :

$$\begin{aligned}\langle \mathbf{W}_{ti} \rangle &= \mathbf{0} \\ \langle W_{ti\alpha} W_{t'j\beta} \rangle &= \delta_{ij} \delta_{\alpha\beta} \min(t, t') \\ \langle \mathbf{W}_{ti} \cdot \mathbf{W}_{t'j} \rangle &= 3\delta_{ij} \min(t, t')\end{aligned}$$

In the continuous limit, the above equations can be rewritten as following:

$$\xi \frac{\partial \mathbf{R}(n)}{\partial t} = k \frac{\partial^2 \mathbf{R}(n)}{\partial n^2} + \mathbf{f}_n \quad (1.49)$$

$$\left. \frac{\partial \mathbf{R}(n)}{\partial n} \right|_{n=0} = 0, \quad \left. \frac{\partial \mathbf{R}(n)}{\partial n} \right|_{n=N} = 0 \quad (1.50)$$

where $k = 3k_B T / b^2$ and \mathbf{f}_n is a random force obeying $\langle \mathbf{f}_n \rangle = 0$, $\langle \mathbf{f}_n(t) \cdot \mathbf{f}_{n'}(t') \rangle = \delta(n - n') \delta(t - t') 6k_B T \xi$. More details about Rouse modes are given in Appendix A.

1.8 Doi-Edwards model of entangled polymers

The viscosity of various linear polymer melts as a function of molecular weight were measured by Berry *et al.*[5] and Colby *et al.*[6]. A transition behaviour of viscosity was found at some critical molecular weight M_c . The viscosity is a linear function of the molecular weight with the slope = 1 below M_c . Above the threshold, the slope increases to approximately 3.4. The tube model, which was proposed and developed by de Gennes[7], Doi and Edwards[8], is usually used to describe polymer dynamics of chains longer than M_c in concentrated solutions and melts. The observed change in scaling behaviour is due to the surrounding chains around the probe single chain, which prevent the probe chain to cross other surrounding chains. Instead of solving a many-body problem of the entangled system, the tube model adopts a mean-field method and reduces the problem to a single chain model. The topological interactions are modelled as a set of obstacles that confine the probe chain in a tube-like region. This tube allows the probe

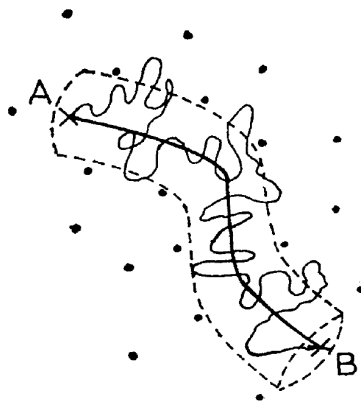


FIGURE 1.6: The tube model

chain to move freely along its own contour length but not perpendicular to its contour(Fig.1.6). A piece of chain which escaped from the tube is assumed to adopt a random orientation independent of surrounding chains. Merrill *et al.*[9] demonstrated that if this assumption is violated, the relaxation will be slower than expected from the tube theory.

The primitive path was defined as the center line of the confining tube(thick solid line in Fig.1.6). In order to quantify this idea, we need to make some assumptions about the single chain which is surrounded by other chains. Displacement of the monomers in the direction of perpendicular to the primitive path is confined by the surrounding chains to an average distance a , which is called the **tube diameter**. Tube theory assumes that in equilibrium the primitive path is a random walk of step length a , which has the same end-to-end vector as the original chain. This leads to the following relationship:

$$Nb^2 = Za^2. \quad (1.51)$$

where Z is the number of the entanglement segments. If we define the number of monomers in an entanglement strand as $N_e = N/Z$, the following relation can be obtained from Eq.(1.51):

$$N_e = \frac{a^2}{b^2}. \quad (1.52)$$

1.8.1 Primitive chain

If we are interested in large scale dynamics of the polymer chains, the small scale fluctuation can be disregarded. We only need to use the motion of the primitive path to describe the dynamics of the original chain. The term “primitive chain” is used to represent the dynamic properties of the primitive path. The contour length s , which is measured from one chain end, is used to represent a point on the primitive chain and called the primitive chain segment s . $\mathbf{R}(s, t)$ is its position at time t , the vector

$$\mathbf{u}(s, t) = \frac{\partial}{\partial s} \mathbf{R}(s, t) \quad (1.53)$$

is the unit vector tangent to the primitive chain. In the original pure reptation model, the dynamics of the primitive chain has the following assumptions and predictions:

- The primitive chain has constant contour length L .
- The primitive chain can only move along the contour length with a certain diffusion constant D_c .
- The correlation of $\mathbf{u}(s, t)$ and $\mathbf{u}(s', t)$ decreases quickly with increasing $|s - s'|$.

Based on the third feature, the primitive chain becomes Gaussian on a large length scale. The parameter D_c is assumed to be equal to the diffusion coefficient of the Rouse model

$$D_c = \frac{k_B T}{N \xi}. \quad (1.54)$$

And since the mean square distance between the two points on the Gaussian chain is proportional to the contour length between these two points, we can have

$$\langle (\mathbf{R}(s, t) - \mathbf{R}(s', t))^2 \rangle = a |s - s'| \quad \text{for } |s - s'| \gg a. \quad (1.55)$$

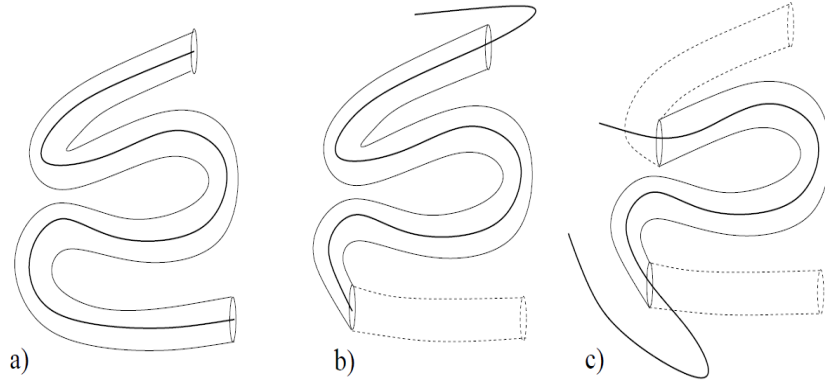


FIGURE 1.7: The relaxation of the primitive chain.

1.8.2 Reptation

Now we can study the dynamics of the primitive chain. In the beginning, the original primitive chain is trapped in a tube like region (Fig. 1.7(a)). After the primitive chain moves along the contour length back and forward, which is called reptation, one end of the chain escapes from the original tube and can adopt any directions, the other end of the tube disappears as it is evacuated (dashed line in Fig. 1.7(b)). As the chain moves back and forward on both directions, the tube is destroyed from both ends (Fig. 1.7(c)). The time correlation function of the end-to-end vector $\mathbf{R}_e(t) = \mathbf{R}(L, t) - \mathbf{R}(0, t)$ is given by

$$\langle \mathbf{R}_e(t) \cdot \mathbf{R}_e(0) \rangle = Nb^2 \sum_{p=\text{odd}} \frac{8}{p^2 \pi^2} \exp\left(-\frac{p^2 t}{\tau_d}\right) \quad (1.56)$$

The time τ_d is known as the reptation time and is related to the molecular parameters by

$$\tau_d = \frac{\xi N^3 b^4}{\pi^2 k_B T a^2} = 3Z\tau_R. \quad (1.57)$$

From Eq.(1.56), we can see that the time correlation function of the end-to-end vector is dominated by the first term with $p = 1$.

We can introduce a mathematical equation for reptation dynamics:

$$\mathbf{R}(s, t + \Delta t) = \mathbf{R}(s + \Delta s(t), t) \quad (1.58)$$

where $\Delta s(t)$ is the distance that the primitive chain moves in a time interval Δt and it is a Gaussian random variable with

$$\langle \Delta s(t) \rangle = 0 \quad (1.59)$$

$$\langle \Delta s(t)^2 \rangle = 2D_c \Delta t \quad (1.60)$$

But if $s + \Delta s(t)$ is not between 0 and L , $\mathbf{R}(s, t + \Delta t)$ should be on a new tube segment.

Now we can calculate the mean-square displacement $\langle (\mathbf{R}(s, t) - \mathbf{R}(s, 0))^2 \rangle$ of the primitive chain segment s . The function $\varphi(s, s', t)$ is defined as following:

$$\varphi(s, s'; t) = \langle (\mathbf{R}(s, t) - \mathbf{R}(s', 0))^2 \rangle \quad (1.61)$$

The time evolution equation of $\varphi(s, s'; t)$ is

$$\begin{aligned} \varphi(s, s'; t + \Delta t) &= \langle (\mathbf{R}(s, t + \Delta t) - \mathbf{R}(s', 0))^2 \rangle \\ &= \langle (\mathbf{R}(s + \Delta s(t), t) - \mathbf{R}(s', 0))^2 \rangle \end{aligned} \quad (1.62)$$

$$= \langle \varphi(s + \Delta s(t), s'; t) \rangle \quad (1.63)$$

$$= \left\langle \left(1 + \Delta s \frac{\partial}{\partial s} + \frac{\Delta s^2}{2} \frac{\partial^2}{\partial s^2} \right) \varphi(s, s'; t) \right\rangle \quad (1.64)$$

$$= \left(1 + \langle \Delta s \rangle \frac{\partial}{\partial s} + \frac{\langle \Delta s^2 \rangle}{2} \frac{\partial^2}{\partial s^2} \right) \varphi(s, s'; t) \quad (1.65)$$

And then we can get the equation

$$\frac{\partial}{\partial t} \varphi(s, s'; t) = D_c \frac{\partial^2}{\partial s^2} \varphi(s, s'; t) \quad (1.66)$$

The initial condition is

$$\varphi(s, s'; t)|_{t=0} = |s - s'|a. \quad (1.67)$$

The boundary conditions are

$$\left. \frac{\partial \varphi(s, s'; t)}{\partial s} \right|_{s=0} = -a, \quad \left. \frac{\partial \varphi(s, s'; t)}{\partial s} \right|_{s=L} = a. \quad (1.68)$$

From the calculation of Doi *et al.*[1], the solution of Eq.(1.66) is

$$\varphi(s, s'; t) = |s - s'|a + \frac{2aD_c t}{L} + \sum_{p=1}^{\infty} \frac{4La}{p^2 \pi^2} \cos\left(\frac{p\pi s}{L}\right) \cos\left(\frac{p\pi s'}{L}\right) (1 - \exp(-tp^2/\tau_d)) \quad (1.69)$$

For $t \ll \tau_d$, $\varphi(s, s, t)$ is dominated by the terms with large p .

$$\varphi(s, s, t) \approx 2a\sqrt{D_c t/\pi} \quad (1.70)$$

For $t > \tau_d$, $\varphi(s, s, t)$ is dominated by the terms with $p = 1$.

$$\varphi(s, s, t) \approx 2D_c t/Z \quad (1.71)$$

1.8.3 Contour length fluctuation(CLF)

In previous sections, the primitive chain was regarded as an inextensible string of contour length L . In reality, the contour length of the primitive path ought to be continually fluctuating around its equilibrium length under the influence of thermal fluctuations, and fluctuations sometimes play an important role in various dynamical properties. Since the primitive chain represents a set of conformations of the Rouse chain, the probability of a certain conformation of the primitive chain is proportional to the number of the conformation of the Rouse chain which can be represented by that primitive chain. If we set the polymer as a random walk confined in a tube, the entropy of the primitive chain was calculated as following[1]:

$$S(L) = S_0 - k_B \left(\frac{3L^2}{2Nb^2} + \alpha_0 \frac{Nb^2}{a^2} \right) \quad (1.72)$$

where S_0 is the entropy of the primitive chain in free space, a is the diameter of the tube and α_0 is a numerical factor. At the first sight, the entropy increases with decreasing the contour length L , but in a melt the equilibrium length does not shrink to zero. The dynamics of the contour length of the primitive chain are described by the Langevin equation for the Rouse model. The only difference

between the primitive chain and a free Rouse chain is that the equilibrium average of the contour length is $\frac{\alpha_1 N b^2}{3a}$, where α_1 is a numerical factor, while the end-to-end vector is zero in Rouse dynamics. This can be achieved by adding a tensile force applied to the chain ends[10].

These fluctuations of the chain ends will accelerate the rate at which the tube segments are visited by these ends. The longest characteristic time of the contour length fluctuation is τ_R , the Rouse relaxation time. The effect of the contour length fluctuation can be neglected in the limit $Z \rightarrow +\infty$ but not for the usual values of $Z \approx 1, \dots, 100$, where Z is the number of the tube segments.

1.8.4 Constraint release(CR)

So far it has been assumed that the tube is fixed in the material and its conformational change happens only at the ends. But the conformational change can also happen in the middle of the tube. The topological constraints for a polymer chain can be released or created by the movement of the surrounding chains. The number of constraints fluctuates in time keeping the time-average total number of constraints on a given chain constant. The exchange of topological constraints on a probe chain leads to a modification of the tube that the probe chain was confined in. This process can be modelled by a local jump of the tube, which will lead to Rouse dynamics of the tube. This mechanism is especially important in binary blends.

1.9 Microscopic molecular dynamics simulation

The molecular dynamics simulations are normally used as an experimental tool to investigate dynamic properties of the polymer, which are based on numerical integration of Newton's equations of motion for a system of particles. Each particle has a well-defined set of interaction potentials with its surrounding particles. In

simulations of polymer melts, one has to minimize the finite size effects by using periodic boundary condition.

1.9.1 Periodic boundary condition

Todd and Daivis[11] indicated the effects of periodic boundary condition on the calculation of the stress tensor of the system. If the number of the particles in the system and the volume are finite, the stress tensor can be calculated as following:

$$\sigma^{\alpha\beta}(t) = -\frac{1}{V} \sum_{i=1}^N \mathbf{R}_i^\alpha(t) f_i^\beta(t) \quad (1.73)$$

or

$$\sigma^{\alpha\beta}(t) = -\frac{1}{2V} \sum_{i=1}^N \sum_{j \neq i}^N r_{ij}^\alpha f_{ij}^\beta \quad (1.74)$$

where α, β are Cartesian coordinates, V is the volume of the system, N is the number of particles in the system, \mathbf{R}_i is the position vector of particle i , \mathbf{f}_i is the force on particle i , \mathbf{r}_{ij} and \mathbf{f}_{ij} are the distance vector and force from particle j to i respectively. However the volume of the system is infinite under periodic boundary condition. If we map all the particles into a periodic box, the volume is finite. But Eq.(1.73) does not work anymore, and Eq.(1.74) only works if we give a special definition of \mathbf{r}_{ij} which is the minimum image distance between particle i and j . Suppose we set the center of the initial box as origin and 6 surfaces are on the planes $x = -L/2$, $x = L/2$, $y = -L/2$, $y = L/2$, $z = -L/2$, $z = L/2$, the minimum image distance between particle i and j is

$$\mathbf{r}_{ij}^{min} = (\mathbf{R}_i - \mathbf{R}_j) - L \left[\frac{\mathbf{R}_i - \mathbf{R}_j}{L} \right] \quad (1.75)$$

where $[\]$ is round up operator. Once the initial positions and momenta have been allocated, each particle that is not in the original box can be treated as a copy of a particle in the original box. The periodic boundary conditions of 2D is shown in Fig.1.8. The solid circle is the real position of the particle and the open ones of

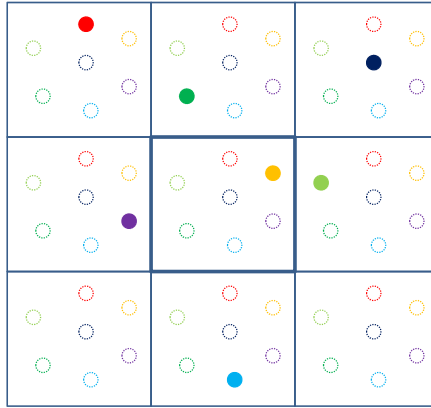


FIGURE 1.8: Periodic boundary condition.

the same colour are the copies of these particles in each image of the simulation box.

1.9.2 Pair interactions

In this thesis the polymer chains are represented by the bead-spring chain model introduced by Kremer and Grest[12][13] in their simulations of monodisperse linear polymer melts. In this model, all monomers interact via a truncated-shifted Lennard-Jones(LJ) potential

$$U_{LJ}(r) = \begin{cases} 4\varepsilon \left[\left(\frac{\sigma}{r}\right)^{12} - \left(\frac{\sigma}{r}\right)^6 + \frac{1}{4} \right]; & r < r_c \\ 0; & r \geq r_c \end{cases} \quad (1.76)$$

where σ is the length unit, r is the distance between the centers of two monomers, and the cut-off radius r_c is taken to be $2^{1/6}\sigma$, yielding purely repulsive interactions between the monomers. The LJ parameter ε is the basic energy unit in which all other energies and temperature are expressed. The monomers of the same chain are connected to their sequential neighbours by the finite extensible nonlinear elastic(FENE) potential

$$U_{FENE}(r) = -\frac{1}{2}kR_{max}^2 \ln\left(1 - \frac{r^2}{R_{max}^2}\right), \quad (1.77)$$

where the spring constant $k = 30\varepsilon/\sigma^2$ and the maximum bond length $R_{max} = 1.5\sigma$, at which the elastic energy of the bond becomes infinite. The combination of U_{LJ} and U_{FENE} leads to an average bond length $\langle l^2 \rangle^{1/2} \approx 0.97\sigma$. In addition, a harmonic bending potential is used to introduce some stiffness into the polymer chain.

$$U_{bend} = \frac{k_b}{2} \sum_{i=1}^{N-1} (\mathbf{R}_{i+1} - 2\mathbf{R}_i + \mathbf{R}_{i-1})^2 \quad (1.78)$$

where \mathbf{R}_i is the position vector of i th monomer in the chain. In this way the forces are pairwise and the bending force on the monomer i is

$$\mathbf{f}_{bend}^i = 4k_b(\mathbf{R}_{i+1} + \mathbf{R}_{i-1} - 2\mathbf{R}_i) - k_b(\mathbf{R}_{i+2} + \mathbf{R}_{i-2} - 2\mathbf{R}_i)$$

Thus, our bending potential corresponds to an attractive harmonic spring $4k_b$ between the neighbouring monomers and a repulsive harmonic spring k_b between monomers with chemical distance 2.

1.9.3 Equations of motion

The velocity Verlet algorithm is used to integrate the equations of motion of the monomers. The system is coupled to a Langevin thermostat by the standard equation,

$$m\ddot{\mathbf{r}}_i = -\nabla_i U(\{\mathbf{r}_i\}) - \xi\dot{\mathbf{r}}_i + \mathbf{f}_i, \quad (1.79)$$

where m is the monomers mass and ξ is the friction coefficient set to be $0.5(mk_B T)^{1/2}/\sigma$.

The stochastic force \mathbf{f}_i is given by a δ -correlated Gaussian noise source. The friction constant ξ and Langevin noise term \mathbf{f}_i are introduced to control the temperature and to stabilize the system. They are related by the fluctuation-dissipation theorem as $\langle \mathbf{f}_i(t) \cdot \mathbf{f}_i(t') \rangle = 6k_B T \xi \delta(t - t')$.

1.9.4 Other parameters

The simulations are performed with periodic boundary conditions applied in all three dimensions of the cubic simulation box. The time step $\Delta t = 0.012\tau$ is used in all simulation runs, where $\tau = (m\sigma^2/k_B T)^{1/2}$ is the LJ time unit. The usual simulations of melts are carried out at a temperature $T = \varepsilon/k_B$ and monomer number density $\rho = 0.85\sigma^{-3}$.

1.10 Motivation

The rheology of linear monodisperse polymers in equilibrium is the fundamental problem which has received the most attention in the field. Several theories[14][1] were proposed to describe the dynamic properties of the melts. Then several additional dynamic mechanisms such as CLF[10][15] and CR[16] were introduced to the original theory, which brought the theories in better agreement with experiments. In recent years, the most complete model was formulated[17] and accurate analytical and numerical solutions of the model became available. However, polymers in real world are never perfectly monodisperse. The interplay between different components affects the dynamics of the sample dramatically. These effects stimulate the scientists to further investigate polydisperse melts, and the binary blend is the simplest case. In Chapter 2 we will concentrate on dynamical properties of unentangled and entangled binary blends, and propose some universal properties which allow us to bridge between monodisperse and bidisperse melts.

Although the linear rheology of linear and some branched polymers can be described by the tube theory, there is still no successful model to describe the non-linear rheology due to the lack of an equation of motion for the tube. Recently an alternative model[18] was developed, which consists of a well defined single chain equation of motion. This model is supposed to allow us to investigate the properties of polymers in flow. However, several parameters corresponding to the flow need to be chosen carefully, i.e. the number of entanglements and the methods

of their creation and destruction. Microscopic molecular dynamics simulations are a feasible way to derive these parameters. The shear simulation is also an intermediate step between the experiments and the simple models. We will discuss the non-equilibrium study in Chapter 3, developing basic methods to produce non-linear rheology data from MD simulations.

As discussed before the molecular dynamics simulations are used as an experimental tool to understand the behaviour of polymer melts. Due to the limit of computer power and the large number of particles, we can not simulate a real sample at the molecular level. This encourages us to use different models at different scaling levels, which is also called coarse-grained simulations. The advantage of this method is that if we are only interested in the macroscopic properties of the polymer, the same result can be derived by using corresponding coarse-grained simulations correctly with less variables of the system and shorter simulation times. In chapter 4, we aim to derive coarse-grained variables from microscopic simulations in a systematic way and reproduce some quantities in microscopic simulations by using these variables.

Chapter 2

Orientational relaxation and coupling in equilibrium polymer melts

2.1 Overview

Slow relaxation in polymer melts has attracted constant attention of theoreticians for the last 40 years, perhaps partly because it is still lacking a general framework description. Indeed, melts of short chains are called unentangled and described by the Rouse theory[4]. Relaxation in melts of longer chains is believed to be dominated by entanglements, and is consequently described by the tube theory[14][1], which is a mean field description of an entangled system. Based on the tube theory, the terminal relaxation time τ_d and the zero shear viscosity η_0 are proportional to the cube of the molecular weight M_w in monodisperse melts. Although experimental data show a slightly larger exponent around 3.4, the tube theory has been regarded as a theoretical triumph. Many modifications like contour length fluctuation(CLF)[10][15] and constraint release(CR)[16] have been introduced to bring the original theory into better agreement with experiments. The effect of CLF can be neglected for $Z \gg 1$, where Z is the number of

the entanglement segments. Likhtman and McLeish[17] improved the treatment of contour length fluctuations using a combined theoretical and stochastic simulation approach which allows them to obtain an expression for the single chain relaxation function $\mu(t)$ without any adjustable parameters and approximations. They then used the scheme proposed by Rubinstein and Colby[16], which provides an algorithm for calculating the full relaxation function $G(t)$ from the single chain relaxation $\mu(t)$, to include the constraint release mechanism. They produced excellent agreement between theory and experiment in the linear regime. All these mechanisms from monodisperse melts should be involved in the study of polydisperse melts, which would include several other mechanisms.

In order to understand the rheology of polydisperse melts, a simple case of mixtures of long and short chains should be investigated first. The concept of CR becomes very useful and important for binary blends. After the terminal relaxation time of the short component, short chains move away and release their constraint on the long probe chain. The entanglements left in the system are the ones between the long chains. Then a dilated tube constructed by other long chains can be introduced. However, the tube dilation was not found useful in entangled linear monodisperse melts although it was applied to describe the dynamics of branched polymers successfully[19][20]. Following the initial idea of Marrucci[21], Doi *et al.*[22] derived the condition under which the long component in a binary blend would reptate in a dilated tube. They concluded that the relaxation of a long chain in binary blend would not be faster than the relaxation in the pure long chain melt if the Struglinski-Graessley parameter $r_{SG} = N_l N_e^2 / N_s^3$ is smaller than one. When $r_{SG} > 1$, Doi *et al.* suggested that the long chain would reptate in the diluted tube and the terminal relaxation time of the long chain, which depends on the composition of the blend, would not depend on the short chain length. Struglinski and Graessley[23] also concluded that the terminal relaxation time of the long chain in binary blends at different compositions was almost the same as the terminal time in the pure long chain melts if $r_{SG} < 1$.

Wang's group[24][25] did experimental studies of mixtures of long and short chains which were of different chemistry. The lengths of short chains N_s were

chosen to be smaller than the entangled length N_e to avoid the complication associated with the entanglements between long and short chains. They also studied the homo-mixture of long and short chains of polybutadiene, in which the short chains were longer than the entangled length N_e [26]. In binary blends with a Struglinski-Graessley parameter smaller than one, they saw a discernable shift of the terminal relaxation time with the composition, which contradicts the previous theories of Viovy *et al.*[27] and Doi *et al.*[22].

Wang *et al.*[28] presented extensive molecular dynamics simulations of the dynamics of diluted long probe chains entangled with a matrix of short chains. The constraint release effect in the binary blends was investigated by systematically reducing the short chain length N_s from the monodisperse case of $N_s = N_l$ to slightly above one entanglement length. The diffusion of the long chains, measured by the mean square displacements of the monomers and the centers of mass of the chains, demonstrated a systematic speed-up relative to the pure reptation behavior expected for monodisperse melts of sufficiently long polymers. On the other hand, the diffusion of the matrix chains was only weakly perturbed by the diluted long probe chains.

The aim of this chapter is to investigate the stress and orientation relaxation of monodisperse and bidisperse melts in both unentangled and mildly entangled systems, and to find out how the dynamics of each component are affected by the composition of the system. In section 2.2, we will introduce the definition of stress and orientation relaxation functions and cross-correlation functions used in this thesis. In section 2.3, the stress-optical rule in MD simulations is established. In sections 2.4 and 2.5, the stress and orientational relaxation of monodisperse and bidisperse melts are investigated respectively. In section 2.6, we will propose a universal time-dependent orientational coupling parameter for both monodisperse and bidisperse melts. Using this universal coupling parameter, the total relaxation function of binary blends can be obtained from the auto-relaxation function of each component.

2.2 Definition of the orientational correlation function

Based on the fluctuation-dissipation theorem stated in section 1.6.3, we can derive the orientation relaxation function by calculating the time correlation functions. An efficient method to calculate the time correlation function on the fly was developed by Ramirez *et al.*[29].

$\chi_j(t')$ is set as the notation of orientation tensor of chain j at time t' :

$$\chi_j^{\alpha\beta}(t') = \sum_{i=1}^N u_{ji}^\alpha(t') u_{ji}^\beta(t') \quad (2.1)$$

$$u_{ji}^\alpha(t') = R_{j,i}^\alpha(t') - R_{j,i-1}^\alpha(t') \quad (2.2)$$

where α, β are Cartesian coordinates, i and N are the monomer index and the number of bonds in the chain respectively. For any time-dependent tensor $T(t')$ the correlation function of this tensor \mathcal{F} is defined as:

$$\mathcal{F}_{xy}(T, t) = \langle T_{xy}(t + t') T_{xy}(t') \rangle \quad (2.3)$$

where $\langle \rangle$ is averaging over t' and $\mathcal{F}(T, t)$ averages over all possible selection of xy axis. Then in monodisperse melts the auto-correlation function of the chain orientation $A(t)$ and the correlation function of the orientation of the whole system $S(t)$ are defined as following:

$$A(t) = \frac{1}{N_c N} \sum_{j=1}^{N_c} \mathcal{F}(\chi_j, t) \quad (2.4)$$

$$S(t) = \frac{1}{N_c N} \mathcal{F} \left(\sum_{j=1}^{N_c} \chi_j, t \right) \quad (2.5)$$

where N_c is the number of chains in the system. And the difference $C(t) = S(t) - A(t)$ is called the orientation cross-correlation function. After comparing Eq.(2.4) with Eq.(2.5), we can see that $C(t)$ is nothing but the cross-correlation function of

different chain tensors

$$C(t) = \frac{1}{N_c N} \sum_{m=1}^{N_c} \sum_{n=1; n \neq m}^{N_c} \langle \chi_m(t+t') \chi_n(t') \rangle \quad (2.6)$$

Similar notations are defined in bidisperse melts:

$$A_s(t) = \frac{1}{N_{c1} N_1} \sum_{j=1}^{N_{c1}} \mathcal{F}(\chi_j, t) \quad (2.7)$$

$$A_l(t) = \frac{1}{N_{c2} N_2} \sum_{j=N_{c1}+1}^{N_{c1}+N_{c2}} \mathcal{F}(\chi_j, t) \quad (2.8)$$

$$S_s(t) = \frac{1}{N_{c1} N_1} \mathcal{F} \left(\sum_{j=1}^{N_{c1}} \chi_j, t \right) \quad (2.9)$$

$$S_l(t) = \frac{1}{N_{c2} N_2} \mathcal{F} \left(\sum_{j=N_{c1}+1}^{N_{c1}+N_{c2}} \chi_j, t \right) \quad (2.10)$$

$$S_{tot}(t) = \frac{1}{N_{c1} N_1 + N_{c2} N_2} \mathcal{F} \left(\sum_{j=1}^{N_c} \chi_j, t \right) \quad (2.11)$$

where s, l indicate the short and long component of the binary blend. N_{c1}, N_{c2} are the number of the chains of short and long components. N_1, N_2 are the number of bonds in short and long chains. The cross-correlation functions in the binary blend are defined as following:

$$C_{ss}(t) = \frac{S_s(t) - A_s(t)}{\varphi_s} \quad (2.12)$$

$$C_{ll}(t) = \frac{S_l(t) - A_l(t)}{\varphi_l} \quad (2.13)$$

$$C_{sl}(t) = \frac{S_{tot}(t) - \varphi_s S_s(t) - \varphi_l S_l(t)}{2\varphi_s \varphi_l} \quad (2.14)$$

where $C_{ss}(t)$ is the cross-correlation function of one short chain and all other surrounding short chains (similar for $C_{ll}(t), C_{sl}(t)$), $\varphi_s = \frac{N_1 N_{c1}}{N_1 N_{c1} + N_2 N_{c2}}$ and $\varphi_l = \frac{N_2 N_{c2}}{N_1 N_{c1} + N_2 N_{c2}}$ are the bonds fractions of short and long components. As we can see the orientation is calculated by summing over all the bond vectors.

From Eqs. (2.12), (2.13) and (2.14), the total orientation relaxation function can be described by the sum of the self- and cross-correlation orientation relaxation

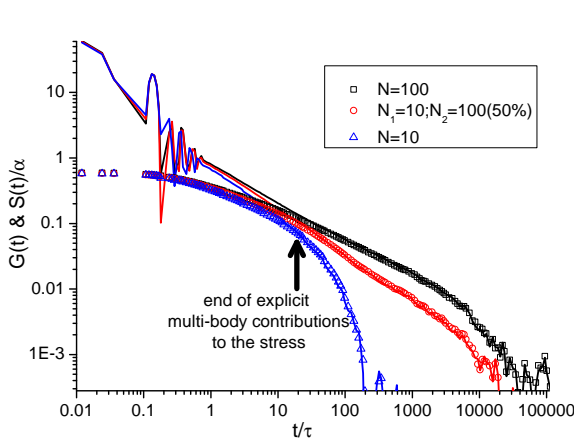


FIGURE 2.1: Stress (lines) and orientation (open symbols) relaxation functions in monodisperse melts and their binary blends. The reason of the oscillations of stress relaxation at short times is bond length relaxation.

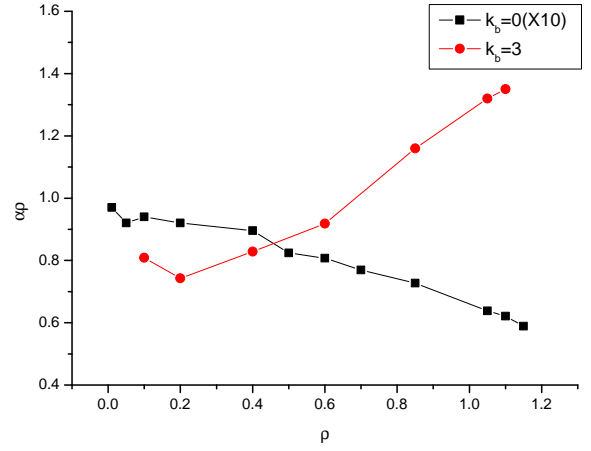


FIGURE 2.2: Stress-optical coefficient α times density ρ as a function of density in flexible(square) and semi-flexible(circle) systems. The results from flexible system are shifted upward by 10 to compare with counterpart of semi-flexible system.

functions of each component:

$$S_{tot}(t) = \varphi_s A_s(t) + \varphi_l A_l(t) + \varphi_s^2 C_{ss}(t) + \varphi_l^2 C_{ll}(t) + 2\varphi_s \varphi_l C_{sl}(t) \quad (2.15)$$

2.3 Stress optical law

Before doing the orientation analysis, let us check if the stress optical law works in our equilibrium simulations. The stress optical law states that the orientation relaxation function should be proportional to the stress relaxation function:

$$G(t) = \frac{V}{k_B T} \mathcal{F}(\sigma, t) \quad (2.16)$$

$$G(t) = \frac{1}{\alpha} S(t) \quad (2.17)$$

where $G(t)$ is the usual stress relaxation function, σ is the stress tensor and α is the stress-optical coefficient. More details of stress relaxation function of monodisperse melts were described by Likhtman *et al.*[30]. Fig.2.1 shows stress relaxation

functions of two monodisperse melts and of their 50% blend, together with orientation relaxation, multiplied by $1/\alpha$. We found that $\alpha=0.0885$ and 1.28 for flexible and semi-flexible Kremer-Grest model at monomer density $\rho=0.85\sigma^{-3}$ respectively. Three important observations are due: (i) indeed the two relaxation functions become proportional to each other after about 30 Lennard-Jones time units, and remain proportional to each other with accuracy better than 1%; (ii) The stress-optical coefficient does not depend on chain lengths and (iii) it remains the same for binary blends, in accordance with experiment. In Fig.2.2 we plot the stress-optical coefficient times density as a function of density in both flexible and semi-flexible systems. The curve from flexible system is shifted upward by a factor of 10 to compare with the ones from semi-flexible system. We can see that the results behave differently in two systems. Thus, studying orientation coupling should provide useful information for the stress relaxation and rheology.

2.4 Monodisperse melts

2.4.1 Monomer mean-square displacement

A quantity traditionally measured in molecular dynamics is the monomer mean-square displacement $g_1(t)$. Doi and Edwards[1] anticipated that this curve should show four different power laws on different regimes. However, we find it very difficult to see clear power-laws in our simulations. We calculate the mean-square displacement of monomers in the chain ends and middle and average the results over groups of five monomers along the chain. We divide the averaged results by the Rouse power-law, $t^{1/2}$, and then present the results in Fig.2.3 and Fig.2.4 for monodisperse flexible and semi-flexible chains respectively.

We find that the pictures are very rich and full of features. First of all, at short times as chain ends have more mobility than the middle section, the mean-square displacement of chain ends is higher than the one of middle monomers. The figures first show a positive slope around 0.5 which indicates that the monomers follow

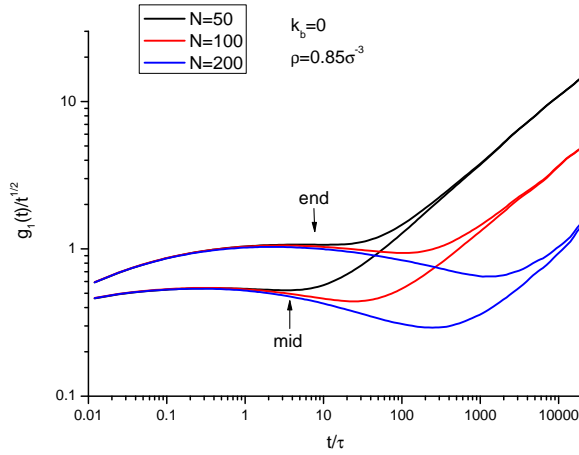


FIGURE 2.3: Mean-square displacement of chain ends and middle for flexible chains.

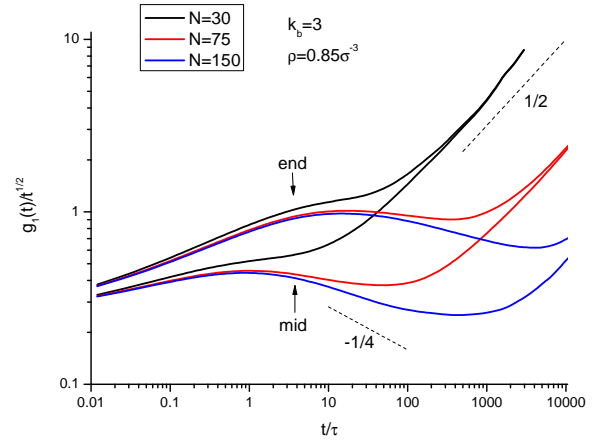
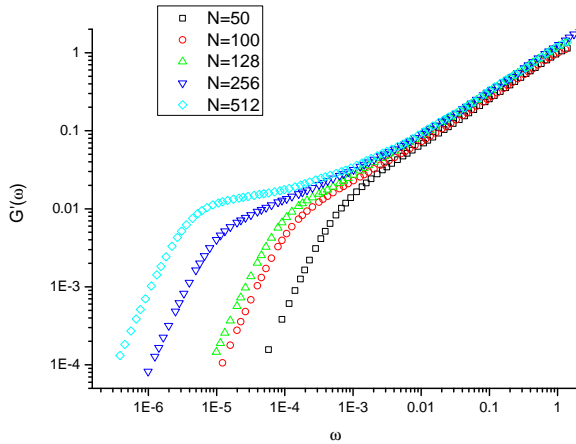
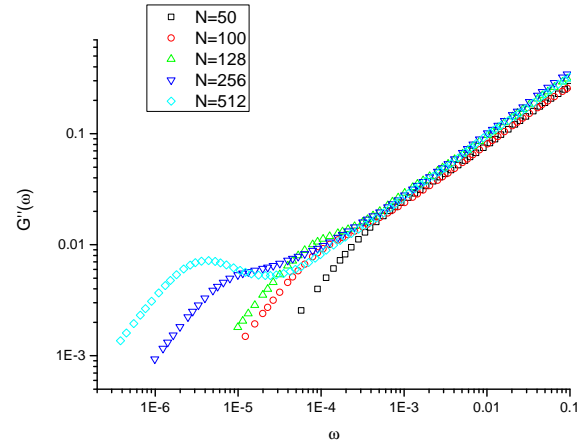
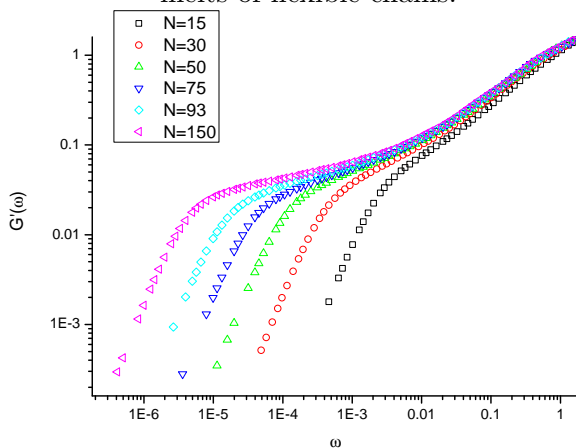
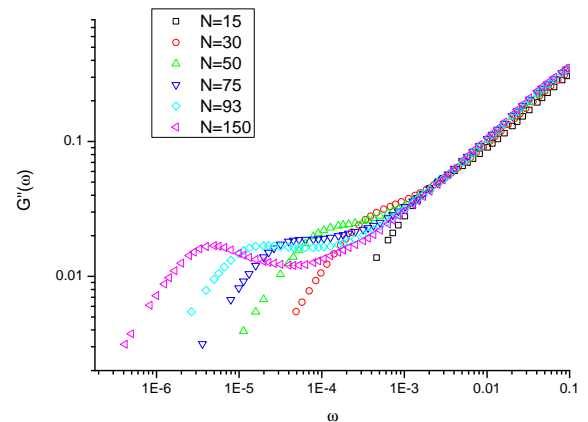


FIGURE 2.4: Mean-square displacement of chain ends and middle for semi-flexible chains.

the random walk in the space and do not feel the connectivity at these short times. Then the plateaus come out for both middle and end monomers which indicates that the chains are in Rouse regime. After comparing the maximum for middle and end monomers, we can see that the mean-square displacement of chain ends is exactly twice of counterpart of middle section, which can be explained by that the chain ends only feel the connectivity from one side comparing to from both sides for middle monomers. Now the curves of entangled systems deviate from the ones of unentangled systems. A negative slope around $-1/4$ comes out in entangled systems which indicates that the chain is trapped in a constraint tube and reptation and CLF are the only mechanisms in this regime. After the time when chains are totally relaxed, two curves of middle and ends monomers join each other and have a positive slope around 0.5 which can be interpreted as the escape time from the tube.

2.4.2 Storage and loss moduli

We first present the storage and loss moduli in flexible and semi-flexible monodisperse melts with different chain lengths in Fig.2.5-2.8. The terminal time and zero-shear viscosity of different chain lengths and stiffnesses are listed in Table.2.1. The entanglement lengths N_e of flexible and semi-flexible chains are around 50 and 15 respectively[30]. From Fig.2.5 and Fig.2.7, $G'(\omega)$ starts to show a plateau with


 FIGURE 2.5: G' of monodisperse melts of flexible chains.

 FIGURE 2.6: G'' of monodisperse melts of flexible chains.

 FIGURE 2.7: G' of monodisperse melts of semi-flexible chains.

 FIGURE 2.8: G'' of monodisperse melts of semi-flexible chains.

increasing chain length. After comparing these two figures, $G'(\omega)$ behaves similar if two chains with different stiffnesses have the same number of entanglements. i.e. flexible chain with $N=256$ and semi-flexible chain with $N=75$ both have around 5 entanglements. However, $G''(\omega)$ have different features with different stiffness even if both chains have same number of entanglements. The modulus G_c at the crossing point is defined as

$$G_c = G'(\omega_c) = G''(\omega_c) \approx G''_{max}.$$

In the semi-flexible systems, the amplitude of G''_{max} is almost the same for different chain lengths which is not true in flexible systems.

2.4.3 Orientational relaxation

In order to investigate relaxation coupling between different chains, the total and self orientational relaxation functions of monodisperse melts are measured in flexible and semi-flexible systems. The lines and open symbols in Fig.2.9 and Fig.2.10 are the total relaxation functions $S(t)$ and the self relaxation functions $A(t)$ respectively. We use several Maxwell modes to fit the self relaxation functions $A(t)$

$$A(t) = \sum_i G_i \exp(-t/\tau_i) \quad (2.18)$$

where G_i and τ_i are the plateau modulus and relaxation time of mode i . The terminal relaxation time τ_d is the largest τ_i among all the modes. We can see that the terminal time τ_d becomes larger with increasing chain length (Table.2.1). The ratio of τ_d and the square of molecular weight are shown in Fig.2.11. As the molecular weight of one entanglement strand N_e in flexible and semi-flexible systems are 50 and 15 respectively, we can see that the data for flexible chains in Fig.2.11 remains constant when $N < 100$ which obey the Rouse theory ($\tau_d \sim N^2$) and then a slope of 1 comes out when $N = 256$. The semi-flexible data points presented well entangled systems which obey the reptation theory ($\tau_d \sim N^3$). However, it seems that the last points in both systems did not follow the reptation theory. We suppose the reason is that the simulation time is not long enough to obtain accurate data for such long chains.

Flexible ($k_b = 0$)					Semi-flexible ($k_b = 3$)				
N	N_c	$\tau_d[\tau]$	$\eta_0[\varepsilon\tau\sigma^{-3}]$	$\tau_{run}[\tau]$	N	N_c	$\tau_d[\tau]$	$\eta_0[\varepsilon\tau\sigma^{-3}]$	$\tau_{run}[\tau]$
10	100	85	8.5	9E6	15	200	490	30	2.3E6
20	50	320	15	2.8E7	30	100	2700	120	2.3E6
50	50	1900	45	2.9E7	50	100	9100	350	2.4E7
100	50	8200	120	1.3E7	75	200	29000	880	9.6E6
128	70	10400	180	1E6	93	100	91200	2500	2.1E6
256	100	107000	950	1.6E7	150	100	270000	7600	9.1E6
512	150	264000	3600	4.3E6					

TABLE 2.1: Terminal time τ_d of different chain lengths of flexible and semi-flexible chains.

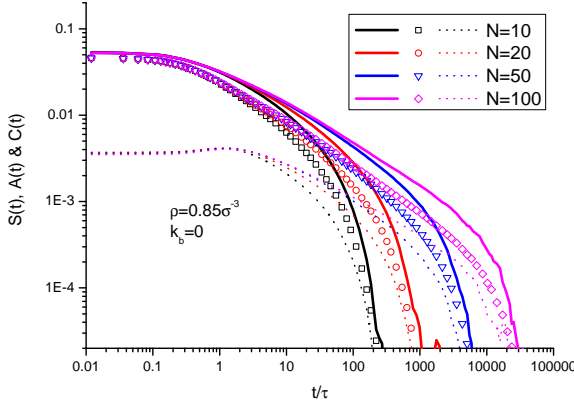


FIGURE 2.9: $S(t)$ (line), $A(t)$ (open symbol) and $C(t)$ (dashed line) of monodisperse melts of flexible chains.

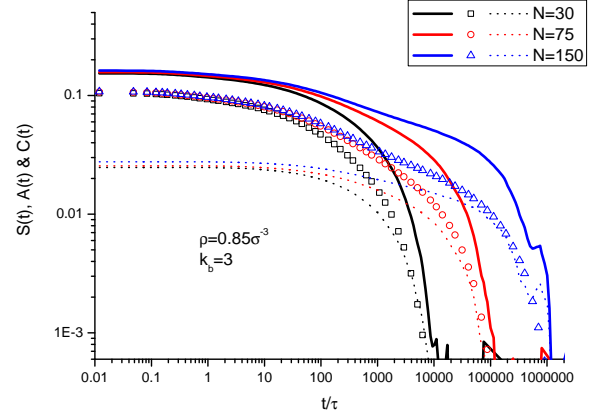


FIGURE 2.10: $S(t)$ (line), $A(t)$ (open symbol) and $C(t)$ (dashed line) of monodisperse melts of semi-flexible chains.

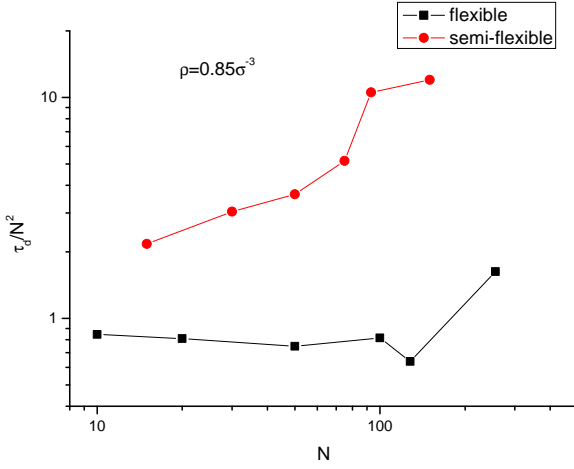


FIGURE 2.11: τ_d of flexible and semi-flexible chains as a function of chain lengths.

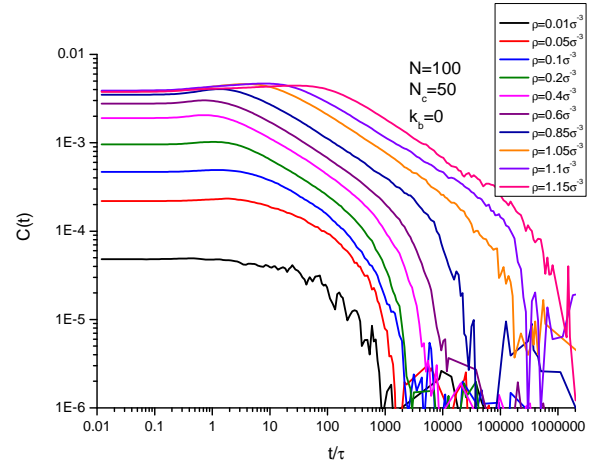


FIGURE 2.12: Cross-correlation functions of flexible chains $N=100$ at different densities.

The difference between the total and the self relaxation functions is defined as the cross-correlation function(dashed lines in Fig.2.9 and 2.10). All cross-correlations start at the same point at $t = 0$ and remain constant until $t \approx 0.5\tau$, and then increase a little (15%) before starting to relax with a slope of approximately -0.5 , similar to the self relaxations. However, there is no overshoot in the cross-correlation functions in the semi-flexible systems.

The cross-correlation functions of flexible chains at different densities are shown in Fig.2.12. The amplitude of the overshoot around $t \approx \tau$ becomes larger with increasing density. For high densities, the time of the overshoot shifts to the right. For example, this overshoot appears around $t \approx 10\tau$ in the system with

$\rho = 1.05\sigma^{-3}$. This is because the monomers are trapped in “cages” created by other surrounding monomers and spend more times in them before escape, and the bonds are affected in a similar way. Now we are going to ask what will happen if two components with different chain lengths are mixed. Ylitalo *et al.*[31] have shown that the concentration of the short component will strongly affect the relaxation of the long component. Now we would like to investigate how the composition of binary blends affect the dynamics of each component.

2.5 Bidisperse melts

2.5.1 Monomer mean-square displacement

In this section, we will investigate the mean-square displacement of monomers of each component in semi-flexible binary blends. In Fig.2.13, short and long components have chain lengths $N_1=30$, $N_2=150$ which are shown by lines and symbols respectively. Different colours indicate different composition of binary blends. Similar features are observed comparing to the mean-square displacement of monodisperse melts(Fig.2.4). The dynamics of short chains feels little effect from the composition of the blend. However, the long chains’ properties change significantly with increasing their volume fraction. Especially in the binary blend with $\varphi_l=10\%$, the mean-square displacement of the middle monomers does not show a negative slope after the terminal time of short component(square symbols in Fig.2.13). This can be explained by that the effective entanglement length N_e on long chains at this composition is ten times larger than the N_e in the monodisperse melt of long chains by double reptation theory and there is few entanglements between different long chains, which makes long chains obey Rouse dynamics.

We also investigate the mean-square displacement of long component in binary blends with the same φ_l but different short chains. We find that if the volume fraction of long component is large enough, the short component does not affect

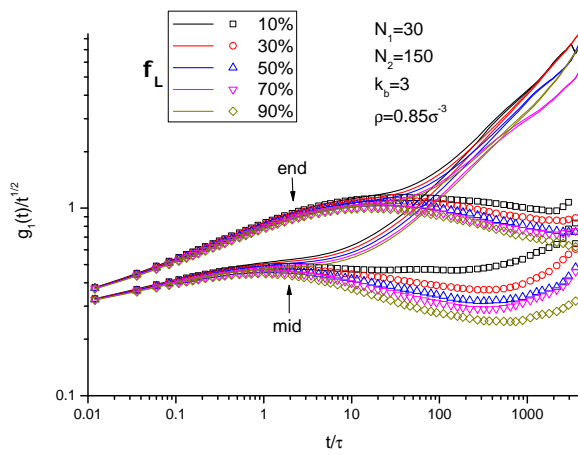


FIGURE 2.13: Mean-square displacement of short (lines) and long (symbols) components in semi-flexible binary blends of $N_1=30$, $N_2=150$.

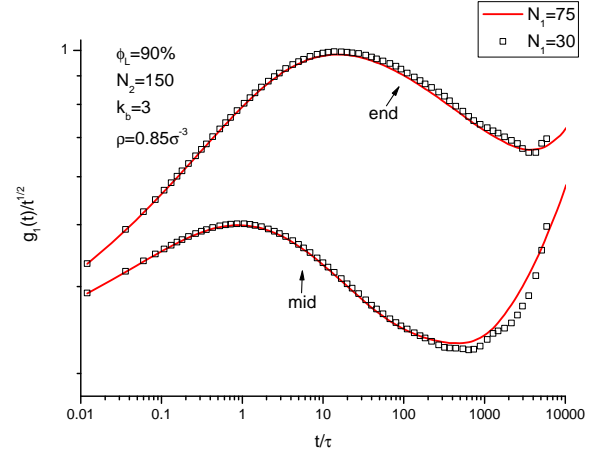


FIGURE 2.14: Mean-square displacement of long chains in semi-flexible binary blends with $N_2=150$, $\varphi_l=90\%$.

the $g_1(t)$ of long component. In Fig.2.14, the length of long component is $N_2=150$, the lengths of short component are chosen as 30 and 75. The volume fraction of long chains φ_l is set to 90%. We can see that the mean-square displacement of middle and end section of long component overlap with each other.

2.5.2 Storage and loss moduli of semi-flexible chains

In this section we will concentrate on the relaxation functions of binary blends. Because the entanglement length N_e is much larger in flexible system than in the semi-flexible system, the chain length would be much longer in flexible system if the same number of entanglements is required. So we will only investigate the semi-flexible binary blends in this section. $N_1=3, 15, 30, 75$ and $N_2=150$ are chosen for the short and long components respectively.

First the binary blend of $N_1=30$, $N_2=150$ will be investigated, whose components have big difference of terminal relaxation time. G' and G'' of the binary blends with different compositions are shown in Fig.2.15 and Fig.2.16 together with monodisperse melts of each component. In Fig.2.15, G' has two clear relaxation steps in the blends with $\varphi_l=10\%$, 30%. G'' in Fig.2.16 shows more interesting

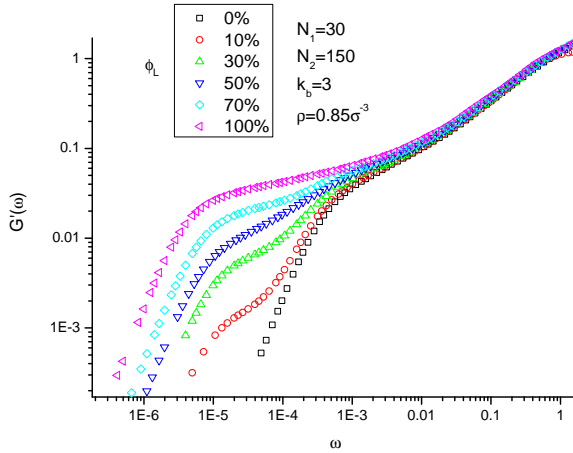


FIGURE 2.15: G' of binary blends of semi-flexible chains with $N_1 = 30$, $N_2=150$.

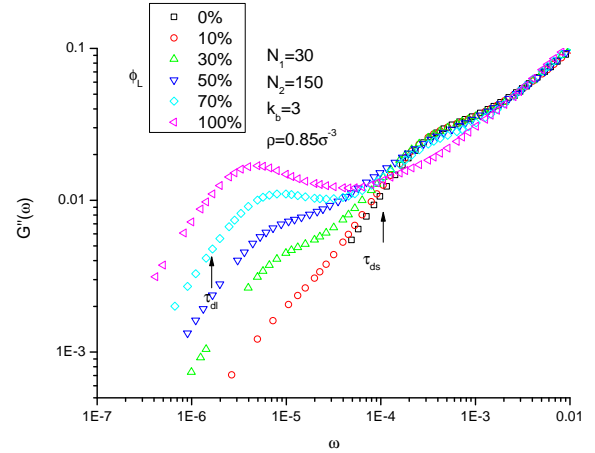


FIGURE 2.16: G'' of binary blends of semi-flexible chains with $N_1 = 30$, $N_2 = 150$ where τ_{ds} and τ_{dl} are terminal time of short and long components respectively.

features. If we decrease the volume fraction of the long chains, the stress relaxation around short chain's terminal relaxation time is dominated by the relaxation of short chains and the segments between two entanglements on the long chains, and the long chains are trapped in dilated tubes constructed by other long chains, which can explain why G'' around $\omega=2 \times 10^{-4}$ in the systems with $\varphi_l=10\%$, 30% overlap with the one from monodisperse melt of $N=30$.

We also investigate the binary blends with $N_1 = 75$, $N_2 = 150$. G' and G'' with different compositions are shown in Fig.2.17 and Fig.2.18 together with the monodisperse melts of each component. We can only observe one relaxation step of G' even at small φ_l . The twin peak characteristics of G'' can be observed in Fig.2.18. Zero-shear viscosity is derived from the time integral of $G(t)$ and is shown in Fig.2.19. Fig.2.20 shows terminal time τ_d as functions of concentration φ_l for different short chain lengths. As the signal of stress relaxation is very noisy at longer times, we use the auto-correlation function of long component's orientation to derive the terminal time of the whole system. The aim of the theory is to describe these results. But in order to do this, we need to understand the coupling between relaxation of different components.

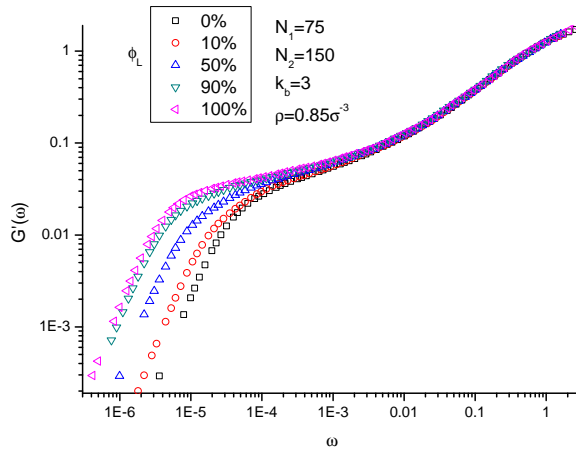


FIGURE 2.17: G' of binary blends of semi-flexible chains with $N_1 = 75, N_2=150$.

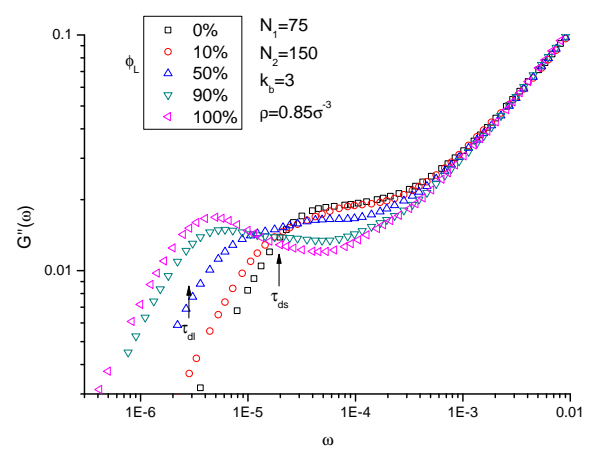


FIGURE 2.18: G'' of binary blends of semi-flexible chains with $N_1 = 75, N_2 = 150$ where τ_{ds} and τ_{dl} are terminal time of short and long components respectively.

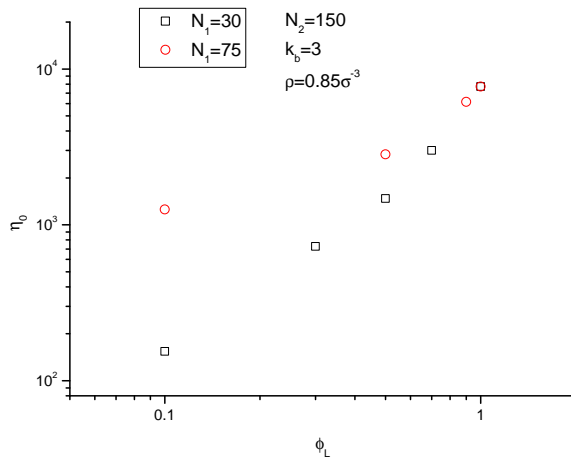


FIGURE 2.19: Viscosity η_0 as a function of concentration for different binary blends.

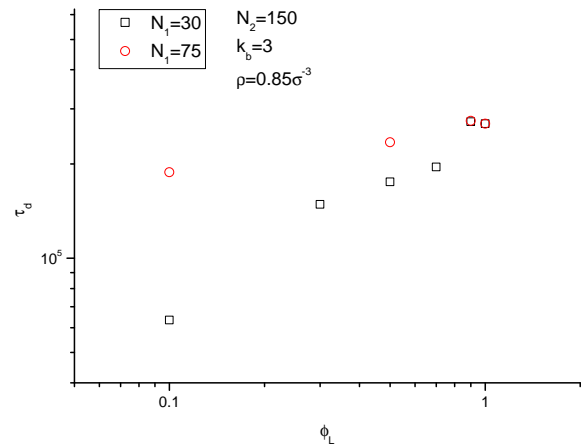


FIGURE 2.20: Terminal relaxation time τ_d as a function of concentration for different binary blends.

2.5.3 Orientational relaxation

The total orientation relaxation functions with different concentrations of the long chains are shown in Fig.2.21 and Fig.2.22 for flexible and semi-flexible chains respectively. It is clear that these figures exhibit certain general features; namely, as the concentration of the long chains increases, the total relaxation is retarded. In the flexible systems, the short chains only contain 10 monomers, which is much smaller than the entanglement length $N_e \approx 50$. So total relaxation at short times is only due to short chains relaxation but not constraint release induced by short

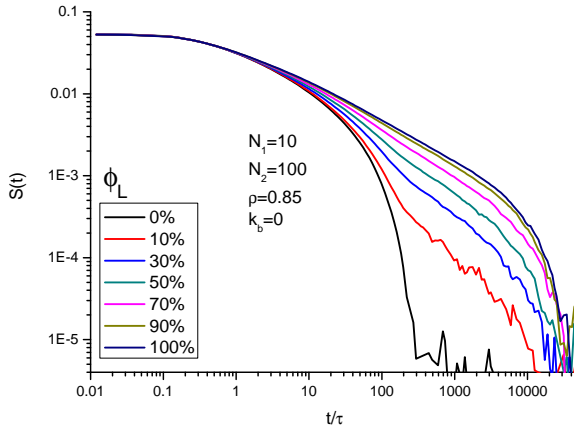


FIGURE 2.21: Total orientational relaxation function in binary blends of flexible chains for different compositions.

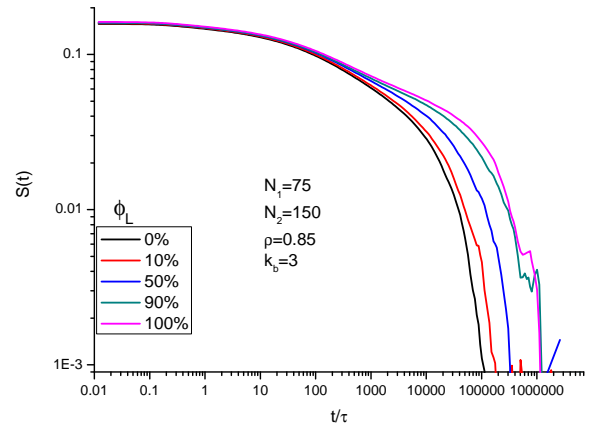


FIGURE 2.22: Total orientational relaxation function in binary blends of semi-flexible chains for different compositions.

chain. However, at longer times total relaxation is governed only by the long chains' relaxation as indicated by the shape of the relaxation functions. The terminal relaxation of the whole system is controlled by the slowest relaxing component in the blends.

Now we turn our attention to different contributions to the total relaxation function. All six terms in Eq.(2.15) of flexible and semi-flexible systems are shown in Fig.2.23 and Fig.2.24 respectively. Surprisingly, the cross-correlation function between short and long components does not relax until the relaxation time of the long chains, which indicates that the coupling is an important relaxation mechanism at all times. We can also see that $C_{ss}(t)$ is not totally relaxed after the terminal relaxation time of the short component. It is possibly a result of two short chains being coupled with long chains at the same time, which makes both short chains affected by the orientation of the long chain.

We would like to introduce a definition of the total relaxation function of each component $E(t)$ in the binary blend, which is normally measured in experiments[31]. $E_s(t)$ and $E_l(t)$ are the orientation relaxation of short and long chains after a step deformation of the whole sample. Ramirez *et al.*[32] demonstrated that in order to calculate $E(t)$ in equilibrium simulations, one has to include the cross-correlation

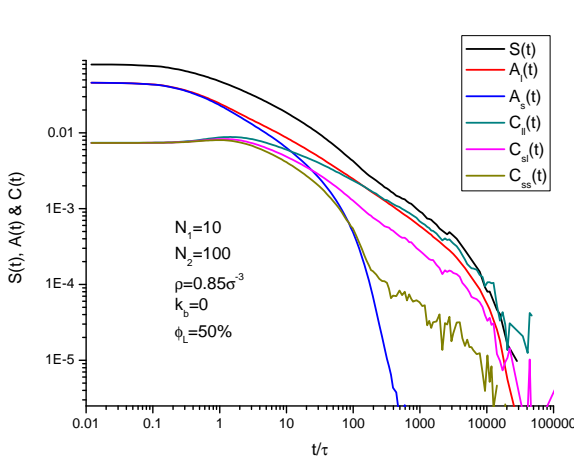


FIGURE 2.23: All components of orientation relaxation function of binary blend of flexible chains.

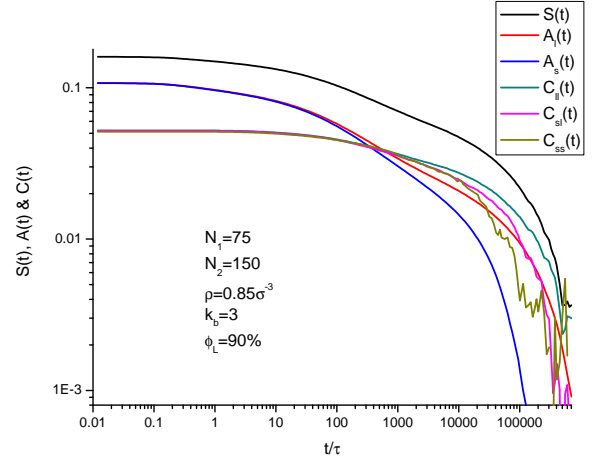
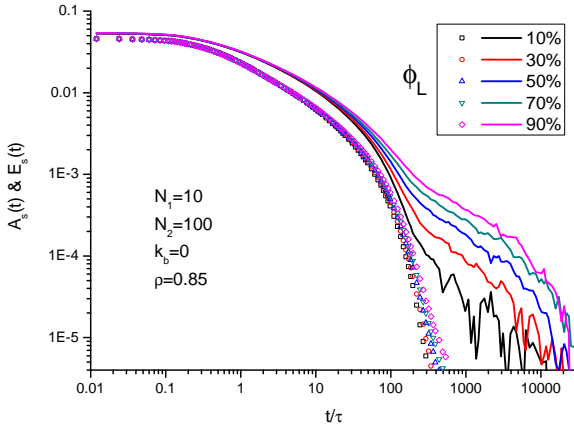
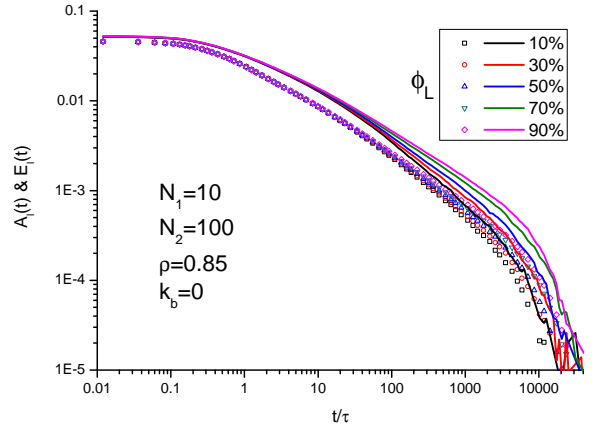


FIGURE 2.24: All components of orientation relaxation function of binary blend of semi-flexible chains.


 FIGURE 2.25: $A_s(t)$ (symbols) and $E_s(t)$ (lines) of short chains. Different colours are for different concentrations of the long chains.

 FIGURE 2.26: $A_l(t)$ (symbols) and $E_l(t)$ (lines) of long chains. Different colours are for different concentrations of the long chains.

terms:

$$E_s(t) = A_s(t) + \varphi_s C_{ss}(t) + \varphi_l C_{sl}(t) \quad (2.19)$$

$$E_l(t) = A_l(t) + \varphi_l C_{ll}(t) + \varphi_s C_{sl}(t) \quad (2.20)$$

Summing up these two equations we can see that $S_{tot}(t) = \varphi_s E_s(t) + \varphi_l E_l(t)$.

Relaxation functions of short component in flexible systems are presented in Fig.2.25 together with its auto-correlation function. In these figures, the effect of long chains in the system is surprisingly strong, producing a dramatic retardation in the short component relaxation with increasing concentration of long chains. After comparing Fig.2.21 and Fig.2.25, we can see that the terminal relaxation

time of short chains measured in $E_s(t)$ are equal to the terminal relaxation time of the whole system, which suggest that short component's orientation relaxes with the orientation of the surrounding environment.

Relaxation functions of long chain in flexible systems are presented in Fig.2.26. The long chain terminal relaxation time is reduced if short chains' concentration increases. For a given blend, the total relaxation of longer component is higher than its self relaxation. The coupling between different chains is one of the reasons. However, they have the same terminal time as the longer component relaxation determines the long-time relaxation.

Based on the Rouse theory, auto-correlation functions of the same unentangled component in different systems should not be affected by surrounded environment. However, we get a slightly different result from the simulations. In Fig.2.25, the terminal times of the auto-correlation functions of short component are different. We suppose that these differences are due to the chain ends effect. In the simulations, the chain ends are moving faster than the middle part of the chain, which means that the effective friction of all monomers will be smaller if the proportion of the chain ends in the system increases. So before comparing the self relaxation functions from different systems, we need to shift the data to avoid these chain ends effect. The expression of the shift factor is found to be

$$\lambda_{shift} = 1 + C \left(\frac{\varphi_s}{N_1} + \frac{\varphi_l}{N_2} \right) \quad (2.21)$$

where $C = 3.2$ in flexible systems and 7.53 in semi-flexible systems.

2.5.4 End-to-end vector relaxation

In this section we will investigate the end-to-end relaxation functions of each component in binary blends. The end-to-end vector relaxations of short chains in binary blends of $N_1 = 30$, $N_2 = 150$ with different compositions are shown in Fig.2.27(lines). As we discussed in previous section, the dynamics of short component is highly affected by the fraction of chain ends in the system. In order

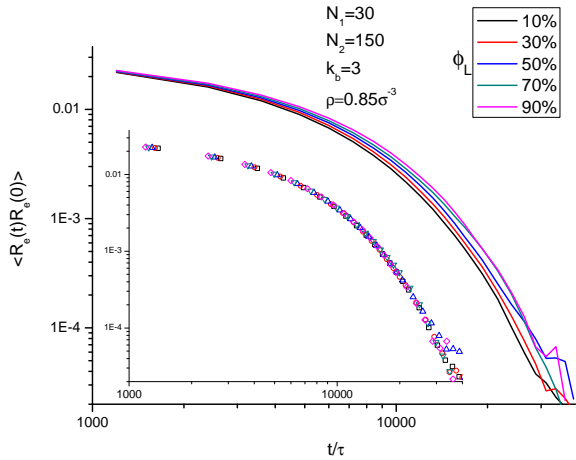


FIGURE 2.27: End-to-end vector relaxation of short component in binary blends with different conformations. After shifting the data according to Eq.(2.21), all figures collapse onto a master curve(inset).

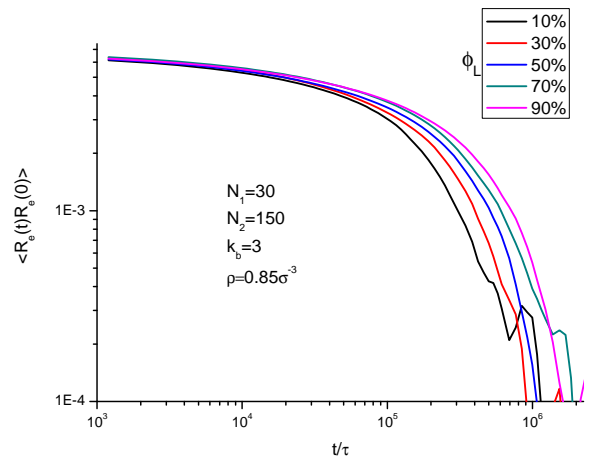


FIGURE 2.28: End-to-end vector relaxation of long component in binary blends with different conformations.

to eliminate this chain ends effect, we need to shift the data by using Eq.(2.21). The shifted results are shown in the inset of Fig.2.27. We can see that all figures collapse onto a master curve.

The end-to-end vector relaxations of long chains in binary blends with different compositions are shown in Fig.2.28. In previous section we already know that the terminal relaxation times of binary blends depend on the fraction of long chains in the system. As the statistics of long chain's orientation auto-correlation function is much better than the stress relaxation, we use the long chain's orientation auto-correlation function to obtain the terminal time of the whole system.

2.6 Orientational coupling

Both Rouse and tube theories rely on a very simple assumption, namely that all chains move independently from each other, i.e. the effect of all other chains on a probe chain can be described by random δ -correlated forces and by the static tube constraints for longer chains. The reasoning behind such an assumption is based on the Flory theorem, which states that the excluded volume interaction in polymer melts is screened. This makes the chains obey Gaussian random walk statistics

on large scales, making single chain dynamics Rouse-like at large scales. However, the fact that each individual chain obeys Rouse dynamics does not mean that the total stress relaxation is also known: this will only be true if cross-correlation between the chains are negligible, which as we showed in Figs.2.21-2.24 is clearly not the case.

The tube theory uses an assumption of chain independence twice: each chain reptates in its tube independently, and the piece of chain which escaped from the tube is assumed to adopt a random orientation independent on surrounding chains. Merrill *et al.*[9] demonstrated a long time ago that if the second assumption is violated, the relaxation will be slower than expected from the tube theory. Thus, the validity of both Rouse and tube theories clearly depends on the coupling and cross-correlations between orientation relaxation of different chains in the melt.

Various experiments suggested that there is a specific interaction in polymer melts called nematic interaction, which orient the surrounding polymer segments toward the same direction. Doi *et al.*[33][34] introduced models which account for the nematic interaction for reptation and Rouse dynamics. In monodisperse melts, they found that the stress-optical law was valid in this model, and the stress-optical coefficient became larger with increasing strength of the nematic field. The theory was also generalized for binary blends, which showed that the relaxation of the short chains were not independent of the long chains relaxation due to the nematic interaction.

Experimentally, orientation coupling was investigated by a combination of dielectric dichroism and birefringence by Ylitalo *et al.*[31], and by NMR by Graf *et al.*[35]. In the first group of experiments, one of the components in binary mixture was labeled and its orientation relaxation was measured after a step-strain experiment. The labeling was achieved by replacing a portion of hydrogens on the polymer backbone with deuterium and then performing the measurements at the infra-red wavelength of the carbon-deuterium vibrational absorption. It was shown that the short component orientation is not fully relaxed until the longest relaxation time of the long component, and that the relaxation of short component

becomes proportional to the total relaxation after the expected reptation time of the short component:

$$E_s(t)/E_s(0) = \varepsilon S_{tot}(t)/S_{tot}(0) \quad (2.22)$$

where $E_s(t)$ is short component orientation relaxation function, $S_{tot}(t)$ is the total orientation relaxation function. The coupling parameter ε defined through this relationship was found to be $\varepsilon \approx 0.45 \pm 0.05$. It was also shown that in order to describe the relaxation with the tube theory, the coupling effects must be taken into account. However, this coupling coefficient ε can only be measured after relaxation of the short component. Also, this definition is not applicable to monodisperse melts.

In ^1H Double quantum NMR experiments Graf *et al.* measured the chain dynamics of a polybutadiene melt well above the glass transition and confirmed significant residual bond orientation after elementary entanglement time τ_e . They concluded that restrictions by entanglements can not be the only source of orientation coupling. A possible reason for this strongly anisotropic orientational dynamics may be the intermolecular orientational correlations. Our molecular dynamics simulations discussed below support this conclusion.

Orientation coupling effects were also investigated in molecular dynamics simulations by Baljon *et al.*[36], whose protocol was similar to the experimental one. They simulated one very long chain ($N = 5000$) in the sea of small chains after the step deformation and looked at the order parameter $q^{\alpha\beta} = (3/2)^{1/2}(u^\alpha u^\beta - \frac{1}{3}\delta^{\alpha\beta})$ of each component and the bulk, where \mathbf{u} is the unit bond vector and $\delta^{\alpha\beta}$ is a unit tensor. Similarly to the experiment of Ylitalo *et al.*, they found that the short chains order parameter does not relax to zero after the relaxation time of short chains, but instead becomes proportional to the order parameter of the long chain, with the somewhat smaller proportionality coefficient $\varepsilon \approx 0.28$. Baljon *et al.* also attempted to calculate ε from the static properties of the melt, namely from the orientation distribution function around each bond. The long chain bonds were oriented by using an explicit nematic field instead of stretching. However, smaller

coefficient $\varepsilon \approx 0.18$ was found. They argued that the difference can be explained by positional anisotropy of chain bonds belonging to other chains. By following the same procedure, we are able to reproduce similar results. However, this coupling parameter ε is only available in binary blends which have wide separation of chain lengths. And we believe that the coupling is also very important in monodisperse melts, which means that a more universal measure of coupling is desirable.

In section 2.6.1, the coupling effect in the system of dumbbells at different densities is investigated. In section 2.6.2, the short-range coupling parameter proposed by Doi *et al.* is measured in our simulations of binary blends. From section 2.6.3 to 2.6.8, a universal time-dependent coupling parameter $\kappa(t)$ is introduced in both monodisperse and bidisperse melts. We then demonstrate that we can predict the total relaxation in binary blends by using the self relaxation of each component and this universal coupling parameter. In unentangled melts, we can predict all blend relaxation functions from the monodisperse relaxation functions.

2.6.1 Dumbbell

For simplicity, we first simulate a melt of dumbbells, i.e. $N = 2$. The radial distribution function, $g(r)$, is a measure of correlations between the particles in a system. It is a measure of probability to find a particle at a distance r away from a given reference particle. In this paragraph, we will measure $g(r)$ for the dumbbells. The distance between two dumbbells is defined as the distance between the center-of-mass of these two dumbbells. And instead of calculating the distance between each pair of the dumbbells only, the angle θ between the bond vectors of these two dumbbells is measured as well

$$\theta_{ij} = \arccos\left(\frac{|\mathbf{r}_i \cdot \mathbf{r}_j|}{|\mathbf{r}_i| |\mathbf{r}_j|}\right) \quad (2.23)$$

$$r_{ij} = \left| \frac{\mathbf{R}_{i1} + \mathbf{R}_{i2}}{2} - \frac{\mathbf{R}_{j1} + \mathbf{R}_{j2}}{2} \right| \quad (2.24)$$

where i, j are the indexes of the dumbbells, $\mathbf{r}_i = \mathbf{R}_{i2} - \mathbf{R}_{i1}$ is the bond vector of dumbbell i and r_{ij} is the distance between dumbbells i and j .

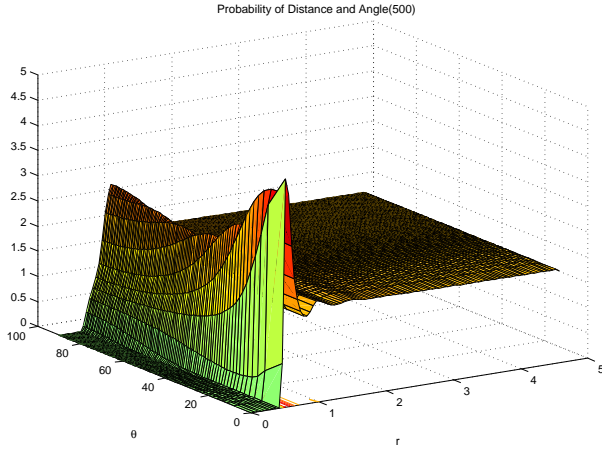


FIGURE 2.29: $g(r, \theta)$ of the system with $\rho=0.6\sigma^{-3}$.

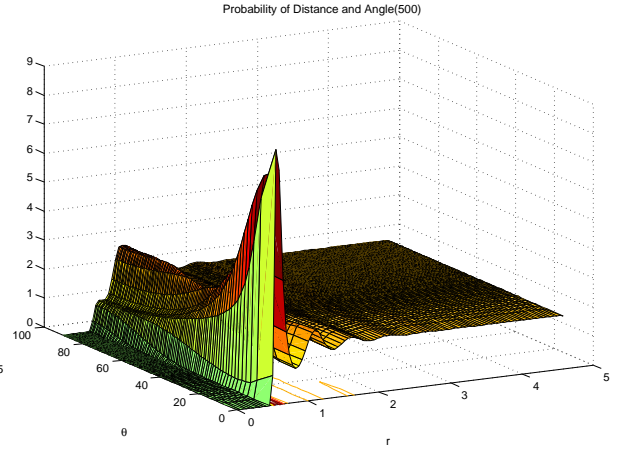


FIGURE 2.30: $g(r, \theta)$ of the system with $\rho=0.85\sigma^{-3}$.

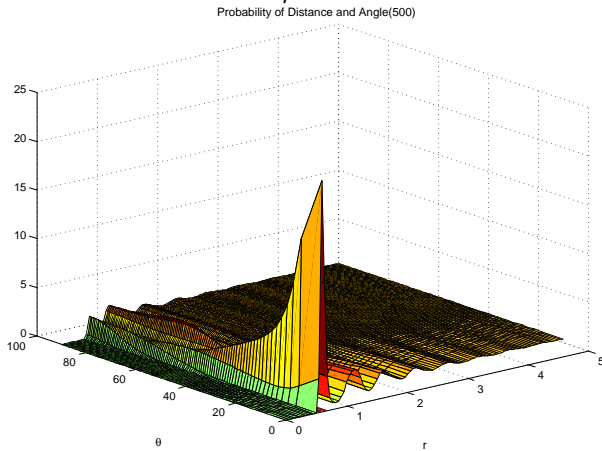


FIGURE 2.31: $g(r, \theta)$ of the system with $\rho=1.15\sigma^{-3}$.

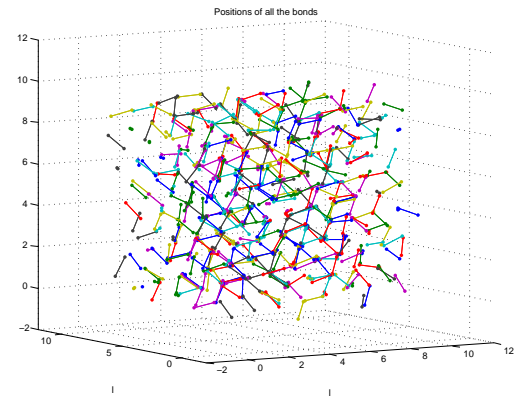


FIGURE 2.32: Bonds positions in the simulation box of the system with $\rho = 1.15\sigma^{-3}$.

$g(r, \theta)$ was calculated in the systems with different densities (Fig. 2.29 and Fig. 2.30) and $g(r) = \int_0^{\pi/2} g(r, \theta) d\theta$. From these two figures, we can see the following general features:

- If the distance between two dumbbells is around σ , there is higher probability that two dumbbells are parallel to each other.
- If two dumbbells' distance is around 1.5σ , there is higher probability that two dumbbells are perpendicular to each other.
- If the density is high enough, there are also some peaks at $\theta = 60^\circ$.

In these results, the excluded volume effect is the only source of the orientational coupling. If the density of the system increases, the probed dumbbell

would be trapped by the surrounding dumbbells and feel difficult to jump out the “cage”. The coupling effect between two dumbbells at short distance becomes larger with increasing density. The system crystallized if we increase density to $1.15\sigma^{-3}$ (Fig.2.32), with dominant orientation being $\theta = 60^\circ$, which due to the spheres are close packed. Now we turn our attention to the same effect in polymer chains.

2.6.2 Short-range orientational coupling

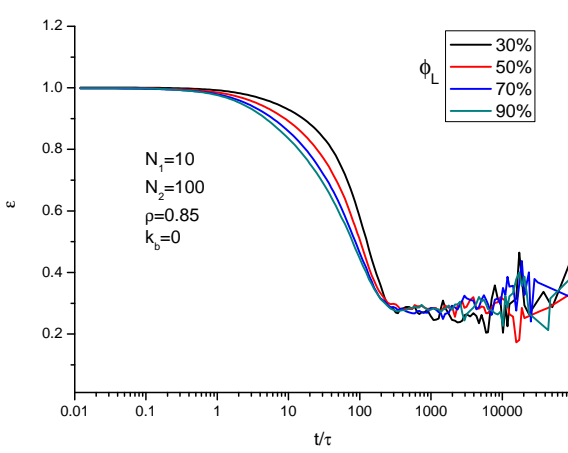
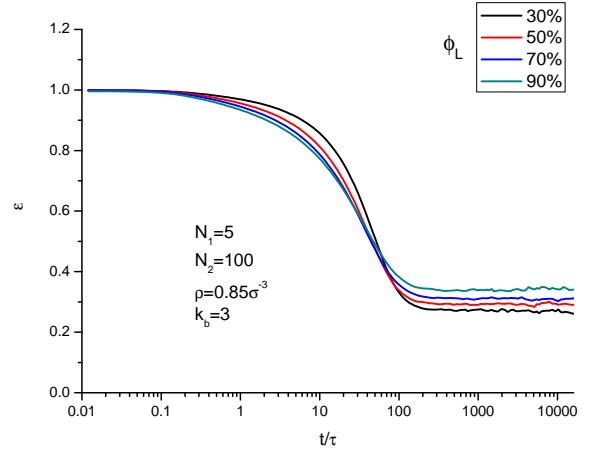
Orientational cooperativity in polymer melts can arise due to short-range forces acting on the segmental level. It was discussed by Doi *et al.*[33] that the strength of this interaction can be measured by using the bulk and shorter component relaxations after short chain’s relaxation time(Eq.2.22).

In our notations, this coupling parameter ε can be expressed as following:

$$\varepsilon(t) = \frac{E_s(t)}{S_{tot}(t)} \frac{S_{tot}(0)}{E_s(0)} = \frac{E_s(t)}{S_{tot}(t)} = \frac{A_s(t) + C_{ss}(t)\varphi_s + C_{sl}(t)\varphi_l}{S_{tot}(t)} \quad (2.25)$$

It is shown in Fig.2.33 and Fig.2.34 for different composition of the binary blends of flexible and semi-flexible systems. In flexible systems, short and long components have chain lengths $N_1=10$ and $N_2=100$ respectively and all ε equal to 0.28 after short component relaxed. However, this coupling parameters are different in the particular semi-flexible systems with $N_1= 5, N_2=100$ in Fig.2.34. The range of ε is from 0.28 to 0.35 depending on the concentration of the short component, which is caused by the dynamics of the chain ends. If we use longer short chains($N_1=30$), ε are the same at different compositions(≈ 0.35). The results from our simulations are consistent with Baljon’s results[36].

However, Eq.2.25 does not include the cross-correlation function between the long chains $C_{ll}(t)$, which is an important contribution to the relaxation function at longer times. This exclusion indicates that ε is not an appropriate parameter to present coupling effect at longer times. And this coupling parameter can only be measured after short chains were relaxed. If the lengths of short and long


 FIGURE 2.33: Coupling parameter ε in binary blends of flexible chains.

 FIGURE 2.34: Coupling parameter ε in binary blends of semi-flexible chains.

components are not very different, it is extremely difficult to obtain this coupling parameter, and impossible in monodisperse melts. We would like to have a more universal coupling parameter to express the coupling effect, which is independent of the chain lengths and the composition of the melts. In the next section we will introduce another time-dependent parameter $\kappa(t)$ which measures how important the orientation cross-correlation function is in the total relaxation function.

2.6.3 Time-dependent coupling parameter in flexible systems

We would like to describe orientational coupling with one universal function, which captures the behaviour of both monodisperse melts and their mixtures. In particular, it should allow prediction of all cross-correlation curves in Fig.2.23 from monodisperse behaviour. We find these requirements are met by the function we call a time-dependent coupling parameter $\kappa(t)$:

$$\kappa(t) = \frac{\sum_i \sum_j \varphi_i \varphi_j C_{ij}(t)}{S_{tot}(t)} \quad (2.26)$$

where i, j are the component indexes, φ_i is the volume fraction of component i , $C_{ij}(t)$ is the cross-correlations between components i and j in the system. Clearly

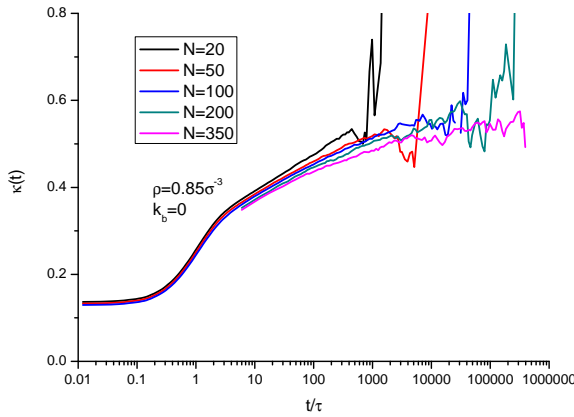


FIGURE 2.35: Coupling parameter $\kappa(t)$ in monodisperse melts.

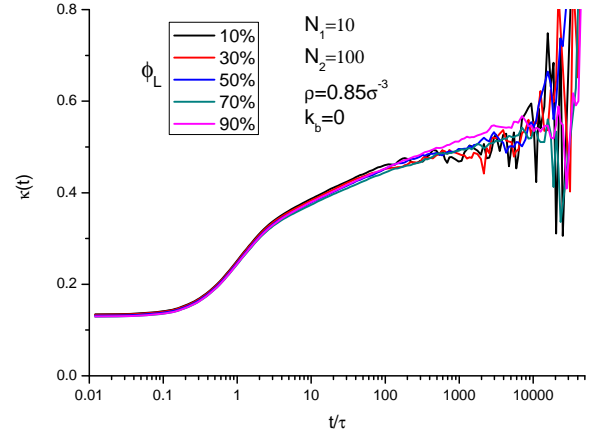


FIGURE 2.36: Coupling parameter $\kappa(t)$ in bidisperse melts.

$\kappa(t)$ has a simple physical interpretation of relative importance of cross-correlations at different times.

$\kappa(t)$ of monodisperse melts of different chain lengths ranging from $N=20$ to $N=350$ which have approximately 0.5 to 7 entanglements are shown in Fig.2.35. $\kappa(t)$ of binary blends of $N_1=10$, $N_2=100$ with different compositions are shown in Fig.2.36. These results demonstrate that $\kappa(t)$ has a universal behavior, which is independent on molecular weight and blends composition. Indeed, all plots collapse onto the same master curve for several bidisperse melts and for different chain lengths. These two figures illustrate that the role of cross-correlations increase with time, rising from 12.9% at $t = 0$ to about 50% at later time until the chain is totally relaxed. We also observe that the $\kappa(t)$ of $N=350$ in Fig.2.35 is slightly smaller than the ones from other systems. Insufficient simulation box size or incomplete relaxation are suspected to be the reason.

2.6.4 Coupling effects in monodisperse melts at different densities

In this section we will show the relaxation and the coupling effect of monodisperse melts at different densities. Total orientation relaxation function $S(t)$ and the one multiplied by $t^{1/2}$ are shown in Fig.2.37 and Fig.2.38 respectively. In the systems with low densities $\rho < 0.4\sigma^{-3}$, $S(t)$ has two relaxation processes separated by about

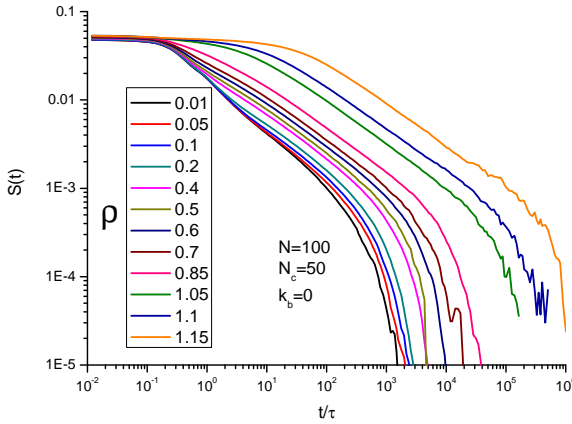


FIGURE 2.37: Total orientation relaxation function $S(t)$ in monodisperse melts with different densities.

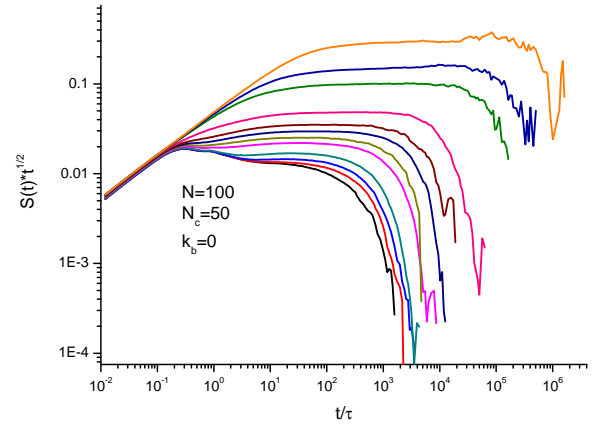


FIGURE 2.38: Total orientation relaxation function $S(t)$ in monodisperse melts with different densities.

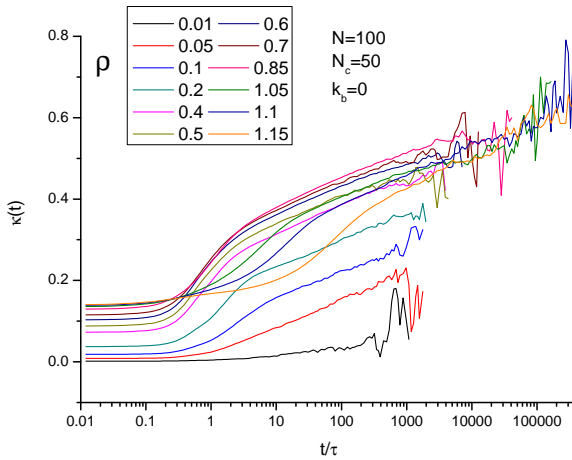


FIGURE 2.39: Coupling parameter $\kappa(t)$ in monodisperse melts with different densities.

$t = 5\tau$ (Fig. 2.37). Short time process is associated with bond length relaxation, whereas long time is Rouse-like chain orientation relaxation. In the systems with higher densities, the total orientation only have one relaxation procedure and keep as constant until $t \approx 10\tau$, and then relaxes with the slope equal to -0.5 .

The time-dependent coupling parameter $\kappa(t)$ at different densities is shown in Fig. 2.39. The static coupling $\kappa(0)$ is a monotonically increasing function of density. The more molecules there are in the same volume, the more collisions will happen, which will enhance the coupling between different molecules. At the extremely small density ($\rho = 0.01\sigma^{-3}$), $\kappa(t)$ increases with time but not significantly. At higher densities, $\kappa(t)$ keeps constant until $t \approx 0.5\tau$, and then increases until the polymer chain is totally relaxed. After comparing $\kappa(t)$ from the systems with densities $\rho = 0.85, 1.05, 1.10, 1.15\sigma^{-3}$, we can observe that all $S(t)$ and all

$\kappa(t)$ curves can be superimposed to each other by shifting the time axis. This is a manifestation of time-density superposition, similar to the time-temperature superposition.

2.6.5 Coupling effects by entanglements

In order to find out whether entanglements play any role in the observed coupling, we simulated a system with softer non-bonded and bonded potentials

$$U_{nb}(r) = \frac{3}{4}u_0(r^2 - r_{nb}^2)^2; \quad r < r_{nb} \quad (2.27)$$

$$U_b(r) = \frac{k_r}{2}(r - r_b)^2 \quad (2.28)$$

where $r_{nb} = 1.6$, $r_b = 1.222$, $u_0 = 2.2$, and $k_r = 20$ in flexible system. This system has approximately the same structural properties of the chains with “harder” system at long distances (i.e. it has exactly the same average squared internal distances $\langle R_{ij}^2 \rangle$ and thus the same C_∞)(Fig.2.40), but allows easy chain crossing. We found that $\kappa(t)$ reached the same plateau(around 50%) as the original “hard” system (Fig.2.41). The only difference is that the terminal relaxation time is smaller than before since the chains obeyed Rouse-like dynamics(Fig.2.42). Indeed we observed that the mean-squared displacements of the middle and end beads were in perfect agreement with the Rouse model(Fig.2.43). The results of the original entangled and soft potential simulations show that the role of entanglements in orientational coupling is negligible in this particular system, contrary to the recent argument of Deutsch and Pixley[37].

To further probe the role of entanglements we computed $\kappa(t)$ for slightly semi-flexible chains with stiffness parameter $k_b = 3$. These systems have significantly smaller $N_e \approx 15$ and thus more entanglements. $\kappa(t)$ are shown in Fig.2.44 for both entangled and soft systems. In this case the coupling at time zero is higher since the semi-flexible chains have more contacts with other chains than their fully flexible counterpart. At later times $\kappa(t)$ increases above 60%. This is again compared with the corresponding softer system with parameters $u_0 = 2.1$, $k_r = 34$ in

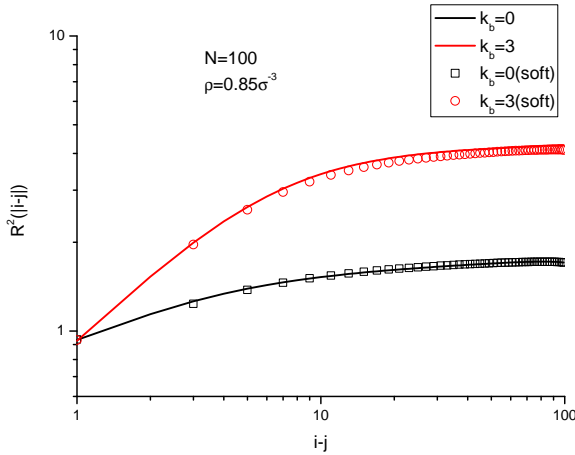


FIGURE 2.40: Average squared internal distances of the polymer chain in different systems.

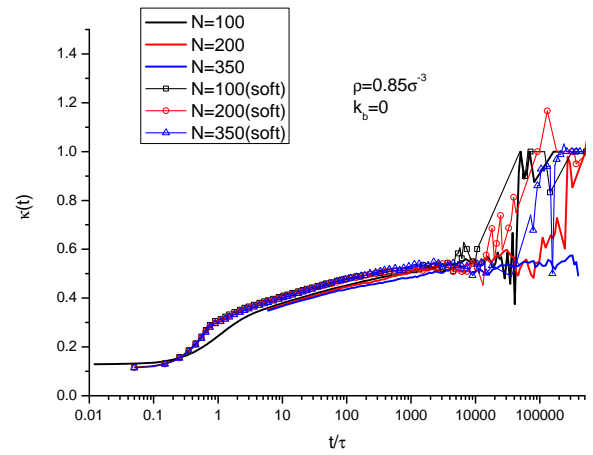


FIGURE 2.41: Coupling parameter $\kappa(t)$ of soft potential in monodisperse melts.

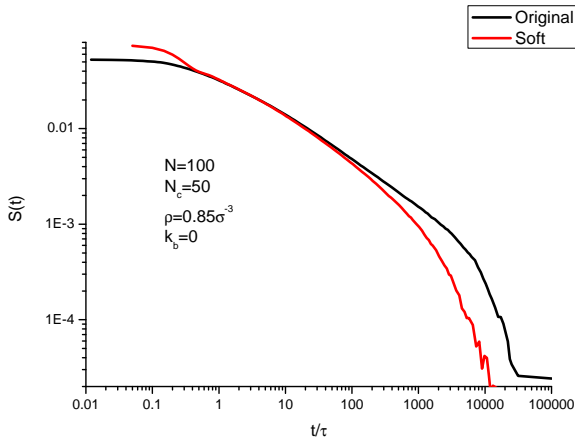


FIGURE 2.42: Total relaxation function of orientation in original hard and soft systems.

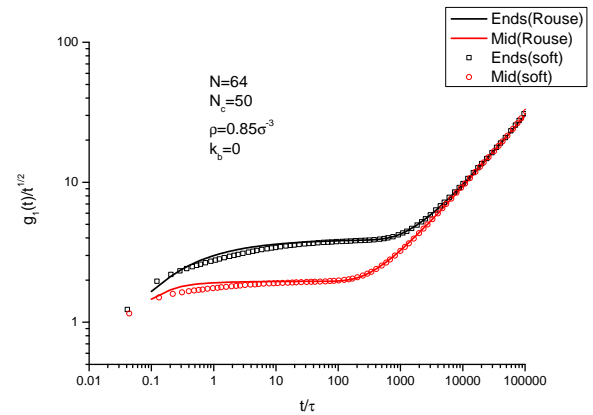


FIGURE 2.43: Mean-square displacement of middle and end monomers of Rouse systems.

Eq.(2.27) and Eq.(2.28) adjusted to match the internal distances $\langle R_{ij}^2 \rangle$ in Fig.2.44. The results are again very close, although some difference shows up at late time. The coupling parameter for soft systems seems to reach a plateau, whereas it continues to increase slowly for the Lennard-Jones chains. This can be interpreted as the influence of entanglements. Alternatively, one can say that in entangled system chains spend more time in contact with the same other chains, and thus become more coupled to each other. In any case, the role of entanglements seem to be minor and indirect. In entangled systems, the single chain models like the tube or slip-links models aim to predict the auto-correlation relaxation function in blends. Observed orientation relaxation of short chains will be affected by the long chains via orientation coupling and the tube or slip-links models predictions

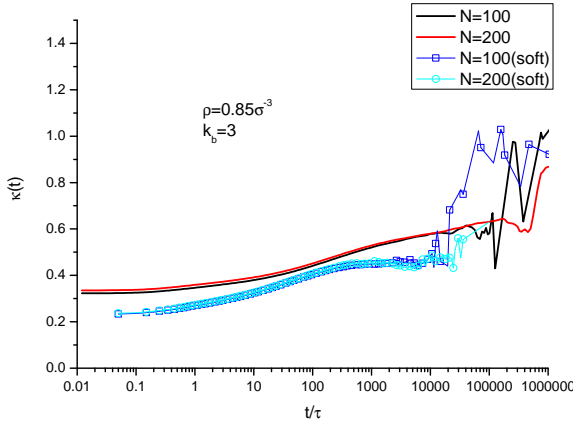


FIGURE 2.44: Coupling parameter $\kappa(t)$ of soft potential in monodisperse melts of semi-flexible chains.

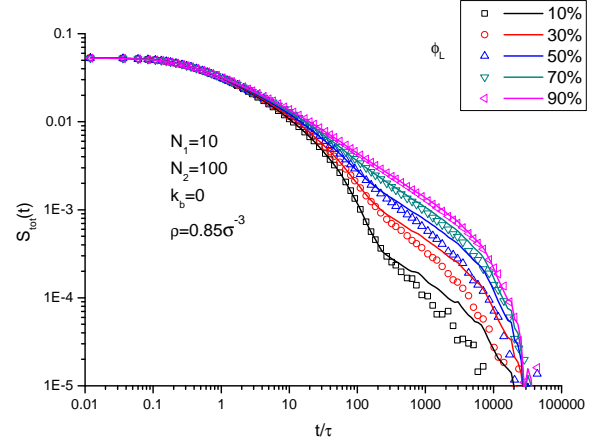


FIGURE 2.45: Prediction from Eq.(2.30)(lines) and the measured total relaxation(symbols) of binary blend of flexible systems.

must be modified accordingly.

2.6.6 Universality of our coupling parameter

The universality of time-dependent coupling parameter $\kappa(t)$ has non-trivial consequences for polymer blends. Indeed, a requirement that $\kappa(t)$ is the same in monodisperse melts and in their blends can be written as

$$\begin{aligned}
 1 - \kappa(t) &= \frac{A_s(t)\varphi_s + A_l(t)\varphi_l}{S_{tot}(t)} = \frac{A_s^{mono}(t)}{S_s^{mono}(t)} = \frac{A_l^{mono}(t)}{S_l^{mono}(t)} \\
 \Rightarrow \frac{A_s(t)\varphi_s + A_l(t)\varphi_l}{S_{tot}(t)} &= \frac{\varphi_s A_s^{mono}(t) + \varphi_l A_l^{mono}(t)}{\varphi_s S_s^{mono}(t) + \varphi_l S_l^{mono}(t)} \quad (2.29)
 \end{aligned}$$

It immediately follows from here that if the auto-correlation functions are the same in the mixtures as in the monodisperse systems ($A_s(t) = A_s^{mono}(t)$ which is true for unentangled systems), the simple mixing rule for the total orientation relaxation

$$S_{tot}(t) = \varphi_s S_s^{mono}(t) + \varphi_l S_l^{mono}(t) \quad (2.30)$$

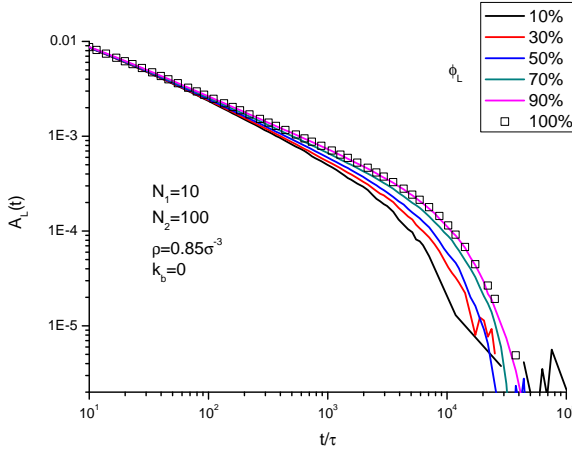


FIGURE 2.46: Auto-correlation function of long component $A_L(t)$ in binary blends and monodisperse melt.

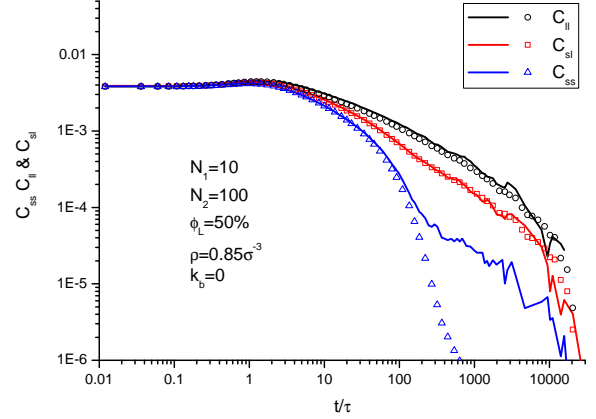


FIGURE 2.47: Components of Cross-correlation functions from simulations (lines) and predictions from Eqs. 2.34, 2.31, 2.32 (open symbols).

is not spoiled by the orientation coupling. The total relaxation function of flexible chains and the predictions from Eq.(2.30) are shown in Fig.2.45. Slight disagreement is observed at late times. We suppose the reason is that the concentration of the short component affects the self-relaxation function of the long component which make $A_L(t)$ different from the one in monodisperse melt $A_L^{mono}(t)$ (Fig.2.46). The more short chains the system has, the more chain ends in the melt which will change the dynamics of the system.

Universality of $\kappa(t)$ also means that one can relate different components of cross-correlation to the auto-correlation functions. In unentangled systems, it is reasonable to believe that the cross-correlation function between different short chains $C_{ss}(t)$ in binary blends has the same physical meaning as the one in the monodisperse melt of short chains. The only difference of $C_{ss}(t)$ between these two systems is that the probability of two short chains meeting each other in binary blends is φ_s^2 of the probability of two chains meeting each other in short chain monodisperse melt. Thus we can claim that

$$C_{ss}(t) \approx C_{ss}^{mono}(t) = S_s^{mono}(t)\kappa(t) \quad (2.31)$$

The same is true for the cross-correlation function between the long chains

$$C_{ll}(t) \approx C_{ll}^{mono}(t) = S_l^{mono}(t)\kappa(t) \quad (2.32)$$

From the definition of $\kappa(t)$ we can derive

$$2\varphi_s\varphi_l C_{sl}(t) + \varphi_s^2 C_{ss}(t) + \varphi_l^2 C_{ll}(t) = S_{tot}(t)\kappa(t) \quad (2.33)$$

Substituting Eqs.(2.31), (2.32) and (2.30) into Eq.(2.33), we obtain

$$2C_{sl}(t) \approx (S_s^{mono}(t) + S_l^{mono}(t))\kappa(t) \quad (2.34)$$

Predictions given by these expressions are shown by open symbols in Fig.2.47. They are in perfect agreement with the curves measured in binary blends apart from the long time behavior of $C_{ss}(t)$, which is affected by the secondary coupling of the two short chains via an intermediate long chain. Eqs.2.31-2.33 in turn provide the response of the short and long component relaxation $E_s(t)$, $E_l(t)$

$$\begin{aligned} E_s(t) &= A_s(t) + C_{ss}(t)\varphi_s + C_{sl}(t)\varphi_l \\ &= A_s(t) \left(1 + \frac{\kappa(t)}{1 - \kappa(t)} \frac{1 + \varphi_s}{2}\right) + A_l(t) \left(\frac{\kappa(t)}{1 - \kappa(t)} \frac{\varphi_l}{2}\right) \\ &\approx A_s^{mono}(t) \left(1 + \frac{\kappa(t)}{1 - \kappa(t)} \frac{1 + \varphi_s}{2}\right) + A_l^{mono}(t) \left(\frac{\kappa(t)}{1 - \kappa(t)} \frac{\varphi_l}{2}\right) \\ &= S_s^{mono}(t) + \frac{\kappa(t)}{2} \varphi_l [S_l^{mono}(t) - S_s^{mono}(t)] \end{aligned} \quad (2.35)$$

$$\begin{aligned} E_l(t) &= A_l(t) + C_{ll}(t)\varphi_l + C_{sl}(t)\varphi_s \\ &= A_l(t) \left(1 + \frac{\kappa(t)}{1 - \kappa(t)} \frac{1 + \varphi_l}{2}\right) + A_s(t) \left(\frac{\kappa(t)}{1 - \kappa(t)} \frac{\varphi_s}{2}\right) \\ &\approx A_l^{mono}(t) \left(1 + \frac{\kappa(t)}{1 - \kappa(t)} \frac{1 + \varphi_l}{2}\right) + A_s^{mono}(t) \left(\frac{\kappa(t)}{1 - \kappa(t)} \frac{\varphi_s}{2}\right) \\ &= S_l^{mono}(t) + \frac{\kappa(t)}{2} \varphi_s [S_s^{mono}(t) - S_l^{mono}(t)] \end{aligned} \quad (2.36)$$

For the times longer than the relaxation time of the short component τ_s these

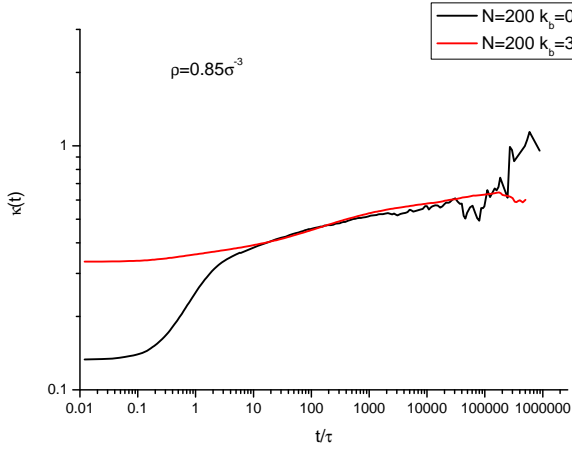
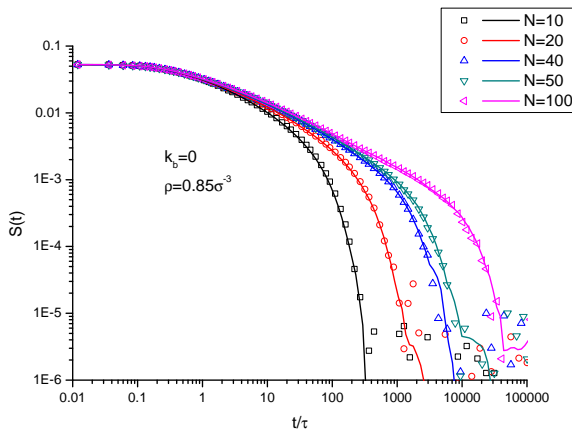

 FIGURE 2.48: $\kappa(t)$ of flexible and semi-flexible chains.


FIGURE 2.49: Total relaxation functions(symbols) and the prediction(lines) of flexible chains from Eq.2.38.

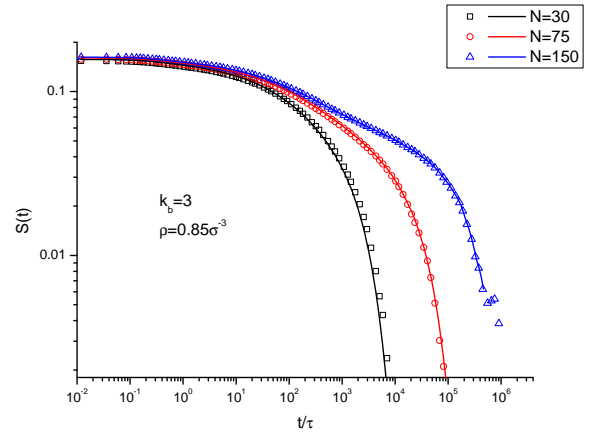


FIGURE 2.50: Total relaxation functions(symbols) and the prediction(lines) of semi-flexible chains from Eq.2.38.

equations provide a simple relation of our coupling parameter with the Doi's parameter:

$$\begin{aligned}
 \varepsilon(t) &= \frac{E_s(t)}{S_{tot}(t)} \\
 &= \frac{S_s^{mono}(t) + \frac{\kappa(t)}{2} \varphi_l [S_l^{mono}(t) - S_s^{mono}(t)]}{\varphi_s S_s^{mono}(t) + \varphi_l S_l^{mono}(t)} \\
 &\approx \frac{1}{2} \kappa(t) \quad (t > \tau_s).
 \end{aligned} \tag{2.37}$$

2.6.7 Usage of the universal coupling parameter in monodisperse melts

In this section, we aim to predict the total orientation relaxation function by using the auto-correlation functions of the chains and the universal coupling parameter $\kappa(t)$. According to the universality of $\kappa(t)$ in monodisperse and bidisperse melts, we can obtain an accurate $\kappa(t)$ by running a monodisperse simulation with sufficiently long chains. $\kappa(t)$ of flexible and semi-flexible chains used in all the calculations in this section are shown in Fig.2.48. The prediction of total relaxation function $S(t)$ is

$$S(t) = \frac{A(t)}{1 - \kappa(t)} \quad (2.38)$$

where $A(t)$ is the auto-correlation function of the chain. The total relaxation function and the predicted ones are shown in Fig.2.49 and Fig.2.50 for flexible and semi-flexible chains respectively. The predictions have a good agreement with the desired total relaxation functions in both flexible and semi-flexible chains except the semi-flexible chains with chain length $N = 30$ (black lines and symbols in Fig.2.50). It shows that our prediction slightly underestimates the coupling effect for this short semi-flexible chains.

2.6.8 Usage of the universal coupling parameter in binary blends

Now we would like to use the same strategy to predict the total orientation relaxation function of binary blend by using the auto-correlation function of each component in the blend and the universal coupling parameter $\kappa(t)$. The prediction of the total orientation relaxation function of binary blend $S_{tot}(t)$ is

$$S_{tot}(t) = \frac{\varphi_s A_s(t) + \varphi_l A_l(t)}{1 - \kappa(t)} \quad (2.39)$$

As the statistics of auto-correlation functions are much better than the total relaxation function because it is an average over many correlation functions (see

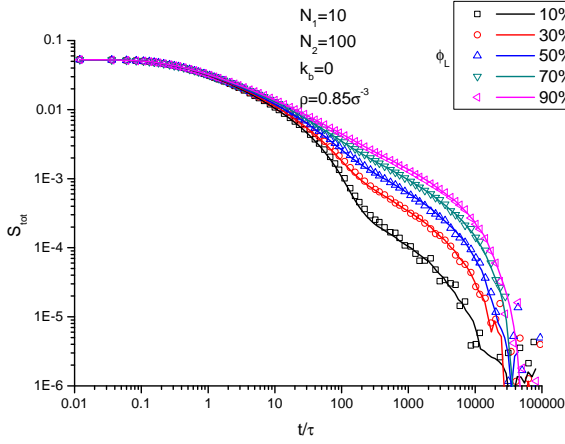


FIGURE 2.51: Total relaxation functions(symbols) and the prediction(lines) of flexible chains from Eq.2.39.

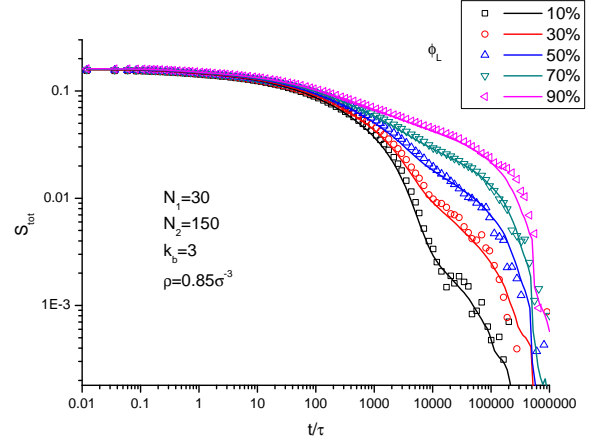


FIGURE 2.52: Total relaxation functions(symbols) and the prediction(lines) of semi-flexible chains from Eq.2.39.

Eqs.(2.7) and (2.11)), we can obtain an accurate estimation of the total relaxation function by using Eq.(2.39). Chain lengths $N_1=10, N_2=100$ are chosen for the binary blends of flexible chains, and $N_1=30, N_2=150$ for the semi-flexible systems. The predictions are plotted together with the total relaxation functions of binary blends for different compositions in Fig.2.51 and Fig.2.52. We see that Eq.(2.39) gives a stable method to obtain the total orientation relaxation function of binary blends, especially the ones which have low concentration of the longer component. In the systems with a low concentration of the long chains, it is very difficult to obtain an accurate total relaxation function through direct calculations. However, the prediction from Eq.(2.39) can give much smoother curves and the agreement is quite good.

Furthermore, suppose the auto-correlation functions of each component in monodisperse and bidisperse melts are the same, which is true in unentangled systems, then we can use the auto-correlation functions of monodisperse melts instead of the ones in bidisperse melts. The comparisons are shown in Fig.2.53 and Fig.2.54. The predictions are in good agreement with the measured ones at short times but not at long times, which is caused by the difference between the auto-correlation functions of long component in monodisperse melt and the one in bidisperse melts

$$A_l^{mono}(t) \neq A_l(t) \quad (2.40)$$

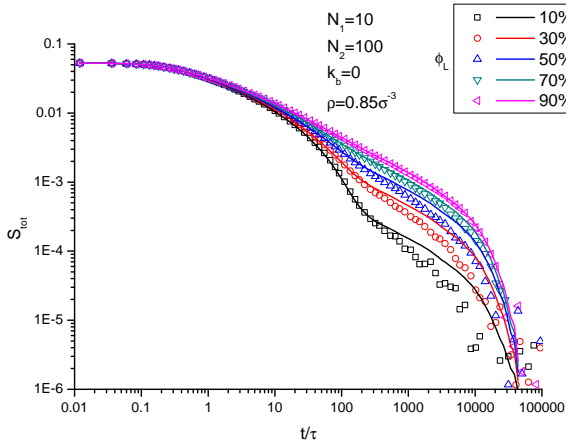


FIGURE 2.53: Total relaxation functions(symbols) and the prediction(lines) of flexible chains.

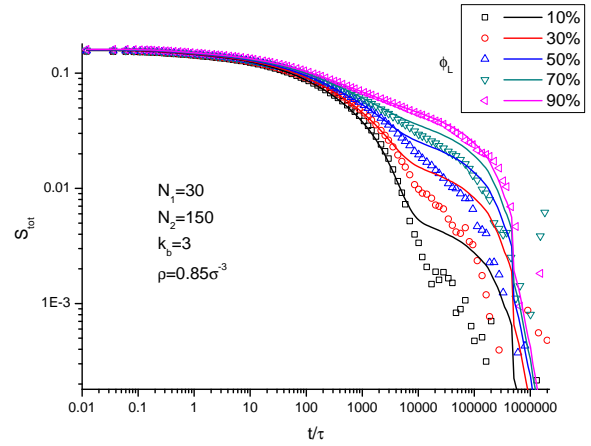


FIGURE 2.54: Total relaxation functions(symbols) and the prediction(lines) of semi-flexible chains.

However, if the long and short chains have widely separated molecular weights M_s and M_l , the slow relaxation behaviour of the long chain in the blend is similar to that in a solution having the same volume fraction φ_l of these chains[38]. The molecular weight of solvent is well below the entanglement molecular weight and the relaxation of the long chain in the solution is only affected by their mutual entanglements. In the binary blends, the short chains are in a slightly entangled state, and the relaxation of the long chains is affected by the entanglements with the short chains. According to constraint release mechanism, the relaxation of the long chains is dominated by the CR mechanism if the Struglinski-Graessley parameter $r_{SG} = M_l M_c^2 / M_s^3$ is larger than a threshold value of about 0.5. In our simulations of entangled binary blends, the SG parameters is 1.25 for semi-flexible chains, which is larger than the threshold value.

Now we are going to check whether the length of the short chain affects the relaxation of the long chain or not in the flexible systems. $N=100$ is chosen for the long chains as in previous runs, and the dumbbells are chosen for representing the solvent. Auto-correlation function $A_l(t)$ of long chains are in good agreement in these two systems(Fig.2.55). Now we can use the auto-correlation function of long chain in the solvent to predict the total relaxation function of binary blends. The predictions and the target relaxation functions are both shown in Fig.2.56.

Thus a qualitative agreement between the solutions and the blends suggest that in this case the short chains in the blends behave as a solvent in the terminal

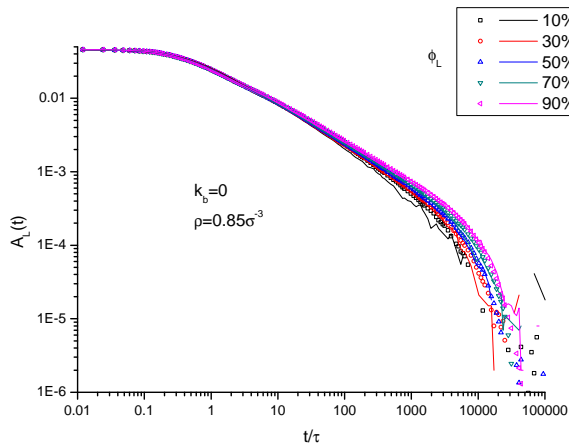


FIGURE 2.55: Auto-correlation function $A_l(t)$ of long chains in binary blends(symbols) and solutions(lines).

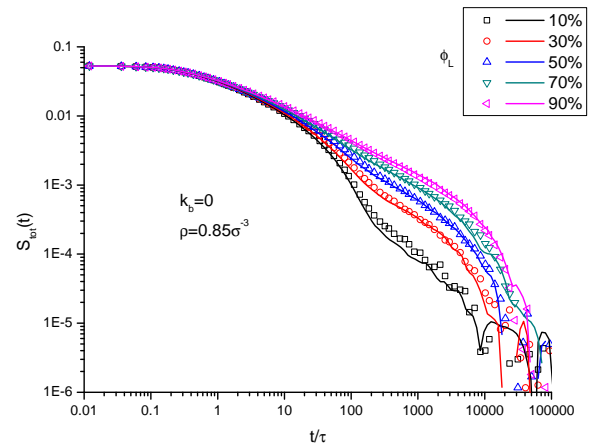


FIGURE 2.56: Total relaxation functions(symbols) and the prediction(lines) of flexible chains.

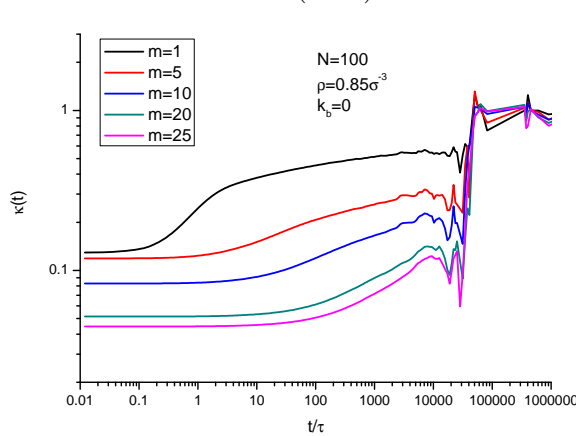


FIGURE 2.57: Coupling parameter $\kappa(t)$ of flexible chains at different coarse-graining level. The starting point $\kappa(0)$ drops from 11% to 3% as the coarse-graining level increases.

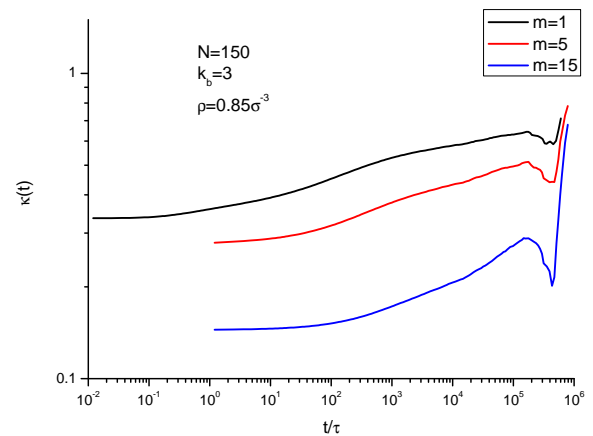


FIGURE 2.58: Coupling parameter $\kappa(t)$ of semi-flexible chains at different coarse-graining levels.

regime of the blend. Then the auto-correlation function of the long chains in binary blends can be obtained by measuring the auto-correlation function of the long chains in solution which has the same volume fraction of long chain as the binary blends. Then we can use this auto-correlation functions from solution to predict the total orientation relaxation functions in binary blends. However, this is expected to break for smaller values of Struglinski-Graessley parameter.

2.6.9 Coupling between the coarse-grained blobs

In this section, we investigate the coupling effect in coarse-grained polymer chains. m monomers on the chain in sequence are coarse-grained into one “blob” whose position is defined as the center-of-mass of these monomers, where m is called the coarse-graining level. We define the coarse-grained orientation tensor in terms of “blob” positions. We show the coupling parameter $\kappa(t)$ at different coarse-graining level for flexible chain with $N=100$ in Fig.2.57 and for the semi-flexible chains with $N = 150$ in Fig.2.58. We can see that the coupling effect reduces significantly as the coarse-graining level m increases, which means that for large m the total orientation relaxation function of the coarse-grained system is almost the same as the sum of auto-correlation functions. In other words, the coupling effect is negligible at large coarse-graining level. At every coarse-graining level, the coupling parameter $\kappa(t)$ stays constant at short times, and then increases. The larger the coarse-graining number is, the longer this time of keeping constant is. More investigation is needed along these lines.

2.7 Conclusions

In this chapter we investigated the stress and orientational relaxation in monodisperse and bidisperse melts. In monodisperse melts, the terminal relaxation time is proportional to the square and cubic of the molecular weight if the chain length is smaller or longer than the entanglement length respectively. In binary blends, the terminal relaxation time τ_d depends on the composition of the mixture. Cross-correlations between orientation tensors of different chains in polymer melt reveal a rich and fascinating picture. Molecular dynamics simulations show that the role of cross-correlations in total orientational relaxation function increases with time, reaching the same amplitude as the auto-correlations. We introduced a time-dependent coupling parameter $\kappa(t)$ and found that it provides a universal description of coupling effects independent of chain length and blend composition. Instead of using static Doi’s coupling parameter ε , which is valid only after short

chain relaxation time in binary blends, we can use $\kappa(t)$ to quantify coupling effects at any times in both monodisperse and bidisperse melts. Universality of $\kappa(t)$ means that we can predict any correlation function in binary blends for unentangled chains providing one knows relaxation functions in monodisperse melts and $\kappa(t)$ (also measured from monodisperse melts). In binary blends with low concentration of long component, it is extremely difficult to obtain reliable data for the total relaxation of the system. However, now we can use universal $\kappa(t)$ and self-relaxation functions $A_s(t)$ and $A_l(t)$ to predict the total relaxation function $S_{tot}(t)$ with much better accuracy.

One of the main conclusions of this chapter is that the orientation coupling is time-dependent, with the relative role of cross-correlations increasing by a factor of about 4 towards longer times. This means that any static calculations will only be able to provide a small value $\kappa(0)$, whereas the important long-time coupling can be only obtained by dynamics calculations. This probably explains the discrepancy observed by Baljon *et al.*[36]. This also suggests that recent static calculations by Semenov[39] will not be able to provide $\kappa(t)$ at long times.

Chapter 3

Microscopic simulations of melts in start-up shear

3.1 Overview

In real world, a rheological measurement tells one how “hard” or “soft” the material is, which depends on the time scale at which the material is probed. A rheometer is normally used to measure rheological properties of a complex fluid as a function of rate or frequency of deformation. There are two widely used methods to obtain rheological property of the complex fluid. One is applying a shear flow on the material and measuring the resulting stress, the other is applying a shear stress and measuring the resulting shear strain. As mentioned before, the shear stress σ is the force that a flowing liquid exerts on a unit surface in the direction parallel to the flow. The shear viscosity η is then defined as

$$\eta = \frac{\sigma}{\dot{\gamma}} \quad (3.1)$$

where $\dot{\gamma}$ is the shear rate applied to the system. Nowadays the experimental equipments are improved dramatically comparing to several decades ago. However, these experiments still suffer from complications such as wall slip[40][41], edge

fracture[42] and shear banding[43][44]. As a result, very few experimental data have been published that can be used by the theoreticians.

The Doi-Edwards tube theory[1] is successful in predicting qualitative properties of entangled polymer fluids. However, the original theory can not fit linear relaxation spectra(G' and G'') as it misses several important physical processes: contour length fluctuations, constraint release, and longitudinal stress relaxation along the tube. All of these processes use either uncontrolled approximations or fail to include all of them at the same time. Likhtman and McLeish[17] combined self-consistent theories for contour length fluctuations and constraint release with reptation theory, and produced excellent agreement between theory and experiment in the linear regime. However, there is no definitive theory to describe the features for non-linear flows. The assumptions of Doi-Edwards theory suggest that it is possible to apply the parameters fitting the linear data to the non-linear data. However, it has been proven that the theory fails in this case. If steady state shear stress σ_{xy} is plotted as a function of shear rate $\dot{\gamma}$, the model predicts a shear stress maximum when the shear rate goes beyond the reciprocal of the reptation time($\dot{\gamma} > 1/\tau_d$). However, experimental data showed that steady state shear stress is a monotonically increasing function of shear rate. Two possible mechanisms to rectify this problem are constraint release and chain stretch. Constraint release is an additional relaxation mechanism that states that whenever a chain end passes through a tube segment the constraint imposed by this chain on the confined chain is lost. Hence the confined chain is free to move a distance of order of tube diameter perpendicular to its contour. Constraint release is a self consistent closure of the mean field approximation of the tube model. In the linear regime constraint release is caused by the reptation of the chains. Likhtman and McLeish[17] demonstrated that constraint release had significant effects near the terminal time. In non-linear regime, constraint release becomes more important. Marrucci[45] and Marrucci and Ianniruberto[46] have pointed out that fast flows convect away the polymer molecules surrounding a given polymer chain, and therefore destroy the tube constraining the chain, faster than the chain reptates out of the tube itself. They demonstrated that in non-linear flow chain retraction

is the dominant contribution to the constraint release. Chain stretching describes a mechanism that the length of the occupied tube exceeds its equilibrium value. In the Doi-Edwards model the orientation of the chain relaxes at the reptation time τ_d while the chain stretch occurs at a rate determined by the Rouse time τ_R . These two time scales are well separated in entangled systems. The effect of chain stretch becomes significant when $\dot{\gamma}\tau_R \geq 1$. The Doi-Edwards-Marrucci-Grizzuti (DEMG) theory [47][48][49] adds stretch to the basic DE model. The new theory improves the transient predictions in start-up of shear. The DEMG model predicts that the transient overshoots in shear stress and normal stress grow in size with shear rate and the strain at maximal stress at overshoots grows with shear rate, which were observed experimentally. However, The DEMG theory is less successful in steady state of shear. It still predicts a maximum of shear stress.

In this chapter, steady shear is applied to our molecular dynamics simulations and the properties of the material in both transient and steady states are investigated. Surprisingly, we observe a shear stress maximum at steady state around $\dot{\gamma} \approx 1/\tau_d$ in a sufficiently long chain system, which indicates that a shear banding instability might occur in non-linear flows. Comparison between our results and the existing shear data from the literature is performed. All artifacts from experiments, like the wall slip, edge fracture and shear banding, can be excluded in our simulations. We will introduce the model and the analytic algorithms in section 3.2. Monodisperse melts at different shear rates are investigated and compared with experimental data in section 3.3.

3.2 Model and algorithms

3.2.1 Periodic boundary conditions and equation of motion

The problem of simulating homogeneous flows driven by boundaries is that a microscopic simulation with walls will introduce inhomogeneity into the fluid. This

is an acceptable method if one is interested in nano-confined flows, where the spacial inhomogeneity is important in the simulations. However, if one is concerned with bulk properties far away from the surface, the explicit use of the boundary is inappropriate. An alternative to using “solid” wall boundaries is to drive a flow via a suitable implementation of periodic boundary conditions. The most useful method is using Lees-Edwards boundary conditions[50] for planar shear flow. The original simulation box is replicated in all directions by periodic images. Monomers interact via their pair-potential forces under Newton’s second law. The difference between the periodic boundary condition in equilibrium simulations and the one in non-equilibrium simulations is that the periodic image boxes in different layers have strain difference $N_L L_y \dot{\gamma} t$ in shear direction, where N_L is the number difference of the layers, L_y is the length of the simulation box in y -direction, $\dot{\gamma}$ is the shear rate and t is the shear time.

However, this boundary condition has a serious disadvantage that it takes time for the effects of translation of atoms between boundaries to communicate throughout the fluid, which means a linear velocity profile will not be imposed immediately, but will evolve only after a sufficiently long time. The first homogeneous NEMD algorithms was proposed by Hoover *et al.*[51] which was based on DOLLS Hamiltonian. The effect of the boundary that drives the flow is replaced by a fictitious external field, which guarantees that the required linear velocity profile is maintained. The DOLLS Hamiltonian is written as

$$H_{dolls}(\{\mathbf{r}_i\}, \{\mathbf{p}_i\}, t) = \phi(\{\mathbf{r}_i\}) + \sum_i \frac{\mathbf{p}_i^2}{2m_i} + \sum_i \mathbf{r}_i \cdot \nabla \mathbf{v} \cdot \mathbf{p}_i \Theta(t) \quad (3.2)$$

where $\phi(\{\mathbf{r}_i\})$ is the system potential energy due to interactions between all N atoms, \mathbf{r}_i and \mathbf{p}_i are the laboratory position and peculiar momentum of atom i , $\nabla \mathbf{v}$ is the gradient of the streaming velocity \mathbf{v} , and $\Theta(t)$ is the Heaviside step function. The peculiar momentum is the thermal momentum relative to the streaming momentum of the fluid. This Hamiltonian generates the DOLLS equations of

motion for the system,

$$\dot{\mathbf{r}}_i = \frac{\mathbf{p}_i}{m_i} + \mathbf{r}_i \cdot \nabla \mathbf{v} \quad (3.3)$$

$$\dot{\mathbf{p}}_i = \mathbf{f}_i^\phi - \nabla \mathbf{v} \cdot \mathbf{p}_i \quad (3.4)$$

where \mathbf{f}_i^ϕ is the interatomic force on atom i due to other atoms. But soon after the DOLLS equations of motion were proposed, it was demonstrated by Evans and Morriss[52][53] that, while suitable for simulating flows in the linear regime, they were unsuitable for generating physically realistic shear flow in the non-linear regime. Evans and Morriss performed theoretical and simulation studies to prove that equations of motion called SLLOD did give the correct non-linear response for shear flow[54]. The equations of motion of SLLOD could be written down as

$$\dot{\mathbf{r}}_i = \frac{\mathbf{p}_i}{m_i} + \mathbf{r}_i \cdot \nabla \mathbf{v} \quad (3.5)$$

$$\dot{\mathbf{p}}_i = \mathbf{f}_i^\phi - \mathbf{p}_i \cdot \nabla \mathbf{v} \quad (3.6)$$

where the only difference between DOLLS and SLLOD is that the last term in the force equation is transposed, i.e. $\nabla \mathbf{v} \cdot \mathbf{p}_i \rightarrow \mathbf{p}_i \cdot \nabla \mathbf{v}$. The term ‘‘SLLOD’’ indicates the transpose of ‘‘DOLLS’’. In ‘‘DOLLS’’ equations of motion, a correction force due to x -component of the momentum is added to y -component of the force. The other way round in ‘‘SLLOD’’ equations of motion.

The flow generated by the SLLOD algorithm is not driven by the boundaries of the simulation box. The equations of motion and momentum conservation are sufficient to generate correct velocity gradient. However the SLLOD equation of motion must be used with proper periodic boundary conditions which can be prevented from interfering with the particle trajectories. For the planar Couette flow, Lees-Edwards boundary condition[50] can be used. A so-called Kraynik-Reinelt(KR) boundary condition[55] can be used in planar elongational flows. The compatibility between equations of motion and boundary conditions is essential to ensure that the boundaries do not perturb the system. Otherwise the use of response theory will be invalid.

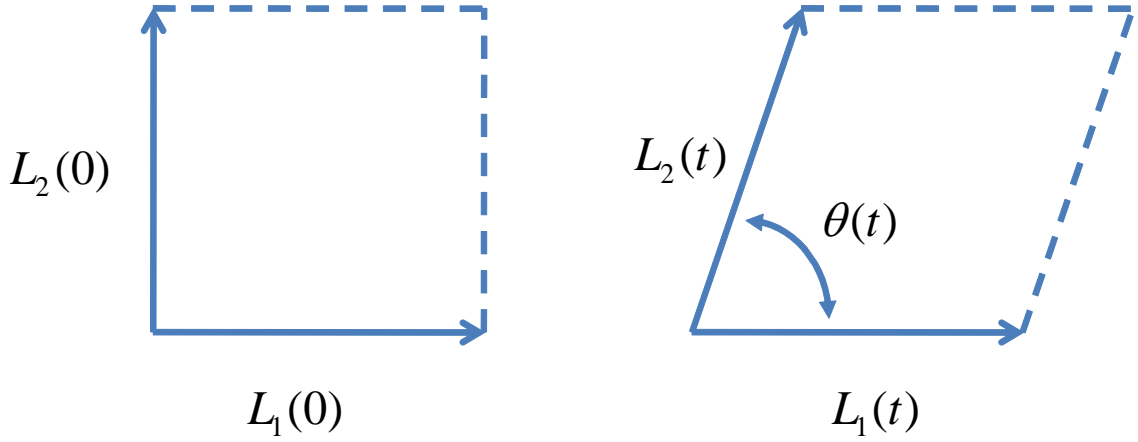


FIGURE 3.1: 2-dimensional representation of simulation box vectors. As $t \rightarrow \infty$, $\theta(t) \rightarrow 0$ and $|\mathbf{L}_2| \rightarrow \infty$, whereas $|\mathbf{L}_1|$ remains the same.

Now we will discuss the implementation of the suitable periodic boundary condition that are compatible with the SLLOD equations of motion for planar Couette flows in which the fluid flows in the x -direction with a velocity gradient $\dot{\gamma}$ in the y -direction. As boundaries must be compatible with the imposed streaming velocity profile, we first calculate the strain rate tensor:

$$\nabla \mathbf{v} = \begin{pmatrix} \frac{\partial v_x}{\partial x} & \frac{\partial v_y}{\partial x} & \frac{\partial v_z}{\partial x} \\ \frac{\partial v_x}{\partial y} & \frac{\partial v_y}{\partial y} & \frac{\partial v_z}{\partial y} \\ \frac{\partial v_x}{\partial z} & \frac{\partial v_y}{\partial z} & \frac{\partial v_z}{\partial z} \end{pmatrix} = \begin{pmatrix} 0 & 0 & 0 \\ \dot{\gamma} & 0 & 0 \\ 0 & 0 & 0 \end{pmatrix} \quad (3.7)$$

The evolution of the boundaries is applied by the same equation of motion. However, the movement of the boundaries have no effect on a thermal velocity.

$$\dot{\mathbf{L}}_k(t) = \mathbf{L}_k(t) \cdot \nabla \mathbf{v} \quad (3.8)$$

where $\mathbf{L}_k(t) = (L_{kx}(t), L_{ky}(t), L_{kz}(t))$ are the initial set of simulation box vectors that define the axes of the boundaries for $k = 1, 2, 3$, which is shown in Fig.3.1.

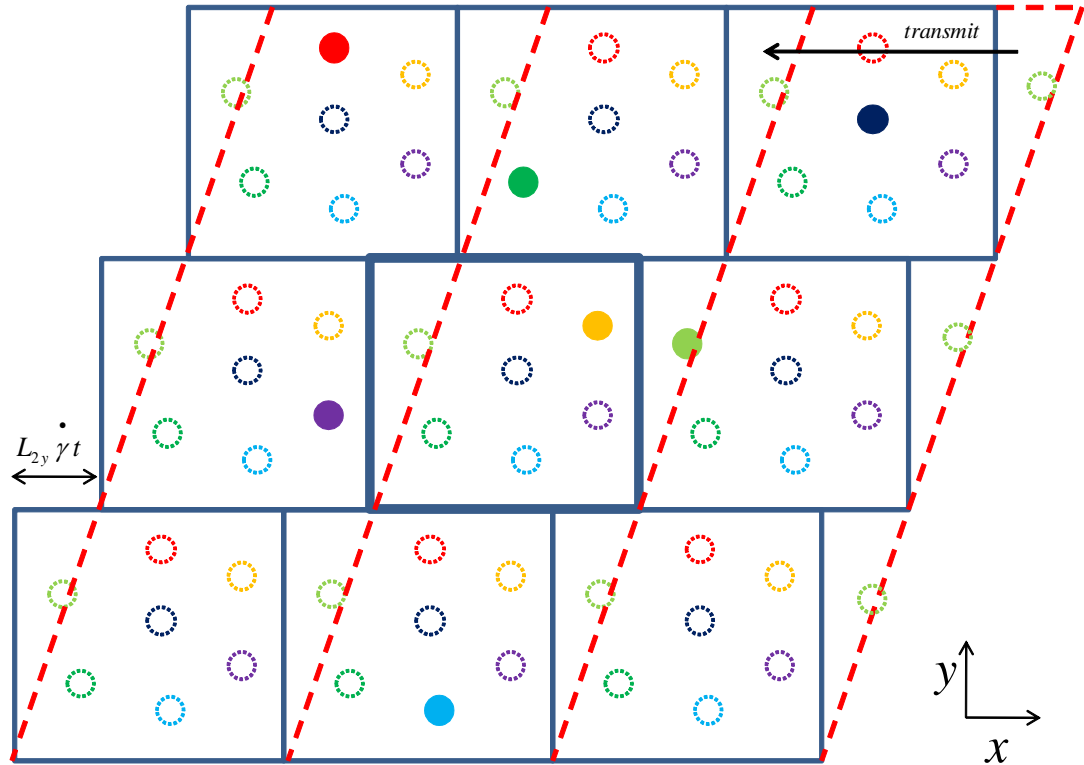


FIGURE 3.2: Lagrangian-Rhomboid and Sliding-Brick periodic boundary conditions.

From Eq.(3.8), we can get

$$\begin{aligned} dL_{kx}(t) &= L_{ky}(t)\dot{\gamma}dt \\ dL_{ky}(t) &= 0 \\ dL_{kz}(t) &= 0 \end{aligned} \quad (3.9)$$

Eq.(3.9) implies that the box vectors in y and z -directions are not changed during the shear. However, for a simulation of length t the vector of the simulation box in x -direction grows linearly in time as

$$L_{kx}(t) = L_{ky}\dot{\gamma}t + L_{kx}(0) \quad (3.10)$$

If atoms move through the top/bottom faces of the box, they are returned to the bottom/top faces with displacement $\mp L_{2y}\dot{\gamma}t$ in the x -direction, where t is the shear time. As $\theta(t)$ is the angle between \mathbf{L}_1 and \mathbf{L}_2 , then $\theta(t) = \arctan(1/\dot{\gamma}t)$,

which creates a problem. If $t \rightarrow \infty$, then $\theta(t) \rightarrow 0$ and $|\mathbf{L}_2| \rightarrow \infty$, which is not practical. Two equivalent algorithms were introduced to fix this situation. The first of these is to deform the simulation box until it reaches a preset angle θ_p , at which time the box is changed back to the original cubic shape. In this method, the transformations do not happen very frequently and box sides lengths do not get too large. The second method is to use Lees-Edwards “sliding-brick” periodic boundary condition. As discussed above, image boxes above and below the original simulation box are displaced relative to it by $\mp L_{2y} \dot{\gamma} t$. Both methods are illustrated in Fig.3.2. The red boxes are the deformed boxes in the first method, which is also called Lagrangian-Rhomboid periodic boundary conditions. The blue boxes are the Sliding-Brick periodic boundary conditions. Sliding-Brick boundaries are constructed from Lagrangian-Rhomboid boundaries by transmitting the triangular region to create cubes. The relative distances between all particles remain the same in both systems and hence all physical properties are equivalent in both systems. The Sliding-Brick boundary conditions are used in our simulations.

3.2.2 Thermostat methods

In molecular dynamics simulations, small system undergoing large fluctuations can lead to much larger fluctuations in kinetic energy than appropriate for a given temperature. In the microcanonical ensemble(NVE), the system will have a drift in a long run due to computing error. The systems are more easier to simulate in canonical ensemble, which means the number of particles, the volume and the temperature of the system are conserved. In this ensemble, the energy is exchanged with a thermostat.

A variety of thermostat methods is available to add and remove energy from the system, approximating the canonical ensemble. Popular techniques to control temperature include velocity rescaling(constraint method), the Nosé-Hoover thermostat, the Berendsen thermostat and Langevin dynamics. Now we are going to introduce these methods.

3.2.2.1 Andersen method

Andersen method mimics random collisions with an imaginary heat bath particles. At intervals, the velocity of a randomly selected molecule is chosen afresh from the Maxwell-Boltzmann distribution[56]. Time intervals between collisions with the bath are chosen from Poisson distribution, with a specified mean collision time. If the collisions take place infrequently, energy fluctuations will occur slowly, but kinetic energy fluctuation will occur much as in conventional MD. If the collisions occur very frequently, kinetic energy fluctuations are dominated by collisions rather than by the systematic dynamics. The choice of this interval is an important parameter. The disadvantage of Andersen method is that it will change the dynamics of the system drastically.

3.2.2.2 Constraint method

A simple method of fixing the temperature of a system is to rescale the velocity of each molecule at each time step by a factor of $(T/\mathcal{T}_C)^{1/2}$ where \mathcal{T}_C is the current temperature and T is the desired thermodynamic temperature. Velocity rescaling is a crude method of solving a set of equations of motion that differ from the Newtonian's. The modified equation of motion is

$$\dot{\mathbf{r}}(t + \delta t) = \sqrt{\frac{T}{\mathcal{T}_C}} \left(\dot{\mathbf{r}}(t) + \frac{\mathbf{f}(t)}{m} \delta t \right) \quad (3.11)$$

A disadvantage of constraint method is that it leads to discontinuities in the momentum part of the phase space trajectory due to the rescaling procedure at each time step. And it does not allow temperature fluctuations which are present in the canonical ensemble.

3.2.2.3 Nosé-Hoover thermostat

At each time-step, the velocities of all particles are rescaled by an additional dynamic variable ξ

$$\dot{\mathbf{r}}(t + \delta t) = \xi \left(\dot{\mathbf{r}}(t) + \frac{\mathbf{f}(t)}{m} \delta t \right) \quad (3.12)$$

$$\dot{\xi} = C(T - \mathcal{T}_C) \quad (3.13)$$

where C is a constant parameter that can be set for optimal results. This method modifies the velocities “gently”.

3.2.2.4 Berendsen thermostat

Comparing to the constraint method, Berendsen thermostat is trying to correct the deviations of the actual temperature \mathcal{T}_C from the prescribed one T by multiplying the velocities by a certain factor in order to move the system dynamics towards the one corresponding to T . At each time step, the velocities of each particle is rescaled so as to bring \mathcal{T}_C closer to T .

$$\dot{\mathbf{r}}(t + \delta t) = \sqrt{1 + \frac{\delta t}{\tau_B} \left(\frac{T}{\mathcal{T}_C} - 1 \right)} \left(\dot{\mathbf{r}}(t) + \frac{\mathbf{f}(t)}{m} \delta t \right) \quad (3.14)$$

where τ_B is a timescale for coupling to the thermal bath.

3.2.2.5 Dissipative particle dynamics (DPD) method

DPD was originally developed in order to simulate fluids on a mesoscopic scale with correct hydrodynamic interactions. However, DPD can also be viewed as a thermostat to molecular dynamics. The DPD algorithm is similar to Stochastic dynamics (section 1.9.3) in that there is local friction and noise such that the stabilizing features are retained. We can run the DPD-thermostat system with the same time step as Stochastic Dynamics. However, the friction does not depend

on the absolute velocities but rather on the relative velocities with respect to surrounding particles. And the stochastic forces act on pairs of nearby particles.

The DPD equations of motion are given by

$$\begin{aligned}\dot{\mathbf{r}}_i &= \frac{\dot{\mathbf{p}}_i}{m_i} \\ \dot{\mathbf{p}}_i &= \mathbf{f}_i + \mathbf{f}_i^D + \mathbf{f}_i^R\end{aligned}\quad (3.15)$$

where i is the particle index, \mathbf{f}_i^D is the friction force on particle i , and \mathbf{f}_i^R is the corresponding random force. These two forces are both based on particle pairs,

$$\begin{aligned}\mathbf{f}_i^D &= \sum_{j \neq i} \mathbf{f}_{ij}^D \\ \mathbf{f}_i^R &= \sum_{j \neq i} \mathbf{f}_{ij}^R\end{aligned}\quad (3.16)$$

The dissipative force between particle i and j is given by

$$\mathbf{f}_{ij}^D = -\xi w^D(|\mathbf{r}_{ij}|)(\hat{\mathbf{r}}_{ij} \cdot \mathbf{v}_{ij})\hat{\mathbf{r}}_{ij}\quad (3.17)$$

and the random force by

$$\mathbf{f}_{ij}^R = \lambda w^R(|\mathbf{r}_{ij}|)\theta_{ij}\hat{\mathbf{r}}_{ij}\quad (3.18)$$

where $\mathbf{v}_{ij} = \mathbf{v}_i - \mathbf{v}_j$ is the relative velocity between particles i and j , $\hat{\mathbf{r}}_{ij}$ denotes the unit vector of the interatomic vector $\mathbf{r}_{ij} = \mathbf{r}_i - \mathbf{r}_j$, ξ is the friction coefficient and λ is the random force amplitude. w^D and w^R are r -dependent weight functions vanishing for $r \geq r_c$. θ_{ij} is a Gaussian white noise variable with $\theta_{ij} = \theta_{ji}$ and first and second moments

$$\langle \theta_{ij}(t) \rangle = 0\quad (3.19)$$

$$\langle \theta_{ij}(t)\theta_{kl}(t') \rangle = (\delta_{ik}\delta_{jl} + \delta_{il}\delta_{jk})\delta(t - t')\quad (3.20)$$

The angular momentum is conserved as \mathbf{F}_{ij}^D and \mathbf{F}_{ij}^R act along \mathbf{r}_{ij} . There is an independent random process for each pair of particles. In order to satisfy the

fluctuation-dissipation theorem, the relations

$$\lambda^2 = 2k_B T \xi \quad (3.21)$$

and

$$w^R(|\mathbf{r}|) = \sqrt{w^D(|\mathbf{r}|)} \quad (3.22)$$

must hold[57]. The usual choice is

$$w^R(r) = \sqrt{w^D(r)} = \begin{cases} 1 - r/r_c; & r < r_c \\ 0; & r \geq r_c \end{cases} \quad (3.23)$$

Another choice, which is computationally more efficient, is

$$w^R(r) = w^D(r) = \begin{cases} 1; & r < r_c \\ 0; & r \geq r_c \end{cases} \quad (3.24)$$

We use Eq.(3.23) in most of our simulations except when a large shear rate $\dot{\gamma} > 0.1\tau^{-1}$ was applied on the system, in which case Eq.(3.24) was used.

3.2.3 Steady-state properties from the test run

In this section, we will show some steady-state properties of the system under shear, in particular velocity and temperature profiles. All equations of motion in this section are Langevin dynamics but not with DPD thermostat. First, we run the simulations with different chain lengths but fixed number of particles in the system under the same shear rate. The velocity used in the friction term is the real velocity of each particle. The velocity profiles are shown in Fig.3.3. The velocity profile of the dumbbell($N = 2$) is in good agreement with the desired linear velocity profile, but if we increases the chain length, it starts to deviate from the desired one. The reason of this phenomenon is probably that the longer the chain length is, the more difficult for the momentum to be transmitted from the boundary to the center of the box. We also observe that the longer the chain

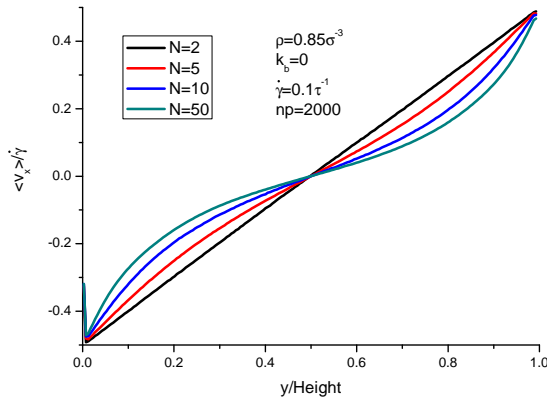


FIGURE 3.3: Velocity profile of different chain lengths. np is the number of the particles in the system.

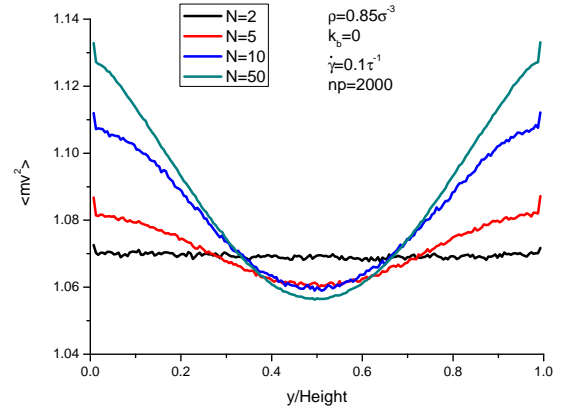


FIGURE 3.4: Temperature profile of different chain lengths.

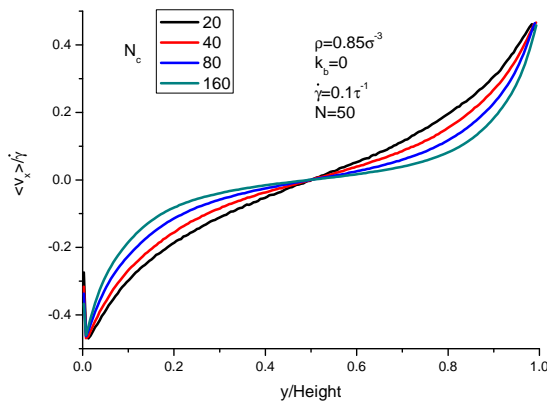


FIGURE 3.5: Velocity profile of different number of chains.

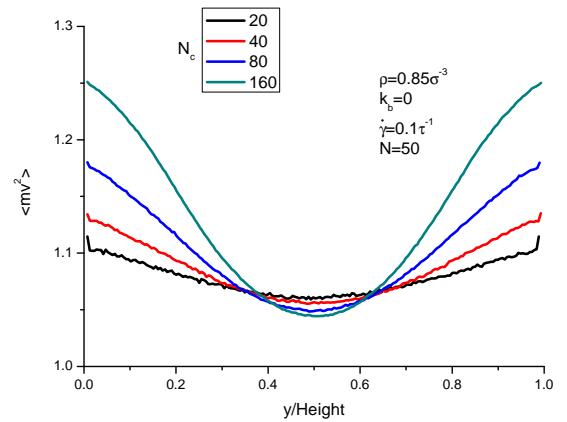


FIGURE 3.6: Temperature profile of different number of chains.

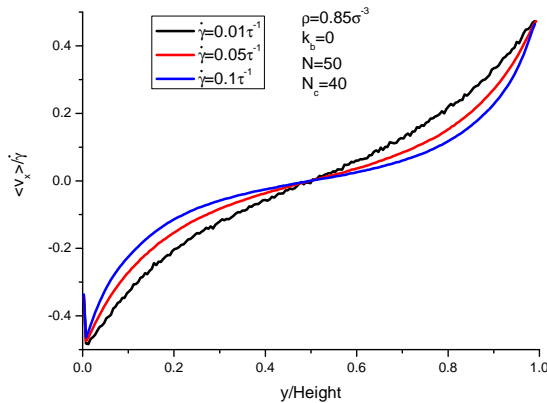


FIGURE 3.7: Velocity profile of different shear rate.

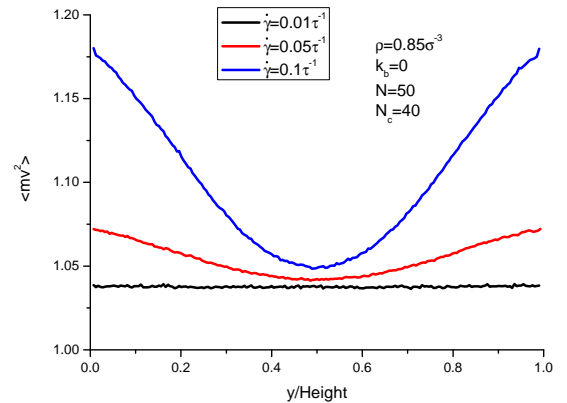


FIGURE 3.8: Temperature profile of different shear rate.

length is, the slower the particle is than it should be, which means the friction term is overestimated. The temperature profiles are shown in Fig.3.4. The temperature near the boundaries is higher than the one in the center, which can be explained by the shear heating as the momentum exchanged around the boundaries.

We also run simulations with the same chain lengths and shear rates but with

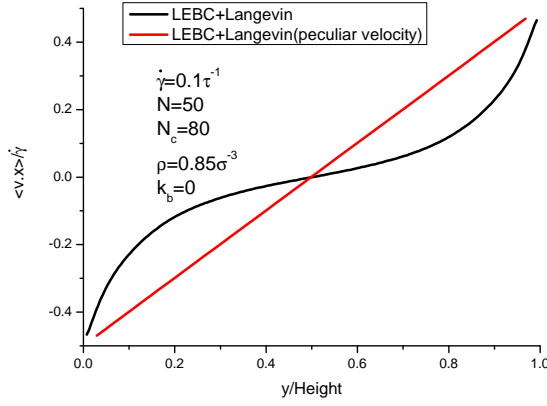


FIGURE 3.9: Velocity profile of different inertial terms.

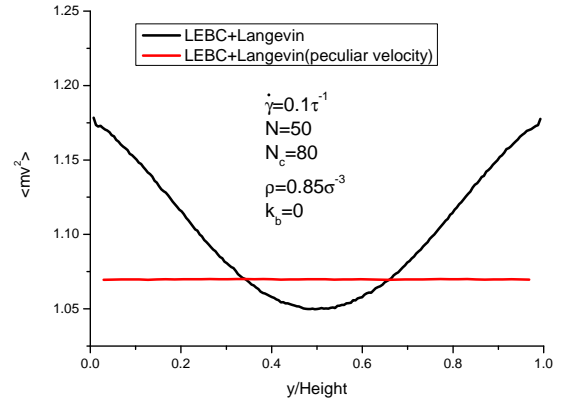


FIGURE 3.10: Temperature profile of different inertial terms.

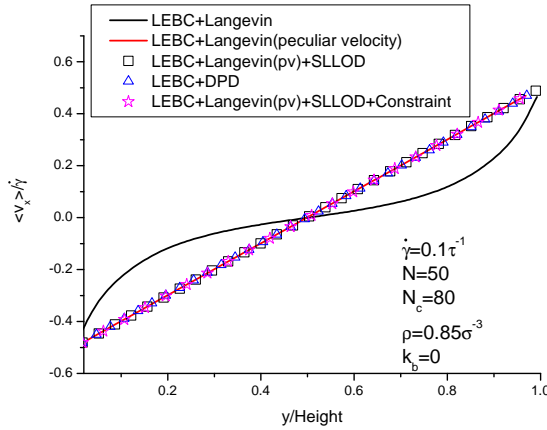


FIGURE 3.11: Velocity profile of different equations of motion.

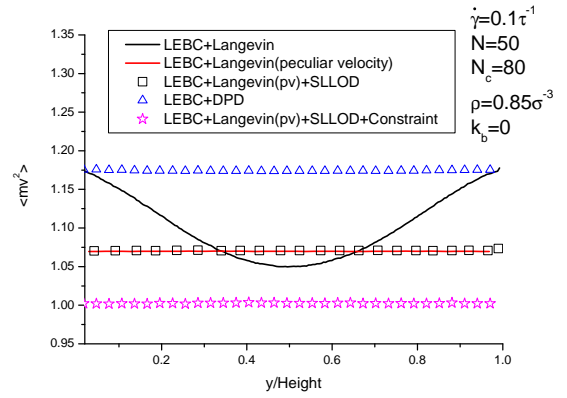


FIGURE 3.12: Temperature profile of different equations of motion.

different system sizes. The larger the system is, the more difficult for the momentum to be transmitted from the boundary to the center of the box (Fig. 3.5 and 3.6). Same quantities are measured in the systems at different shear rates (Fig. 3.7 and 3.8). The velocity profile is closer to the desired linear one if the shear rate is smaller.

Figs. 3.3-3.8 show that both measurements depend on the system size, shear rate, chain length, etc, which should not be the case. To fix these problems, we introduce peculiar velocity in the inertial term, which makes sense that the friction should depend on the relative velocity between the particle and the background but not on the real velocity. Now the velocity profile is in good agreement with the desired ones (Fig. 3.9 and 3.10). However, the temperature is still higher than the target $T = 1$.

We applied SLLOD equation of motion to our model and observed the same

results as in the previous case (square symbol in Fig.3.11 and 3.12). Constraint thermostat method is used to keep the temperature to the desired one (star symbols in Figs.3.11 and 3.12). All the results discussed later are obtained from this combination of Langevin, SLLOD and constraint thermostat method.

As we know, polymer chains will be stretched and oriented under shear, the size of the long chains will be larger than the length of the simulation box and the chains will interact with themselves through the periodic boundaries. In order to eliminate this defect, we need to use non-cubic simulation box. Suppose the shear direction is along the x -axis, the direction of velocity gradient is along the y -axis. The first method we used is putting all chains into a reshaped box which has the length ratio on x, y, z equal to $2 : 1 : 1$. The simulations run for a long time around several terminal relaxation time τ_d of the longest component to make sure the system is in equilibrium, and then we start to shear the material. The second method we used is that the configuration of the chains is obtained from the previous simulations in equilibrium which has a cubic simulation box. Another copy of this configuration is made. And we put this copy next to the original one along the x -axis to make the simulation box with the aspect ratio of $2 : 1 : 1$. As the two parts of the box contain exactly the same conformations, we run the simulations for one terminal relaxation time τ_d of the longest component to let chains forget about the initial configuration. The second method can save the simulation times for equilibration significantly. Now we would like to show the difference among these methods. Stress tensor components σ_{xy} and two normal stress difference $\sigma_{xx}-\sigma_{yy}$, $\sigma_{zz}-\sigma_{yy}$ are shown in Fig.3.13. The black lines are derived from the cubic simulation box. The red and blue lines are from the methods one and two, respectively. We can see that the first normal stress $\sigma_{xx}-\sigma_{yy}$ in the cubic box does deviate from that obtained from the other two methods. All the results from shear are obtained by using the configuration copy method.

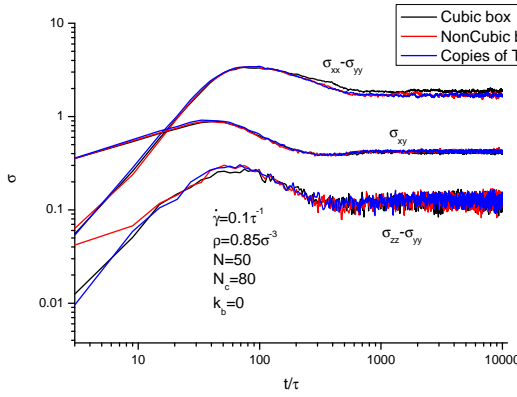


FIGURE 3.13: σ_{xy} and two normal stress in different simulation boxes.

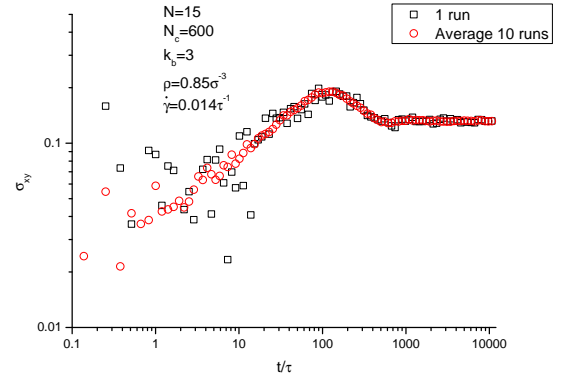


FIGURE 3.14: σ_{xy} in one single run and averaged over ten jobs.

3.2.4 Averaging methods

As we know the number of particles involved in the MD simulations is ranging from several hundred to several hundred thousand, which is a small number comparing to the number of molecules used in experiments. So a careful averaging method is essential in the simulations. Logarithmic bins in time are introduced. Suppose a quantity $C(t)$ of the system is measured at time t since the start of shear. A series of averaging time intervals $t'_i, i \in \mathbb{Z}^+$ where \mathbb{Z}^+ is the set of non-negative integer numbers, is introduced as following:

$$t'_0 = D \quad (3.25)$$

$$t'_i = D M^i \quad (3.26)$$

where D is a constant standing for the first time interval, and M is a multiplication factor. In our simulations, D and M are set to $8dt$ and 1.1 respectively, where dt is the simulation time step. Suppose the shear starts from t_0 , $t_i = t_0 + \sum_{k=0}^{i-1} t'_k$, then

$$C(t_i + \frac{t'_i}{2}) = \frac{1}{t'_i} \int_{t_i}^{t_i+t'_i} C(t) dt \quad (3.27)$$

With this algorithm we obtain around 25 data points in each decade of time (black symbols in Fig. 3.14). As the system size is quite small (9000 particles), the signal is not very good in just one single run. We run 10 simulations with the same parameters except the seed of random force generator, and then average over all these data (red symbols in Fig. 3.14). The curve is much smoother and more reliable

than the data from the single run. However, the signal is still noisy at short times as the averaging intervals t'_i at short times are much smaller comparing to the ones at longer times. Note however that the early time behaviour can be obtained from the $G(t)$ data as demonstrated later, so these data are not essential.

3.3 Monodisperse melts under shear

In this section we will investigate both static and dynamic properties of the material in entangled systems. As discussed before, the entanglement lengths N_e in flexible and semi-flexible systems are around 50 and 15 respectively. If the same number of entanglements is required, the chain lengths in flexible systems is more than three times larger than the one in semi-flexible systems, which makes the simulation times much longer in the former case. So we only concentrate on semi-flexible chains at this stage.

3.3.1 Simulation results

We first show the transient shear viscosity η as a function of time t at different shear rates $\dot{\gamma}$ for different chain lengths in Fig.3.15 and Fig.3.16. The dashed line is obtained from the stress relaxation function $G(t)$ in the linear viscoelastic regime:

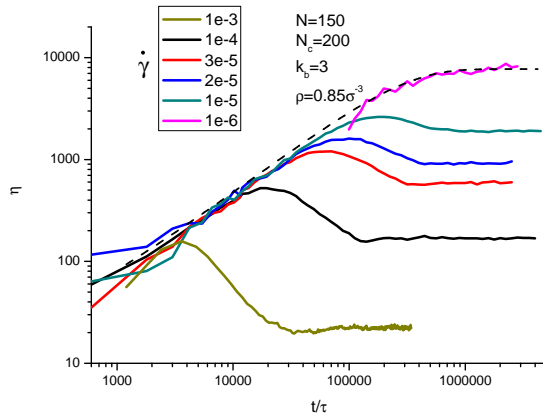
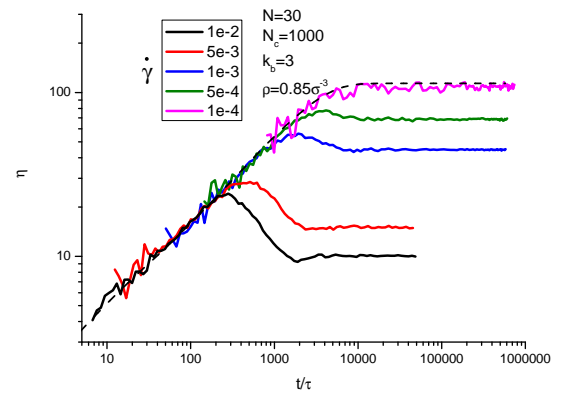
$$\eta(t) = \int_0^t G(t') dt' \quad (3.28)$$

We will use this curve as an additional validation of our procedure. At small strains the respective shear viscosity curves superpose for all applied shear rates with the linear viscoelastic curve. If the shear rate $\dot{\gamma}$ is faster than the reciprocal of the terminal time τ_d of the system, the viscosity $\eta(t)$ passes through a maximum and then decreases until it reaches the steady-state. The terminal time τ_d of the monodisperse melts with chain length $N = 150$ and $N = 30$ with bending energy $k_b = 3$ are around $2.58 \times 10^5 \tau$ and $2.5 \times 10^3 \tau$ respectively, where τ is the Lennard-Jones time unit. However, there is no clear “yielding point” of the viscosity at

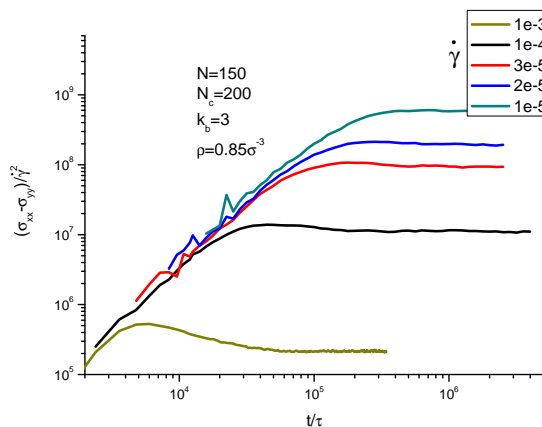
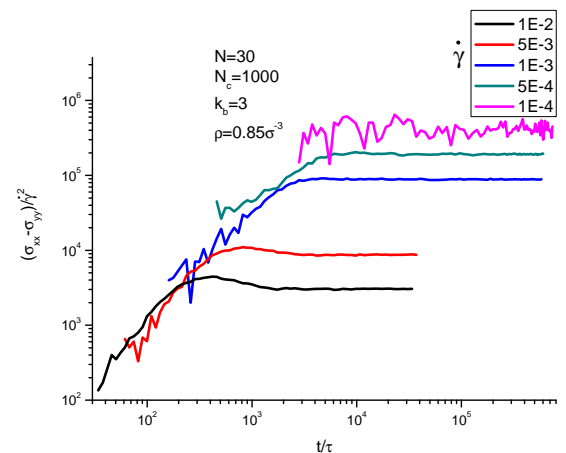
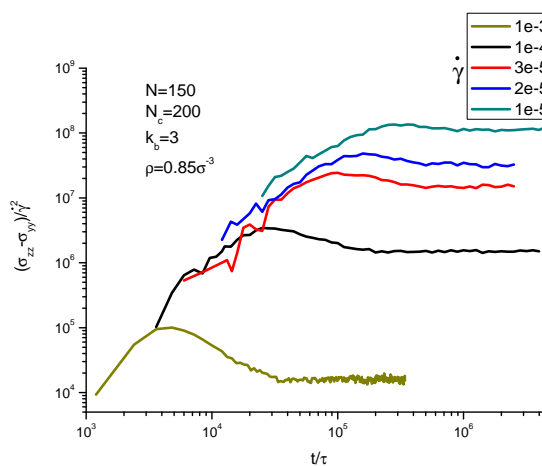
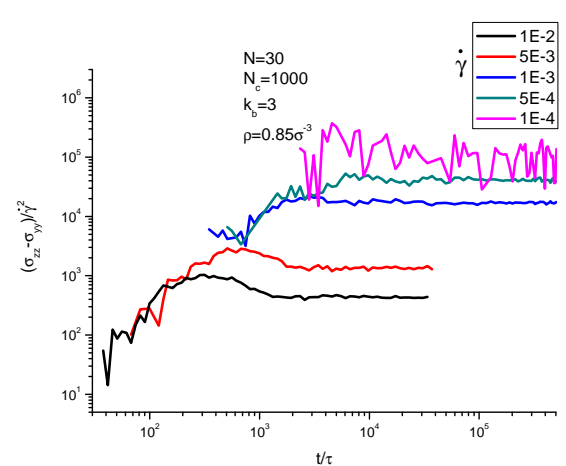
the shear rate $\dot{\gamma}$ slower than the reciprocal of the terminal time τ_d . The stress maximum can be taken as the steady-state stress in these cases and its value increases linearly with the shear rates. The viscosity has a smooth transition from the transient-state to the steady-state (pink line in Fig. 3.15 and Fig. 3.16). It is in good agreement with the result from the stress relaxation function $G(t)$ in linear viscoelastic regime (dashed line in Fig. 3.15 and Fig. 3.16). At the higher shear rate, which is faster than the reciprocal of the terminal time τ_e of an entangled strain, an undershoot can be observed before the system reaches the steady-state.

As we discussed in Chapter 1, the average of the diagonal elements of the stress tensor is the pressure of the system, which is constant in steady-state. Because the system is only sheared in x -axis, the symmetry in respect to the z -axis is still conserved. Thus, the whole stress tensor has only three degree of freedom, which are σ_{xy} , $\sigma_{xx} - \sigma_{yy}$ and $\sigma_{zz} - \sigma_{yy}$. The last two stress differences are called the first and the second normal stress. First and second normal stresses divided by the square of the shear rate $\dot{\gamma}$ are plotted in Fig. 3.17-3.20. Again at small strains all the curves collapse onto a master curve. At a shear rate $\dot{\gamma}$ faster than the reciprocal of the terminal time τ_d , we can also observe an overshoot in the second normal stress. The overshoot in the first normal stress appears at higher rates, presumably larger than τ_R^{-1} .

It is interesting to analyze the position and the magnitude of the stress maximum for different chain lengths and shear rates. For monodisperse melts, the Doi-Edwards model predicts that the shear-stress maximum should occur at a shear strain $\gamma_{max} = \dot{\gamma}t_{max}$ of about 2, independently of the shear rate $\dot{\gamma}$. For small shear rates, the experimental maximum is indeed around 2, but it shifts to higher strain values for large shear rates [58]. We observed similar behaviour in our simulations (black square symbols in Fig. 3.22). In the system with chain length $N=30$, the shear strain at maximal stress is around 2 for all shear rates. However, the shear strain at maximal stress is around 3.5 if $\dot{\gamma}\tau_d = 300$ for the system with chain length $N=150$, which was also observed in experiments. The maximal stress σ_{max} as a function of shear rates are plotted in Fig. 3.21. The power-law exponents

FIGURE 3.15: Viscosity η in different shear rate $\dot{\gamma}$ for $N=150$.FIGURE 3.16: Viscosity η in different shear rate $\dot{\gamma}$ for $N=30$.

are approximately 0.3 and 0.9 in the systems with chain length $N=150$ and $N=7$ respectively.

FIGURE 3.17: First normal stress $\sigma_{xx}-\sigma_{yy}$ in different shear rate for $N=150$.FIGURE 3.18: First normal stress $\sigma_{xx}-\sigma_{yy}$ in different shear rate for $N=30$.FIGURE 3.19: Second normal stress $\sigma_{zz}-\sigma_{yy}$ in different shear rate for $N=150$.FIGURE 3.20: Second normal stress $\sigma_{zz}-\sigma_{yy}$ in different shear rate for $N=30$.

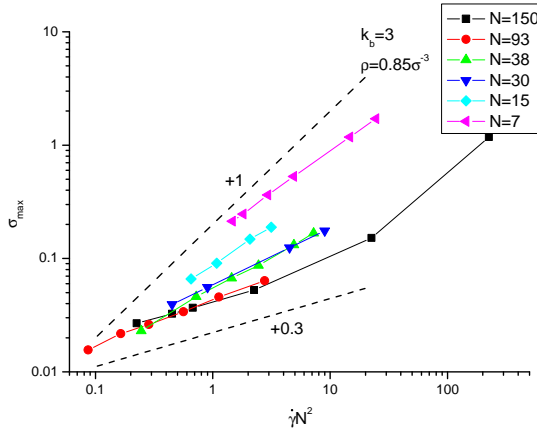


FIGURE 3.21: Shear-stress maximum as a function of $\dot{\gamma}N^2$.

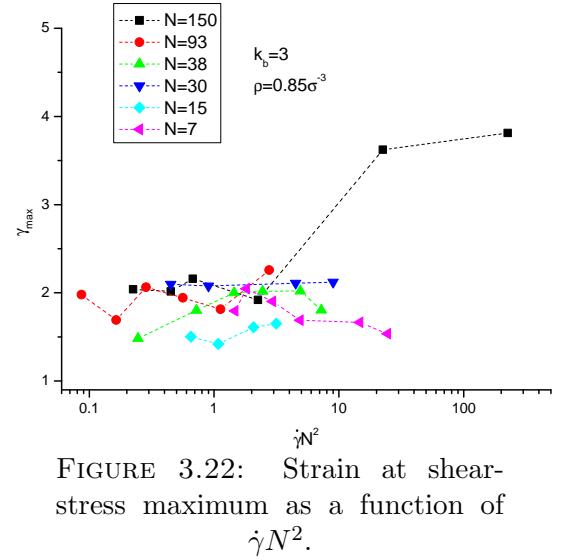


FIGURE 3.22: Strain at shear-stress maximum as a function of $\dot{\gamma}N^2$.

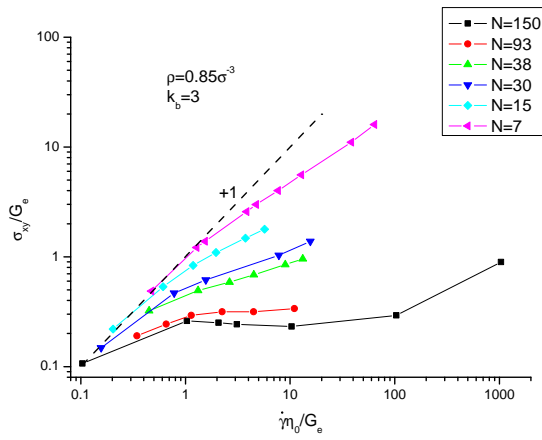


FIGURE 3.23: Shear stress σ_{xy} in steady-state as a function of $\dot{\gamma}\eta_0/G_e$, where $G_e=0.073$.

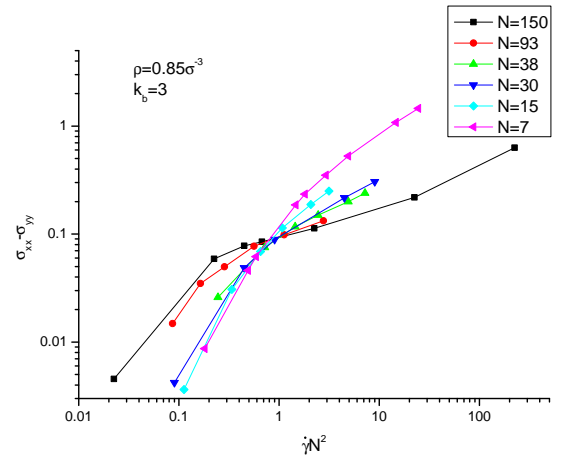


FIGURE 3.24: First normal stress as a function of $\dot{\gamma}N^2$.

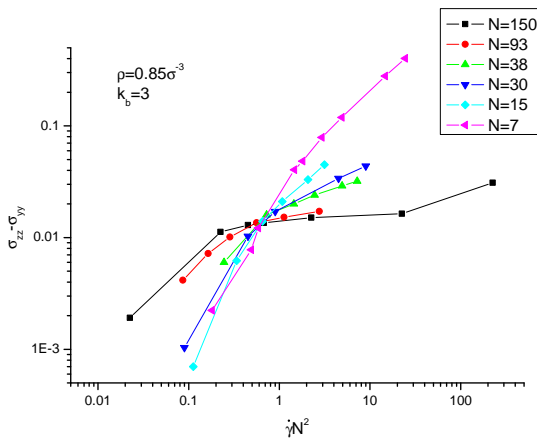


FIGURE 3.25: Second normal stress as a function of $\dot{\gamma}N^2$.

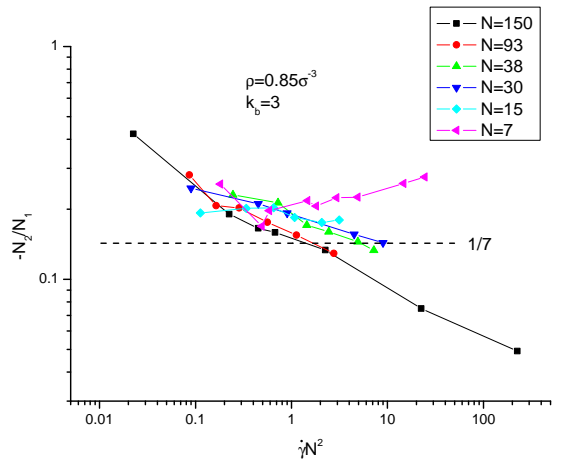


FIGURE 3.26: Ratio of first and second normal stresses as a function of $\dot{\gamma}N^2$.

The shear stress σ_{xy} , first and second normal stresses and the ratio of these two normal stresses in the steady state are shown as a function of shear rate $\dot{\gamma}$ in

Fig.3.23-Fig.3.26. The first and second normal stresses increase as the shear rate increases in all systems. Surprisingly if the first and second normal stresses are plotted as a function of $\dot{\gamma}N^2$, all curves pass through a particular point. The ratio of the second and the first normal stresses is about 1/7 at small molecular weight, which is in good agreement with the Doi-Edwards theory and the experimental results from Schweizer *et al.*[59][42]. With increasing the chain length, a negative slope comes out. More interesting parts are the behaviours of the steady-state shear stresses. An ideal unentangled Rouse chain shows no shear thinning and therefore it can be represented by the line $\sigma = \eta\dot{\gamma}$ at all shear rates(dashed line in Fig.3.23). In a slightly entangled system($N=30$), the steady-state shear stress increases with the slope smaller than 1 with increasing shear rate. However, in our most entangled system for $N=150(Z=10)$ it increases first, passes through a maximum around $\dot{\gamma}\tau_d = 2$ and then decreases by about 5% until $\dot{\gamma}\tau_d = 200$ and then increases again(black squares in Fig.3.23). The shear stress σ_{xy} as function of simulation time of chain length $N=150$ at different shear rates is shown in Fig.3.27. Theoretically, non-monotonic steady state stress means that the system must show shear banding if we relax the condition of linear velocity profile.

3.3.2 Cox-Merz rule

Cox-Merz rule states that the steady state shear viscosity at a given shear rate is equal to the dynamic viscosity at the same frequency

$$\eta(\dot{\gamma}) = \eta^*(\omega) \quad \text{at } \dot{\gamma} = \omega \quad (3.29)$$

where

$$\eta^*(\omega) = \frac{\sqrt{G'(\omega)^2 + G''(\omega)^2}}{\omega} \quad (3.30)$$

This rule is more or less empirical - it works for many common polymers but there is no theoretical background that it should work for all polymers and it certainly does not. Cox-Merz rule was checked in our simulations(Fig.3.28). They show

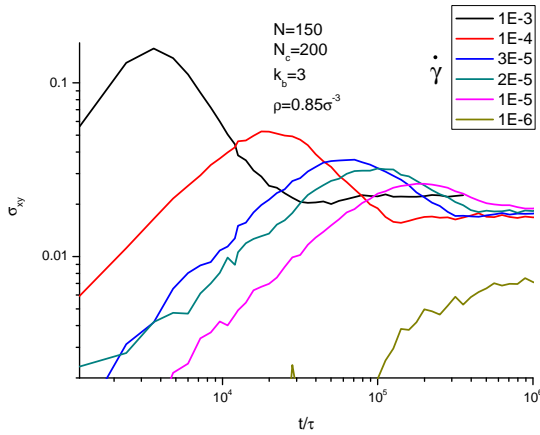


FIGURE 3.27: $\sigma_{xy}(t)$ of semi-flexible chain with $N=150$ at different shear rates $\dot{\gamma}$.

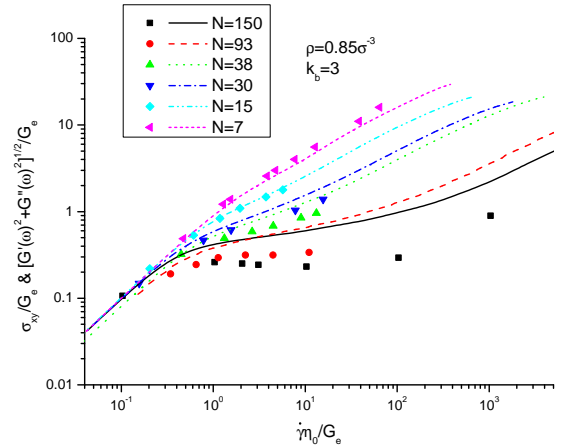


FIGURE 3.28: Cox-Merz rule in our simulations. Solid symbols are stress at steady state. Lines are complex viscosity times shear rate $\dot{\gamma}$.

that the Cox-Merz rule works for the short chain systems, but not for the longer chains.

3.3.3 Stress-optical law in monodisperse melts

Before doing other analysis, let us check if the stress optical law works in our shear simulations. Chain lengths $N = 30, 150$ are chosen for the monodisperse melt. First, the stress and orientation relaxation functions in the equilibrium state are shown in Fig.3.29. The stress-optical law works for the time scale larger than 500τ . Now we would like to see whether the stress-optical law works in the shear situation. The stress and the orientation of the systems divided by the shear rates are shown in Fig.3.30. In the transient state, both stress and orientation collapse onto their respective master curves. The power law exponent of stress is around 0.5. However, the power law exponent of orientation is around 0.8. It looks like the stress-optical rule does not work at short times. As we know, the viscosity in shear can be expressed by the integral of the stress relaxation function $G(t)$ in equilibrium (Eq.3.28). The orientation in shear can also be expressed by the integral of the orientation relaxation function in equilibrium. As shown in Fig.3.29 stress and orientation behave differently at short times. There are oscillations in the stress relaxation function due to bond fluctuations, and it is almost constant

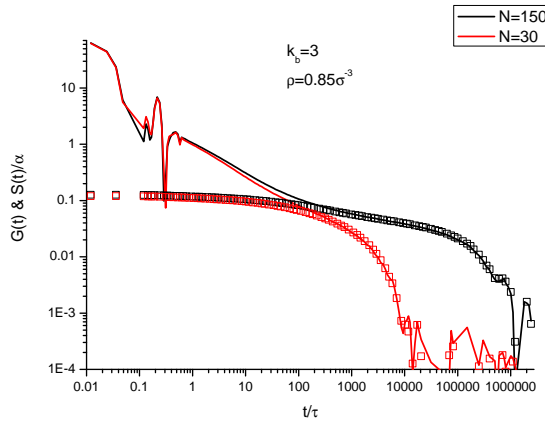


FIGURE 3.29: Stress and orientation relaxation functions in the equilibrium where α called stress-optical coefficient is 1.28.

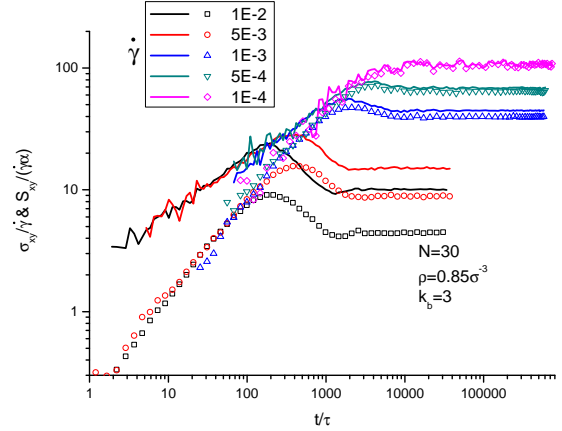


FIGURE 3.30: Stress σ_{xy} (lines) and orientation S_{xy} (symbols) as a function of time at different shear rates, where $\alpha = 1.28$ is the stress-optical coefficient from the equilibrium simulation.

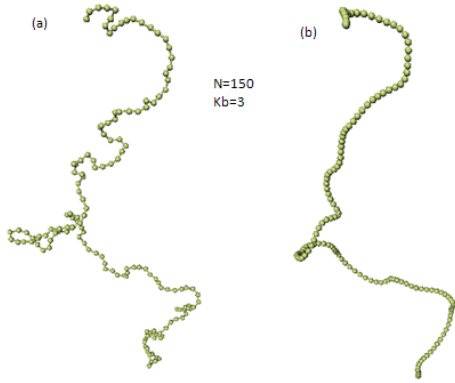


FIGURE 3.31: Instantaneous position(a) and mean path(b) of a polymer chain with chain length equal to 150 and bending energy equal to 3.

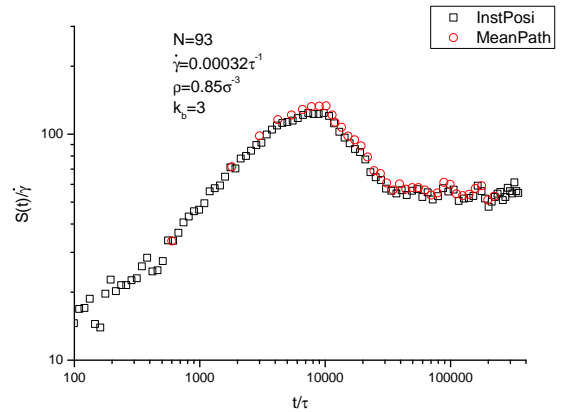


FIGURE 3.32: Orientation from instantaneous positions is compared to the one obtained from mean path.

for orientation relaxation function, which explains why the slope of orientation in shear is closer to 1. After the overshoot, the stress and the orientation are in qualitative agreement(Fig.3.30). In conclusion, the stress-optical law works quite well at small shear rates $\dot{\gamma} < 1/500$ and at long time $t > 500$.

3.3.4 Orientation from mean path

We introduce a notion of the *mean path* which is a collection of the bead coordinates \mathbf{r}_i averaged over the time interval τ_{av}

$$\hat{\mathbf{r}}_i(t) = \frac{1}{\tau_{av}} \int_{t-\tau_{av}}^t \mathbf{r}_i(t') dt' \quad (3.31)$$

Both instantaneous configuration and the mean path of a polymer chain with chain length $N=150$ are shown in Fig.3.31. These configurations show that the mean paths are smoother than the chains and the short time fast fluctuations are suppressed by the averaging procedure. The averaging time interval should be chosen with care. In Fig.3.31, the averaging time was chosen to be $\tau_{av}=1200\tau$. Now we would like to check whether the mean path will keep the property of the orientation of the original chains or not. The orientation obtained from the instantaneous positions and the mean paths are both shown in Fig.3.32. The monodisperse melt with chain length $N=93$ and bending energy $k_b=3$ was chosen. The result from the mean paths is in good agreement with the one from the instantaneous positions, so we can claim that mean paths contains all information about the orientation of the polymer chains. In the future, we will analyse our system by using mean path instead of instantaneous positions, which can erase faster fluctuation effects. We note that orient function $S(t)$ obtained from instantaneous positions stored every 1200τ is much noisier than the one shown in Fig.3.32.

3.3.5 Configuration of polymer chain in transient state and steady state

DNA tumbling has previously been observed in dilute unentangled solutions[60] and in entangled solutions[61]. We would like to investigate the tumbling in polymer melts for the first time in our simulations.

In Fig.3.33, we can see the evolution of the single chain conformation in a monodisperse melt. The sample has the chain length $N=93$ with bending energy

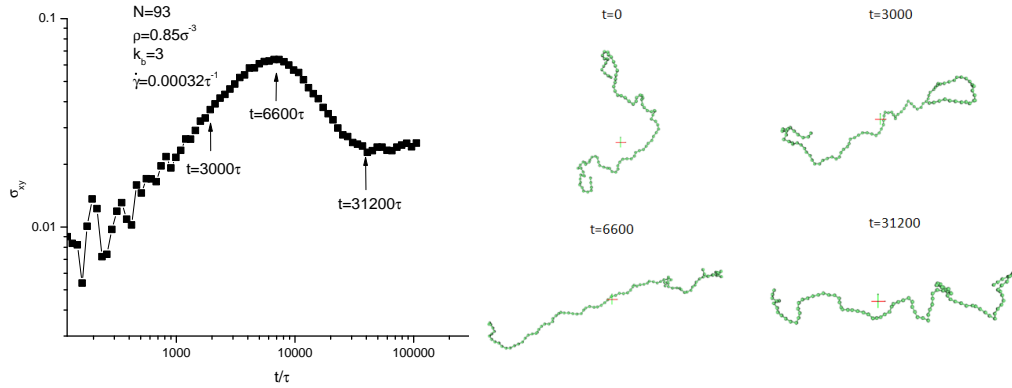


FIGURE 3.33: Configuration of the polymer chain at different state during shear.

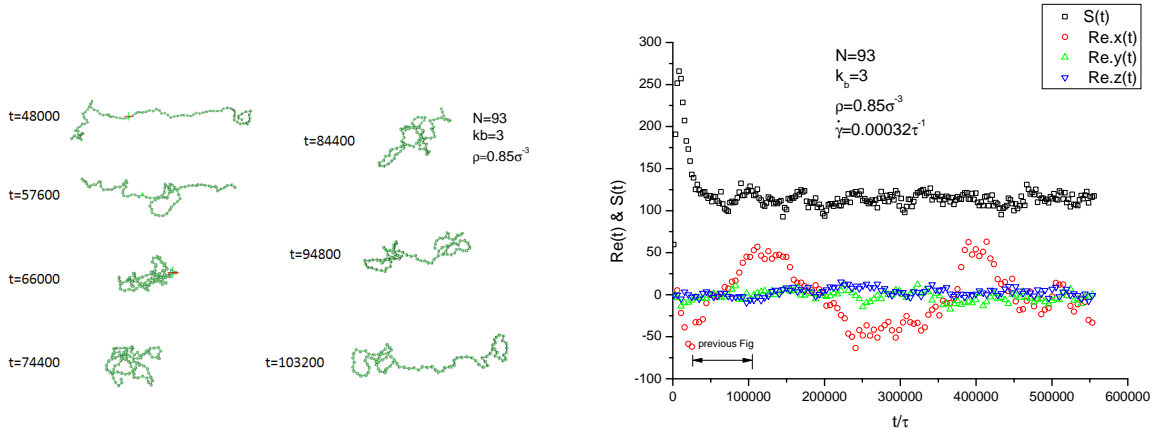


FIGURE 3.34: The corresponding conformation of the chain during tumbling in steady state at shear rate $\dot{\gamma} = 0.00032\tau^{-1}$.

FIGURE 3.35: End-to-end vector \mathbf{R}_e of one chain and orientation of the system in shear.

$k_b = 3$ and density $\rho = 0.85\sigma^{-3}$. Before the shear starts ($t = 0\tau$), the chain is a random walk in 3D-space. After shearing starts, the chain is stretched in shear direction (x -axis).

Beyond the stress overshoot, we observed that the chain also spends a small fraction of the time to tumble as shown in Fig.3.34. In Fig.3.35, we show each component of the end-to-end vector \mathbf{R}_e of the chain which was plotted in Fig.3.34. The black symbols are the orientation of the system. y and z components of \mathbf{R}_e are not strongly affected by the shear. They both fluctuate around the average of the end-to-end vector in equilibrium. However, x -component of \mathbf{R}_e is tumbling around the average. The configuration of the chain in Fig.3.34 is the one during the first tumbling after the overshoot. The observed tumbling means that decoupling approximations used by the tube theory[62] might not work for these shear

rates. In future we plan to investigate these approximations using our mean path trajectories.

3.3.6 Comparing semi-flexible chain with the experiments

Experiments(-35°C)						Simulations					
sample	M_w [kg/mol]	Z [-]	η_0 [Pa s]	τ_d [s]	τ_R [s]	kb	N	Z	η_0 [$\varepsilon\tau\sigma^{-3}$]	τ_d [τ]	τ_R
PI-2k	2.4	0.5	73	0.0012	0.0047	3	7	0.5	9.4	84	150
						0	20		15	550	-
PI-4k	5.1	1.1	1.9E4	0.033	0.045	3	15	1.1	30	490	670
						0	40		34	930	-
PI-14k	13.5	2.8	3.3E5	0.56	0.48	3	38	2.8	190	3700	4300
						0					-
PI-30k	33.6	7.0	1E7	17.2	3.5	3	93	7.0	2500	9.1E4	2.6E4
						0					-

TABLE 3.1: Mapping between the experiments and the simulations.

Now we investigate whether we can map our simulation results onto the real experiments. The experimental sample is polyisoprene(PI) from Auhl *et al.*[63] with a large range of molecular weights(2kg/mol-1000kg/mol) and narrow molecular weight distribution. The storage moduli G' and loss moduli G'' are used for mapping the PI sample onto the semi-flexible Kremer-Grest model. All the experimental data are shifted to temperature of $-35^\circ C$ by time-temperature superposition. G' and G'' of sample PI-30k are in good agreement with simulation data from the chain length $N = 93$ (Fig.3.36). The ratio of the loss and storage moduli is the tangent of the phase angle, called the loss tangent

$$\tan \delta = \frac{G''}{G'} \quad (3.32)$$

which is shown in Fig.3.37. The shift factors of frequency and stress from the simulations to the experiments were obtained by comparing the crossing point of

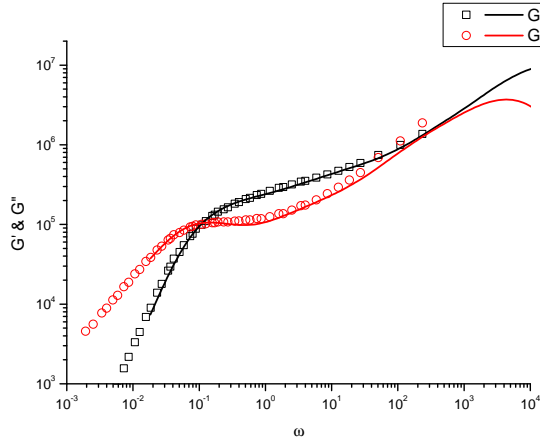


FIGURE 3.36: G' , G'' of PI-30k(symbols) in experiment and $N=93$ with $k_b=3$ (lines) in the simulation.

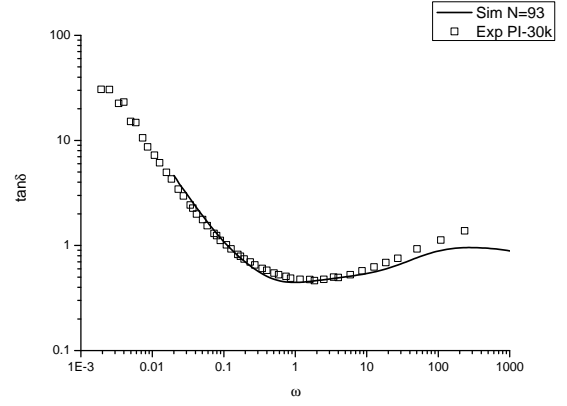


FIGURE 3.37: $\tan \delta$ of PI-30k(symbols) in experiments and $N = 93$ with $k_b = 3$ (lines) in the simulation.

G' and G'' at low frequencies,

$$1s \Rightarrow 8300\tau \quad (3.33)$$

$$1Pa \Rightarrow 1.48 \times 10^{-7} \varepsilon / \sigma^3 \quad (3.34)$$

where τ , ε and σ are the units of time, energy and length in the simulations.

The mapping coefficient between PI molecular weight in the experiment and number of beads of semi-flexible chains in the simulations is

$$\frac{M_e^{exp}}{N_e} = 0.36kg/mol \quad (3.35)$$

All the parameters of the simulations will be calculated from these three mapping coefficients.

The shear viscosity from the experiments and our simulations are shown in Fig.3.38-Fig.3.41. The Weissenberg numbers used in PI-2k and PI-4k samples are $W_i = \dot{\gamma}\tau_R$, and the ones used in PI-14k and PI-30k are determined by both τ_R and τ_d . The experiments of PI-2k(Fig.3.38) were taken at a different temperature ($T = -60^\circ C$) from the others, as the glass transition temperature T_g of PI-2k is higher than T_g of the longer molecules. Thus, a different mapping coefficient is used for this particular sample. The results show that the shear viscosity from

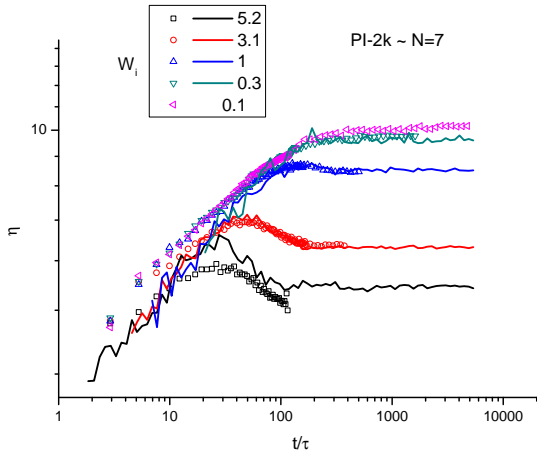


FIGURE 3.38: Comparing PI-2k shear experiments(symbols) with $N=7$ simulation results(lines) according to the same Weissenberg number.

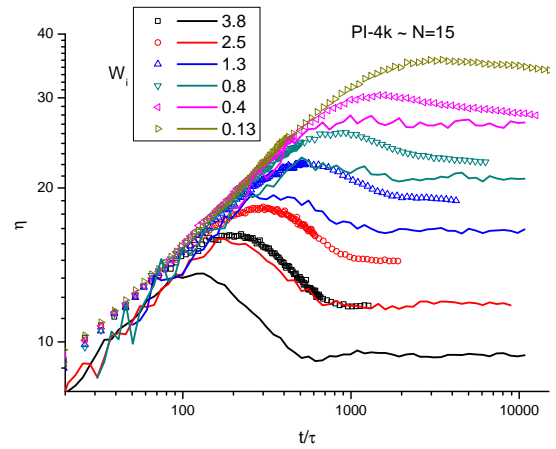


FIGURE 3.39: Comparing PI-4k shear experiments(symbols) with $N=15$ simulation results(lines) according to the same Weissenberg number.

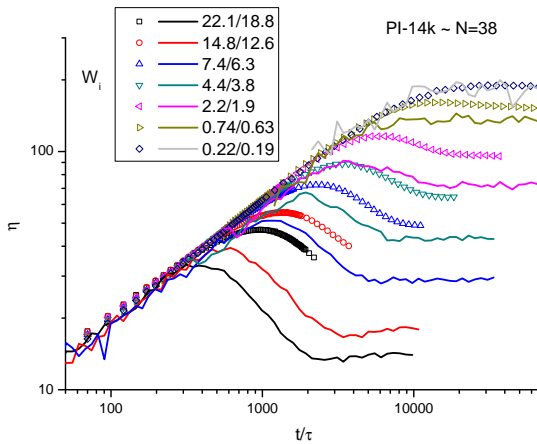


FIGURE 3.40: Comparing PI-14k shear experiments(symbols) with $N=38$ simulation results(lines) according to the same Weissenberg number.

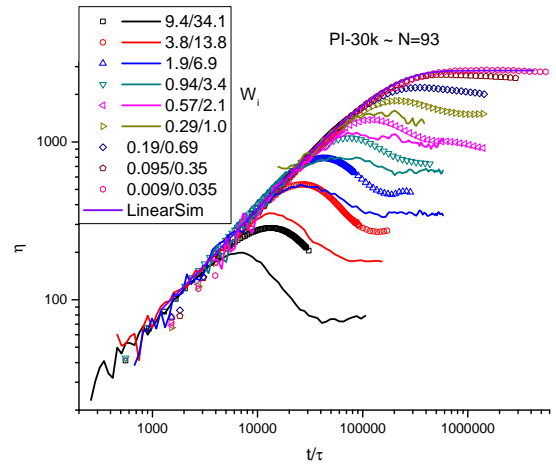


FIGURE 3.41: Comparing PI-30k shear experiments(symbols) with $N=93$ simulation results(lines) according to the same Weissenberg number.

simulations is in qualitative agreement with the viscosity from the experiments. We suppose the reason for some disagreement is that the local structures of PI and the semi-flexible Kremer-Grest model are different from each other. The semi-flexible KG model is more stiff than polyisoprene. We believe the results from flexible systems can be in better agreement with experiments which is a subject of future study. Another reason might be inaccurate mapping parameters. We note that for every new set of parameters new simulations must be performed, which makes it a very expensive procedure.

3.4 Conclusions

In this chapter we applied start-up shear in MD simulations by using Lees-Edwards boundary conditions. Comparing to the experiments, we did not suffer from the artefacts like wall slip, edge fracture and non-linear velocity profiles. Several thermostat methods were tested and constraint thermostat method was chosen to keep the temperature of the system consistent with the desired one. We covered the chain lengths from unentangled ($Z=0.5$) system to mildly entangled ($Z=10$). The properties of the material in both the transient and steady states were investigated. A careful averaging method was introduced for transient stresses to obtain reliable and accurate results. The shear stress, first and second normal stresses were measured as functions of time. As we know the first and second normal stresses are very difficult to measure in experiments. However, we can obtain accurate and reliable data by using these averaging methods. The results from linear regime in Chapter 2 were consistent with the shear data. Surprisingly, if we plot the shear stress σ_{xy} at steady state as a function of shear rate $\dot{\gamma}$, a maximum was observed at $\dot{\gamma} \approx 1/\tau_d$ for sufficiently long chains with $Z=10$, which probably means that the system is susceptible to shear banding. Cox-Merz rule was checked in our simulations. However, we found that it only works accurately for small molecular weights. Stress-optical law was also checked and it works at small shear rates and long times. A definition of mean path was introduced as an effective way to store trajectories. We will use these mean paths to analyze the dynamics of entanglements in shear in the future. We visualized the configurations of the chains in both the transient and steady states and chain tumbling was observed.

Then we tried to compare our rheological results with the experimental data from the literature. Although the chemical structures of the experimental sample and our simulation model are very different, we can relate these two by using mesoscopic variables, i.e. entanglement length or number of entanglements. The mapping coefficients between the experiments on polyisoprene and the simulations of semi-flexible chains were chosen carefully by comparing the storage and loss modulus of the samples. A qualitative agreement between the simulations and

experiments was obtained. We suppose the quantitative disagreement is due to different stiffness of PI sample and semi-flexible KG model. In order to obtain a quantitative agreement with the experiments, we will study the simulations of more flexible chains and improve our mapping procedures.

Chapter 4

Coarse-grained simulation of polymer melts

4.1 Overview

As we explained in chapter 1, the molecular dynamics(MD) simulations are not suited to the study of phenomena which occur on time and length scales that are far beyond the molecular scales due to the limit of computer power and the large number of particles. Normally we have to reduce the number of degrees of freedom of the system. In MD simulations, we need positions and velocities of all particles which makes the number of degrees of freedom of the system equal to $6N_p$, where N_p is the number of the particles in the system. However, if one is only interested in the long time diffusive motion of one polymer chain in a melt, it is sufficient to know the position and the velocity of the center-of-mass of the chain instead of all particles of the chain. The reduction of the number of degrees of freedom is called coarse-graining in which a bead-spring chain is represented by a set of mesoscopic “blobs”. The aim of coarse-graining is to derive a reduced equation of motion that only needs the mesoscopic variables which describe the position and velocity of the coarse-grained “blobs”. Normally there are three contributions to the total force on the mesoscopic “blobs”. The first one is the thermodynamic force which

is the gradient of the free energy of the configuration of the mesoscopic “blobs”. Second is the dissipative force which indicates that the motion of the mesoscopic “blobs” is retarded by friction. The last is the thermal force due to the continual collision effect on the mesoscopic “blobs”. The dissipative and thermal forces must be related to each other to ensure that both forces do not alter the equilibrium ensemble distribution, which is stated by the fluctuation-dissipation theorem.

As far as static properties are concerned, the determination of effective interactions from microscopic models is one of the main challenges in this subject. In general one starts from experimental observables or quantities calculated from microscopic simulations and tries to reproduce these quantities by using some effective interactions. One such property is the radial distribution function $g(r)$, which can always be reproduced by a pair potential regardless of the actual potential from which it comes. Español *et al.*[64] studied the free energy of two predefined clusters in a simple liquid as a function of their separation which can be used as an effective pair interaction potential between these clusters if higher order correlations are ignored. Many algorithms have been proposed to obtain effective potentials from distribution functions. The simplest method is to use the effective interaction in the limit of low density where many-body effects can be neglected. A simulation with this effective potential can be used as the starting point of a series of iterations. In each iteration i , the difference between the objective interaction potential ($k_B T \ln g^0(r)$) and the one obtained from the i -th simulation ($k_B T \ln g^i(r)$) is used to predict a new potential $u^{i+1}(r) = u^i(r) - k_B T \ln(g^0(r)/g^i(r))$. Soper[65] applied this method to the radial distribution function of water from neutron scattering experiments and obtained consistent results with the experiment data. A modified hypernetted chain approximation was used by Reatto *et al.*[66] to obtain the potential of mean force of a hard-sphere system which involved many-body correlations. Van Gunsteren, Müller-Plathe *et al.*[67] developed an automatic adjustment of force field parameters during molecular dynamics simulations. Akkermans and Briels[68] investigated the effective Gaussian pair interactions between two blobs each being a coarse-grained polymer chain in the melt, which reproduces the radial

distribution function of the microscopic system. They introduced fitting parameters λ , and minimized a field ϕ_λ with respect to λ .

On the other hand, we need information about the dissipative and thermal forces for the dynamic properties. Normally the dissipative force is taken as a linear function of momenta for the microscopic particles. However, the friction coefficient of mesoscopic particles also depends on the configuration of particles, and it is important to account for both time and spatial dependency. Akkermans and Briels[69] coarse-grained one polymer chain in a melt to a single dimer of mesoscopic particles, called blobs. By using the projection operator formalism they separated the total force on the chain into the thermodynamic mean force, dissipative force and fluctuation force, and derived the equations of motion for the dimer. Dimer properties of the microscopic and the coarse-grained model were shown to be in reasonable agreement.

In this chapter, we only concentrate on the static properties of the polymer chains, so we make the dissipative and thermal forces of mesoscopic “blobs” independent of time and space. The whole chain was coarse-grained into a single “blob”, and we aim to study the interaction forces between the blobs rather than interaction potentials. In section 4.2, we introduce a method to derive the interaction force between two blobs called force projection method. In section 4.3 and 4.4, we will apply the force projection method between a single chain and a wall to derive the effective force on the blob from the wall. The distribution function of the blobs from a coarse-grained simulation is in good agreement with the one from the original microscopic simulation. Then we start to investigate the pairwise force and many-body effects between blobs. In section 4.5 and 4.6, the Kremer-Grest chains are investigated in vacuum and melts, respectively.

4.2 Force Projection Method

In the microscopic simulation, we project the force between two monomers belonging to different molecules onto the vector connecting the centers-of-mass of these

two molecules.

Suppose monomers i, j are two monomers which belong to two different molecules a, b respectively. \mathbf{f}_{ij} is the force between monomers i and j . $\mathbf{R}_a, \mathbf{R}_b$ are the coordinates of the center-of-mass of chains a and b . We then define a projection force \mathbf{f}_{ab} between blobs a and b as

$$\mathbf{f}_{ab}(|\mathbf{D}_{ab}|) = \sum_{i,j} \frac{\mathbf{f}_{ij} \cdot \mathbf{D}_{ab}}{|\mathbf{D}_{ab}|^2} \mathbf{D}_{ab}; \quad \forall i \in a, \forall j \in b \quad (4.1)$$

$$\mathbf{D}_{ab} = \mathbf{R}_a - \mathbf{R}_b \quad (4.2)$$

where \mathbf{D}_{ab} is the distance vector between blobs a and b . \mathbf{f}_{ab} and \mathbf{D}_{ab} have the same direction.

In this definition, we do not include the case when two monomers are in the same blob, which means the forces inside the blobs are not considered for this projection procedure. If we divide the molecules into several subchains and coarse-grain the monomers in one subchain into a blob, the projection force between these blobs of subchains will be very different from non-bonded one due to connectivity. In this work, we will study the projection force between non-bonded blobs first. Bonded blobs are left for the future study. Before using the projection procedure in Kremer-Grest microscopic simulation, we should assess if this method is reasonable or not. A Rouse chain is replaced by a blob between two walls and the distribution function of the center-of-mass of the Rouse chain between the walls in microscopic simulation is compared to the one from the coarse-grained simulation.

4.3 Rouse model between two walls

In the Rouse model, the excluded volume interaction and the hydrodynamic interaction are disregarded and the interaction potential is written as:

$$U(\{\mathbf{R}_i\}) = \frac{3k_B T}{2b^2} \sum_{i=0}^{N-1} (\mathbf{R}_{i+1} - \mathbf{R}_i)^2 \quad (4.3)$$

where b is the effective bond length, k_B is the Boltzmann constant and T is the temperature. In this model the Langevin equation becomes a linear equation for \mathbf{R}_n (Eqs. 1.46-1.48).

4.3.1 Microscopic simulation

In this simulation, two solid walls are placed at $x = -r_c$ and $x = 3\sqrt{Nb^2} + r_c$ to make sure that the chain rarely is affected by two walls at the same time. A Rouse chain is placed randomly between the walls. The pure repulsive Lennard-Jones potential with cut-off radius $r_c = 2^{1/6}\sigma$ is applied between the walls and the beads, but not between different beads like in Kremer-Grest model. The potential expressions on the walls are

$$\mathbf{U}_{wall_1} = \begin{cases} 4\epsilon \left[\left(\frac{\sigma}{R_x + r_c} \right)^{12} - \left(\frac{\sigma}{R_x + r_c} \right)^6 + \frac{1}{4} \right]; & R_x < 0. \\ 0; & R_x > 0. \end{cases} \quad (4.4)$$

$$\mathbf{U}_{wall_2} = \begin{cases} 4\epsilon \left[\left(\frac{\sigma}{R_x - 3\sqrt{Nb^2} - r_c} \right)^{12} - \left(\frac{\sigma}{R_x - 3\sqrt{Nb^2} - r_c} \right)^6 + \frac{1}{4} \right]; & R_x > 3\sqrt{Nb^2}. \\ 0; & R_x < 3\sqrt{Nb^2}. \end{cases} \quad (4.5)$$

where R_x is the x -component of the position \mathbf{R} of the bead in the Rouse chain.

During this microscopic simulation, we measured the distribution function of the center-of-mass of the Rouse chain. The effective force between the chain and the walls is derived by using projection force method introduced in the previous section. As only one Rouse chain was involved, the forces between the beads of the Rouse chain and the walls are projected on the distance vectors \mathbf{D} , where \mathbf{D} is just the shortest distance from the center-of-mass to a wall.

Chain length $N=10$ was chosen for the first microscopic test run. The blob distribution function is shown by the red line in Fig. 4.1. We can see that the distribution function increases with increasing distance from the wall until $d \approx$

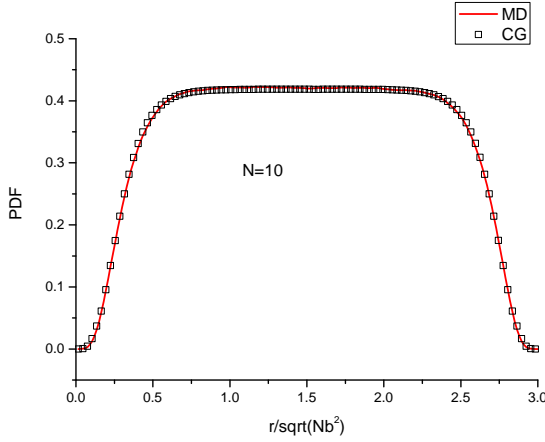


FIGURE 4.1: The center-of-mass distribution function of the Rouse chain between two walls in microscopic (red line) and coarse-grained (open symbols) simulation.

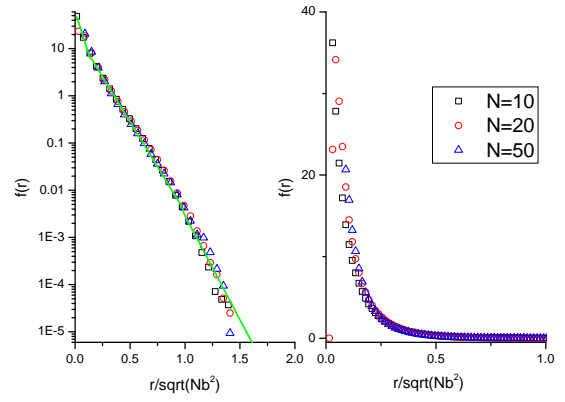


FIGURE 4.2: Projection force function $\mathbf{f}(r)$ of Rouse chain from solid wall in log-linear (left) and linear-linear (right) plots. The line is the best fit data which has the expression as Eq.(4.6).

$0.5\sqrt{Nb^2}$ and then reaches a plateau, which is reasonable because the size of the Gaussian chain is around $\sqrt{Nb^2}$. Then the radius of the Gaussian chain is around $0.5\sqrt{Nb^2}$, which means that if the distance between the center-of-mass of the Rouse chain and the wall is larger than $0.5\sqrt{Nb^2}$, the chain will rarely touch the wall. The effect from the wall should be negligible beyond this threshold.

The projection force function $\mathbf{f}(x)$ on the Rouse chain from the wall is shown in log-linear and linear-linear plots in Fig.4.2 for different chain lengths $N=10, 20$ and 50 . After scaling by the size of the chain, all three force functions collapse onto the same master curve. The green line is the best numerical fit which has the expression

$$f_{fit}(x) = \begin{cases} \exp(-16.537 \frac{x}{\sqrt{Nb^2}} + 4.1007); & 0 < \frac{x}{\sqrt{Nb^2}} < 0.13 \\ \exp(-8.7758 \frac{x}{\sqrt{Nb^2}} + 3.1228); & 0.13 < \frac{x}{\sqrt{Nb^2}} < 1.5 \\ 0; & \frac{x}{\sqrt{Nb^2}} > 1.5 \end{cases} \quad (4.6)$$

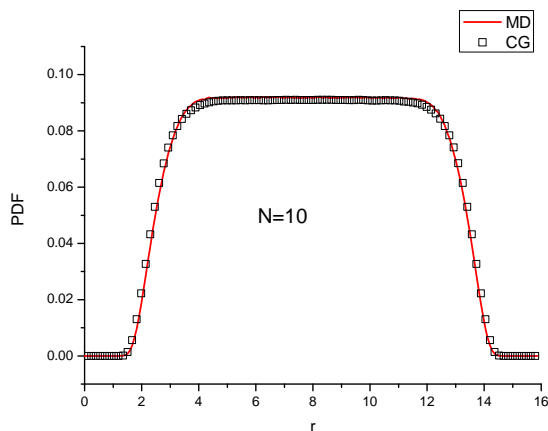


FIGURE 4.3: The center-of-mass distribution function of a Kremer-Grest chain between two walls from microscopic simulation (red line) and from coarse-grained simulation (open symbols).

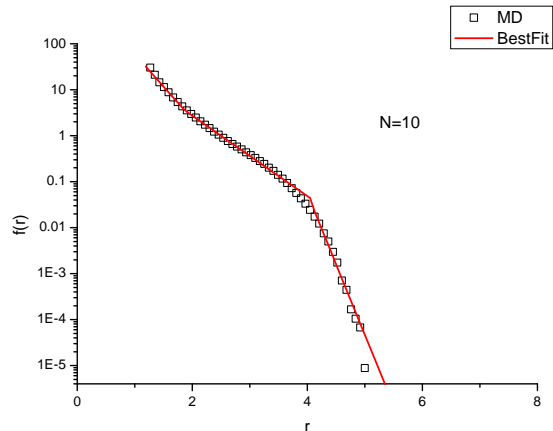


FIGURE 4.4: Magnitude of the projection force function $f(r)$ of Kremer-Grest chain from solid wall in log-linear plots. The line is the best fit data which has the expression as Eq.(4.8).

4.3.2 Coarse-grained simulation

Now we can use this best fit projection force $f_{fit}(x)$ in the coarse-grained simulation. A single particle is placed between the two walls. The potential from the wall was changed from Lennard-Jones potential to

$$U(x) = \int_0^x f_{fit}(x') dx'. \quad (4.7)$$

The obtained distribution function (open squares in Fig.4.1) is in excellent agreement with the one obtained from the original microscopic simulation. However, a Rouse chain is a random walk in space and there is no long range interaction between the beads which have large chemical distance. In next section we would like to ask whether this projection procedure is also valid for the Kremer-Grest model.

4.4 Single Kremer-Grest chain between two walls

Similar to the previous section, we place one Kremer-Grest chain with length $N=10$ instead of a Rouse chain between two walls separated by a distance of 16σ . The chain is not Gaussian in vacuum due to excluded volume effects, and the size

of the chain is larger than $\sqrt{Nb^2}$. As the beads repel each other and the bonds can not cross each other, the dynamics of Kremer-Grest model are different from the Rouse chain.

The distribution function was measured and is shown by red line in Fig.4.3. The force on the KG chain from the walls(symbols in Fig.4.4) was also measured by using projection force method. The best fit is shown by red line in Fig.4.4, where the numerical expressions are

$$f_{fit}(x) = \begin{cases} \exp(-3.2473x + 7.3307); & 0 < x \leq 1.9 \\ \exp(-2.0149x + 5.0317); & 1.9 < x \leq 4.05 \\ \exp(-7.0604x + 25.329); & 4.05 < x \leq 5.0 \\ 0; & x > 5.0 \end{cases} \quad (4.8)$$

Then we applied this best fit projection force $f_{fit}(x)$ to the coarse-grained simulation. The obtained distribution function(open squares in Fig.4.3) is in excellent agreement with the one from the original microscopic simulation.

From the previous two sections, we conclude that the local structure of the polymer chain does not affect the validity of this procedure, which indicates that the force projection method might be useful for reducing the number of degrees-of-freedom of the system.

4.5 Kremer-Grest model in vacuum

In the previous sections, we were using the force projection method to measure the force on the chain from the walls. Now we would like to study this method for pairs of Kremer-Grest chains in vacuum. The pure repulsive Lennard-Jones potential is chosen for the simulations.

Normally, the mean square internal distance function and the radius of gyration are the two common objective functions which describe the structure of the chains. The mean square internal distance function $\langle R^2(n) \rangle/n$ of chain length $N=100$

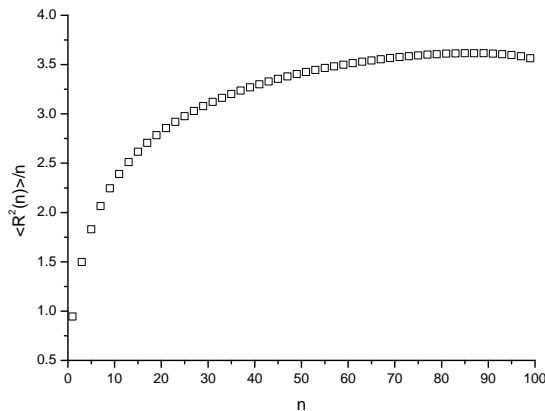


FIGURE 4.5: Mean square internal distance function of chain length $N = 100$ in vacuum.

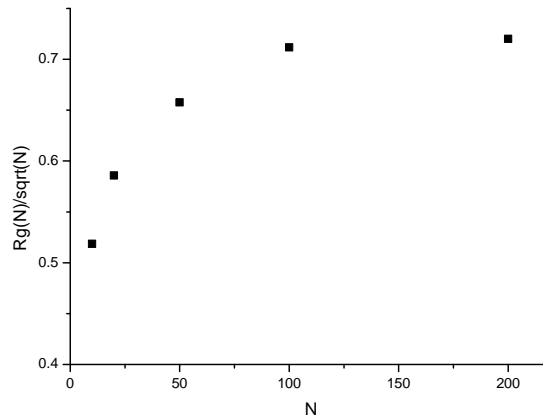


FIGURE 4.6: Radius of gyration of chains with different lengths in vacuum.

averaged over all segments of size $n = |i - j|$ along the chains is shown in Fig.4.5, where i and j are the indexes of two monomers. The figure starts from 0.93 which is the average of the square bond length, and then reaches a maximum around 3.6. It shows that the chain is not Gaussian in vacuum due to the excluded volume effect. The radius of gyration $R_g(N)$ of chains with different lengths in vacuum are shown in Fig.4.6. It has consistent results with the mean square internal distance function. We will use this for normalization in section 4.5.1.

First, we will measure the projection force function between two KG chains in section 4.5.1. Then many-body effects from other surrounding chains will be investigated in section 4.5.2.

4.5.1 Two chains model

We put two chains of the same length in the simulation box and fix the distance between the centers-of-mass of these two chains during the simulations by calculating the force between the two chains, then applying forces on each monomer whose sum has the same modulus but in opposite direction to make the total force on the whole chain to be zero. The average force between these two chains at each fixed distance was calculated over millions of time steps is called vacuum projection force(VPF). These vacuum projection forces for different chain lengths are shown in Fig.4.7. The results have several general features. The force becomes

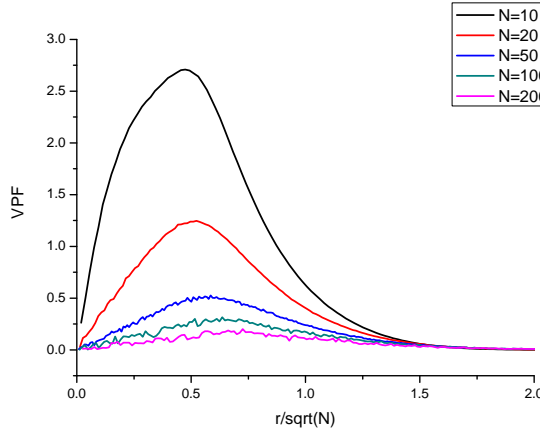


FIGURE 4.7: Vacuum projection force for different chain lengths.

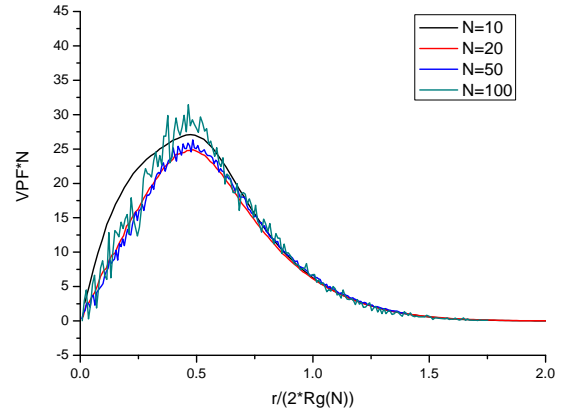


FIGURE 4.8: Normalized vacuum projection force for different chain lengths.

larger if the distance increases, reaches a maximal value around $r=0.5\sqrt{N}$ and then decreases to zero. We normalized the amplitude of VPF by the number of beads in the chain and the domain of VPF by the radius of gyration R_g of the chain in vacuum. The normalized forces are shown in Fig.4.8. The plots collapse onto a master curve for the length $N=20, 50, 100$. The disagreement between $N=10$ and the master curve means that the chain is too short to follow a universal behaviour.

The numerical expression of vacuum projection force \mathbf{f}_{VPF} can be fit as

$$\mathbf{f}_{VPF}(x) = \frac{x}{\sqrt{N}} \sum_{i=1}^4 A_i \exp \left[- \left(\frac{\frac{x}{\sqrt{N}} - B_i}{C_i} \right)^2 \right] \quad (4.9)$$

where parameters A_i , B_i and C_i are listed in Table.4.1.

	$N=10$			$N=20$		
i	A_i	B_i	C_i	A_i	B_i	C_i
1	9.4379	0	0.5989	3.2497	0	0.69241
2	4.6107	-0.026868	0.21659	0.55126	0.47303	0.23352
3	0.66398	0.50909	0.16858	-	-	-
4	0.058232	1.1547	0.34168	-	-	-

TABLE 4.1: Fitting parameter of vacuum projection force for chain length $N=10$ and $N=20$.

In section 4.7.2, we will show the radial distribution function of the blobs in the coarse-grained simulations by using this vacuum projection force, which is in

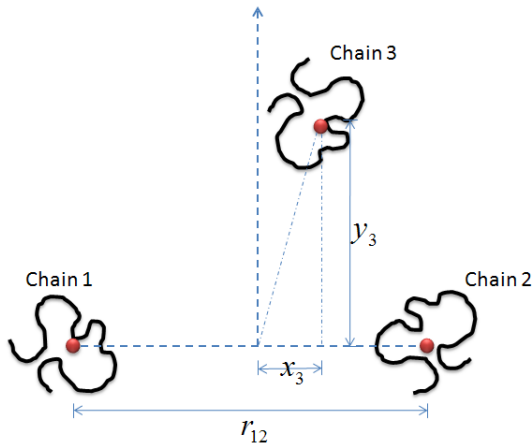


FIGURE 4.9: Three chains model.

good agreement with the original microscopic simulations at low densities but not in the system with high densities. The reason is that many-body effects play a significant role at high densities. Thus we would like to investigate the many-body effects starting from the three body effects.

4.5.2 Three chains model

In this section, we investigate how the force between two chains is affected by the presence of a third chain. Three chains are placed in the simulation box and the centers-of-mass of these chains are fixed. The projection force $f_{vac}(r_{12}; x_3, y_3)$ between first two chains is measured as a function of the position of the third chain, where r_{12} is the distance between first two chains, x_3, y_3 are the coordinates of the center-of-mass of the third chain in the plane going through these three centers-of-mass measured from the first two chains(Fig.4.9). After subtracting the vacuum projection force $f_{VPF}(r_{12})$ of the two chains model from the one in the three chains model, we can obtain how much a third chain affects the force between the pair of chains.

$$\Delta f_{vac}(r_{12}; x_3, y_3) = f_{vac}(r_{12}; x_3, y_3) - f_{VPF}(r_{12}) \quad (4.10)$$

In Fig.[4.10-4.17], we show the difference function $\Delta f_{vac}(r_{12}; x_3, y_3)$ between these two models. Chains 1 and 2 are both located on the x -axis and have the same distance away from the origin. These figures show several general features:

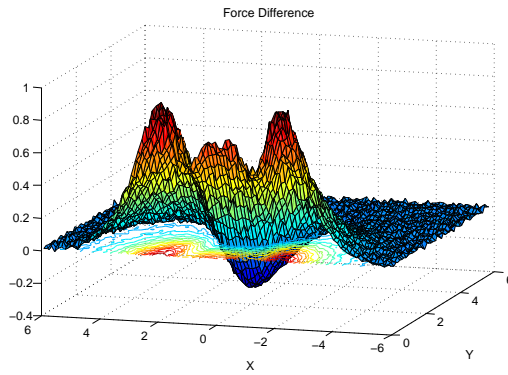


FIGURE 4.10: $\Delta f_{vac}(r_{12}; x_3, y_3)$ where $r_{12}=0.2\sigma$.

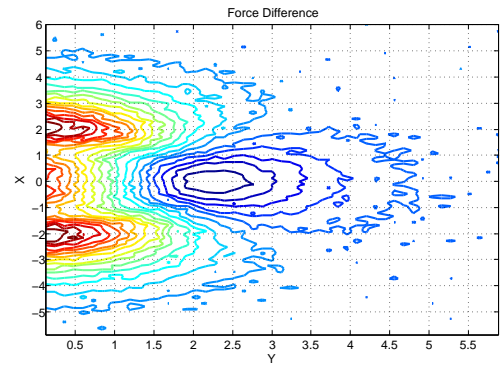


FIGURE 4.11: $\Delta f_{vac}(r_{12}; x_3, y_3)$ in contour where $r_{12}=0.2\sigma$.

- If the third chain is located between chains 1 and 2, the force between chains 1 and 2 becomes smaller. It can be explained by the fact that the third chain pushes chains 1 and 2 away from each other, which is called screening.
- If chains 1 and 2 are both on the same side of third chain, the force between chains 1 and 2 increases. It can be explained by the fact that the third chain pushes one chain towards the other and more collisions happen between monomers of chains 1 and 2.
- If the third chain is far away from these two chains, there is no effect from the third chain.
- In Fig.4.16, if the third chain is located at $x = \pm 3.0\sigma$ on x -axis, although two chains are on the same side of the third chain, the force difference is negative, which is in contradiction to the second feature above. We suppose that if we put the third chain at $x=3.0\sigma$, the shape of the chain at $x=1.5\sigma$ is more like an ellipse instead of a sphere as the center-of-mass of the chain is fixed. So the contacts between chains 1 and 2 decrease. Same arguments also applies to other r_{12} .

Based on all these figures, we conclude that three-body effect plays an important role in vacuum. Then we would like to ask a question, will the many-body effects act in a different way in the melt compared to the vacuum? In order to get the answers, we use the same strategy to calculate the projection forces in the melt.

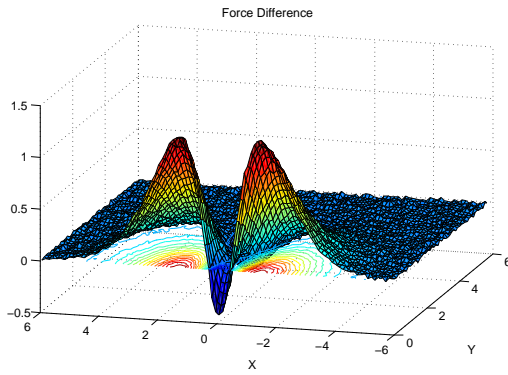


FIGURE 4.12: $\Delta f_{vac}(r_{12}; x_3, y_3)$ where $r_{12}=1.0\sigma$.

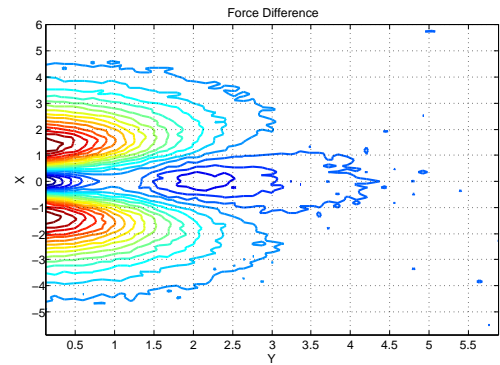


FIGURE 4.13: $\Delta f_{vac}(r_{12}; x_3, y_3)$ in contour where $r_{12}=1.0\sigma$.

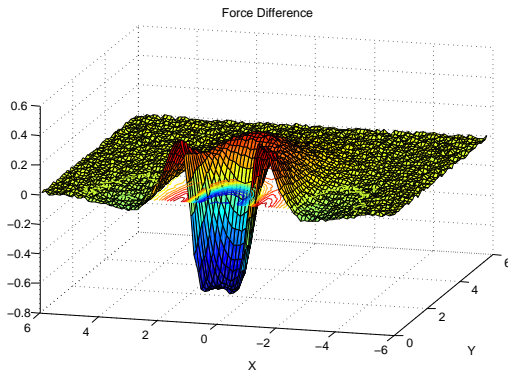


FIGURE 4.14: $\Delta f_{vac}(r_{12}; x_3, y_3)$ where $r_{12}=2.0\sigma$.

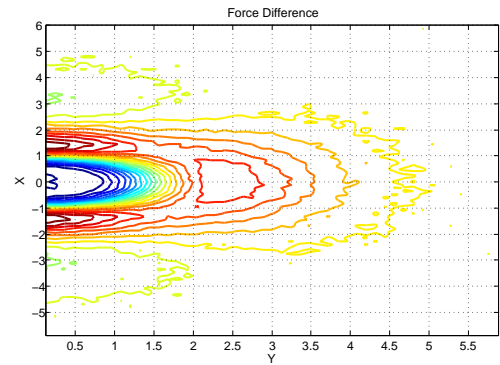


FIGURE 4.15: $\Delta f_{vac}(r_{12}; x_3, y_3)$ in contour where $r_{12}=2.0\sigma$.

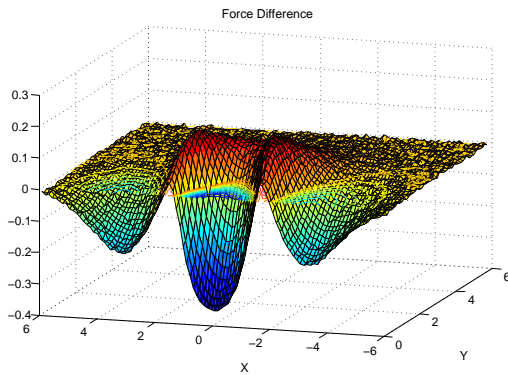


FIGURE 4.16: $\Delta f_{vac}(r_{12}; x_3, y_3)$ where $r_{12}=3.0\sigma$.

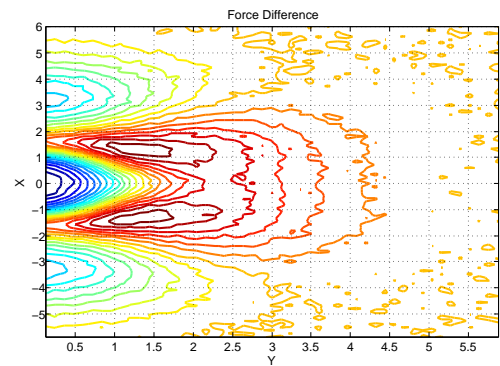


FIGURE 4.17: $\Delta f_{vac}(r_{12}; x_3, y_3)$ in contour where $r_{12}=3.0\sigma$.

4.6 Kremer-Grest model in the melt

4.6.1 Radius of gyration of chains in systems with different densities

First, we investigate some static properties of the polymer chains in the melts, like the radius of gyration and pressure at different densities. The values of $R_g(N)/\sqrt{N}$

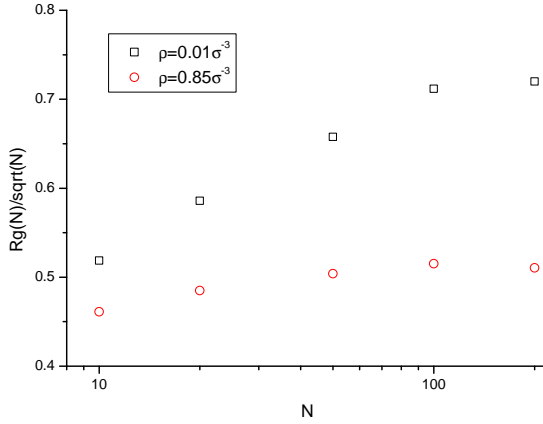


FIGURE 4.18: Radius gyration as a function of chain lengths.

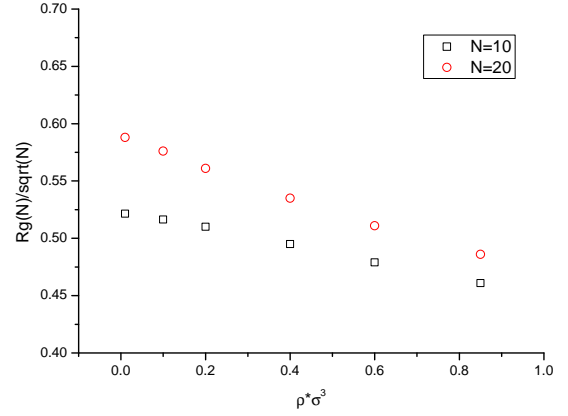


FIGURE 4.19: Radius gyration as a function of density of the system.

of different chain lengths are shown in Fig.4.18. $R_g(N)/\sqrt{N}$ increases with increasing chain length, and then reaches a plateau where the chain is long enough to follow Gaussian statistics which is contrast with the one in vacuum. This normalized radius of gyration decreases with increasing density. The radius of gyration at different densities will be used later to normalize the projection force obtained from the microscopic simulations. The pressure of the system is calculated by adding kinetic pressure and hydrostatic pressure together and is shown in Fig.4.25.

4.6.2 Projection force in the systems with different densities

We run microscopic simulations of Kremer-Grest model with chain length $N = 10$ (Fig.4.20) and $N = 20$ (Fig.4.22) in melts to obtain projection force between pairs of chains at different densities. Figs.4.20 and 4.22 show that the maximum of the projection force increases rapidly with increasing density as summarized in Fig.4.25. In order to find the relationship between the maximal force and the density of the system, the best fit data $f_{max}(\rho, N = 10)$, $f_{max}(\rho, N = 20)$ are derived by using the least square polynomial curve-fitting in these two cases(Lines in Fig.4.25). The expressions are

$$\mathbf{f}_{max}(\rho, N=10) = 34.0708\rho^3 - 10.1408\rho^2 + 4.0553\rho + 2.6342 \quad (4.11)$$

$$\mathbf{f}_{max}(\rho, N=20) = 35.3427\rho^3 - 10.9962\rho^2 + 4.7349\rho + 1.1279 \quad (4.12)$$

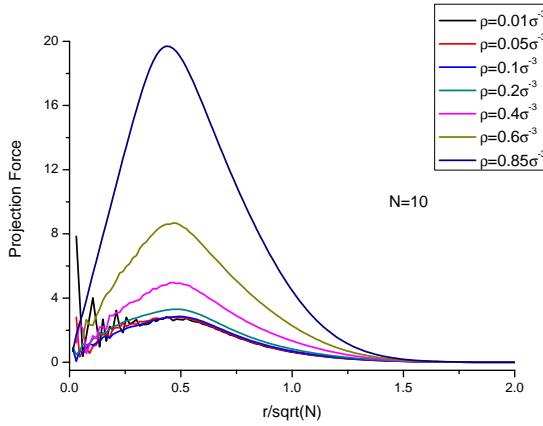


FIGURE 4.20: Projection force of $N=10$ at different densities.

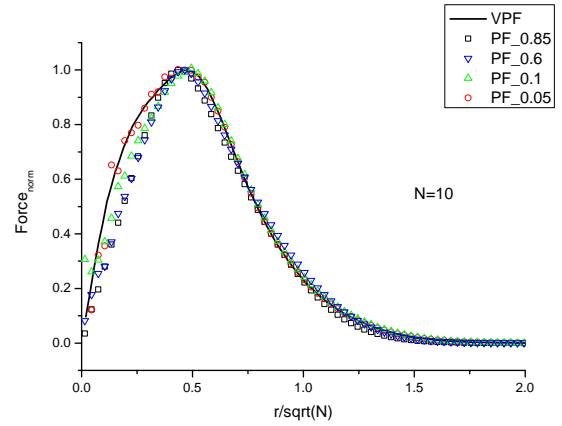


FIGURE 4.21: Normalized projection force of $N=10$ at different densities.

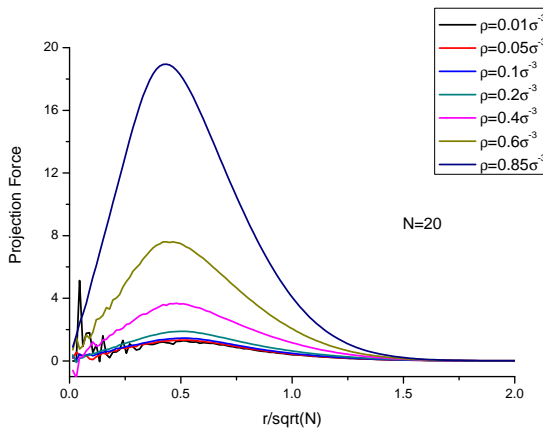


FIGURE 4.22: Projection force of $N=20$ at different densities.

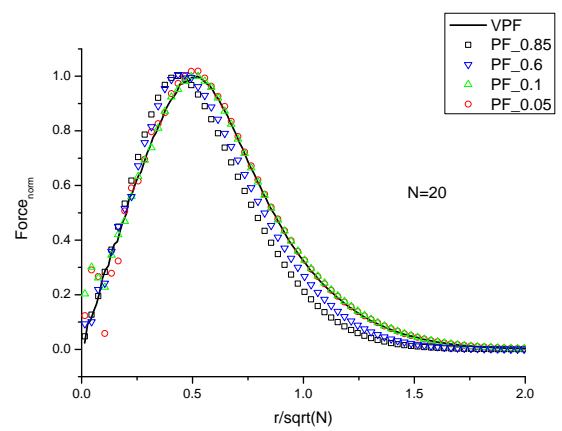


FIGURE 4.23: Normalized projection force of $N=20$ at different densities.

After normalizing these projection forces by their maximum in the system with chain length $N=10$ (Fig. 4.21), we can see that all results overlap with each other more or less at large distances. We suppose that the disagreement at short distances is due to the irregular shapes of two chains which are close to each other at low densities. It is clear that the force at density $\rho = 0.05\sigma^{-3}$ (red circles in Fig. 4.21) is consistent with the vacuum projection force (black line in Fig. 4.21). We can also see that the original projection force converges to the vacuum projection force $F_{VPF}(x)$ with decreasing density of the system (Fig. 4.20). However, there is a small disagreement around $r = 1.3\sqrt{N}\sigma$ in normalized forces. We suppose this disagreement is because the chain size is slightly smaller at high densities as compared with that at lower densities due to screening of excluded volume interactions at high densities.

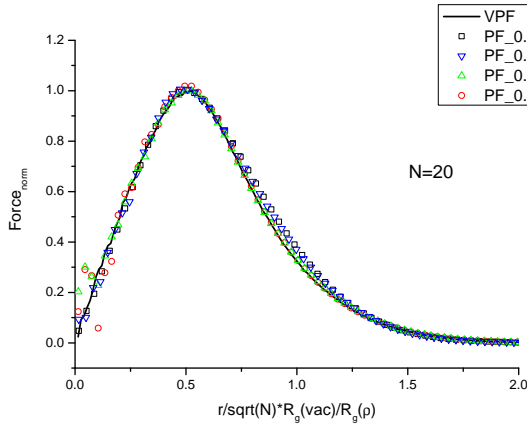


FIGURE 4.24: Shifted normalized projection force of $N=20$ at different densities.

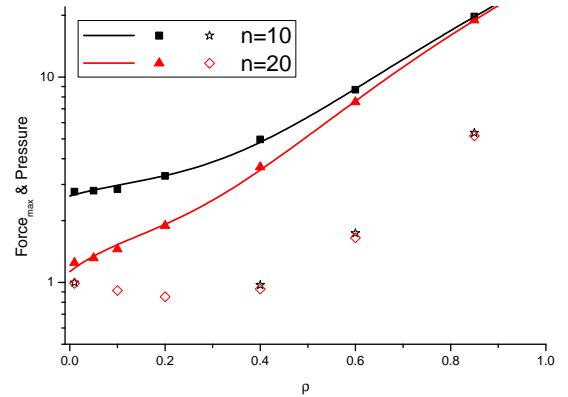


FIGURE 4.25: Maximum of projection force (solid symbols) and pressure (open symbols) at different densities. Lines are the best fit of the projection force maximum.

In the system with $N=20$, we can see that the normalized projection forces at low densities are exactly the same as the effective force in the vacuum, but it is not true at higher densities (Fig. 4.23). We suppose that the disagreement is due to the difference of the chain size at different densities. After multiplying a shift factor to the x -axis, we can overlap all these forces onto the vacuum projection force (Fig. 4.24). The shifting factors are 1.157 and 1.09 for $\rho = 0.85\sigma^{-3}$, $0.6\sigma^{-3}$ respectively, which are consistent with the radius of gyration of the chain at different densities (Fig. 4.19). We can see in Fig. 4.25 that the projection force maximum is proportional to the pressure at large densities. Because the chain size of $N=10$ does not heavily depend on the density of the system as the other large chain lengths, it is chosen for all the simulations in the later sections.

4.6.3 Three-body effects in the melt

In the next two sections we investigate many-body effects in melts. The density of the system is set to $0.85\sigma^{-3}$ unless stated otherwise. First of all, three-body effects are investigated. All chains move freely in the simulation box and none of the centers-of-mass are fixed as in the previous three chains model. Every triplet of chains was chosen to measure the force $f_{mel}(r_{12}; x_3, y_3)$ between the two chains

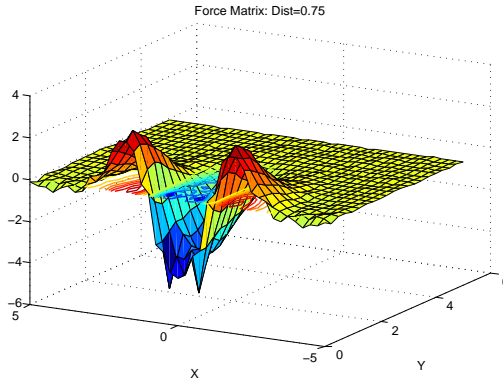


FIGURE 4.26: $\Delta f_{mel}(r_{12}; x_3, y_3)$ where $r_{12}=0.75\sigma$.

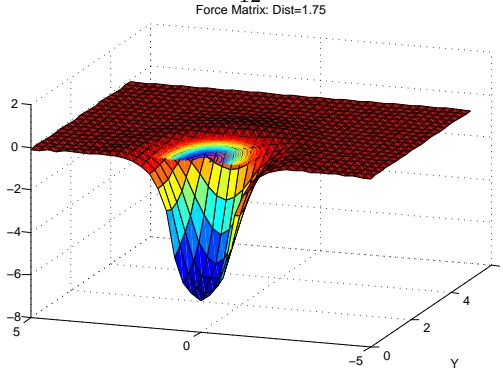


FIGURE 4.28: $\Delta f_{mel}(r_{12}; x_3, y_3)$ where $r_{12}=1.75\sigma$.

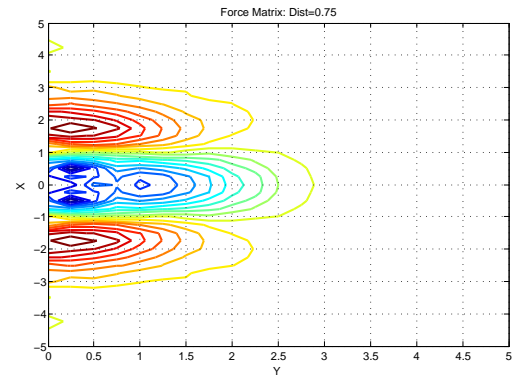


FIGURE 4.27: $\Delta f_{mel}(r_{12}; x_3, y_3)$ in contour where $r_{12}=0.75\sigma$.

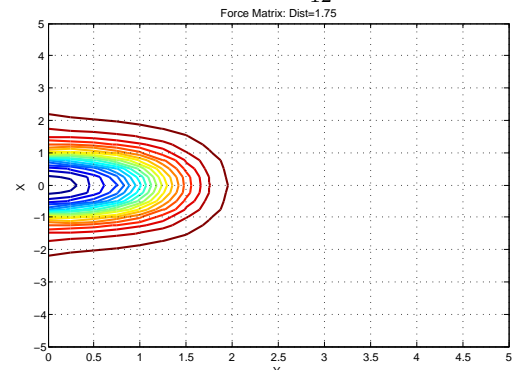


FIGURE 4.29: $\Delta f_{mel}(r_{12}; x_3, y_3)$ in contour where $r_{12}=1.75\sigma$.

where r_{12} is the distance between the two chains and (x_3, y_3) is the relative coordinates of the third chain with respect to the center of the other two chains. The difference function $\Delta f_{mel}(r_{12}; x_3, y_3)$ between $f_{mel}(r_{12}; x_3, y_3)$ and the one obtained from force projection method in the melt (dark blue line in Fig.4.20 and Fig.4.22) is shown in Figs.[4.26-4.35].

Comparing Fig.4.14 with Fig.4.28, we can see that the shapes of these two functions are similar, but the amplitude of the minimum in the melt (≈ 7) is much larger than the one in vacuum (≈ 0.6). This can be explained by the fact that polymer chains have more collisions and the pressure is higher in the melts than in vacuum, so the probe chain will be affected more by surrounding chains in the melt. And the affected range is more or less the same in both vacuum and melts ($\approx 4.0\sigma$).

Correction forces in the melt $\Delta f_{mel}(r_{12}; x_3, 0)$ are compared with the one from vacuum in Fig.4.36-4.39. The same r_{12} is chosen for each comparison and the data are scaled by making $\Delta f_{mel}(r_{12}; 0, 0)$ and $\Delta f_{vac}(r_{12}; 0, 0)$ both equal to -1 . If

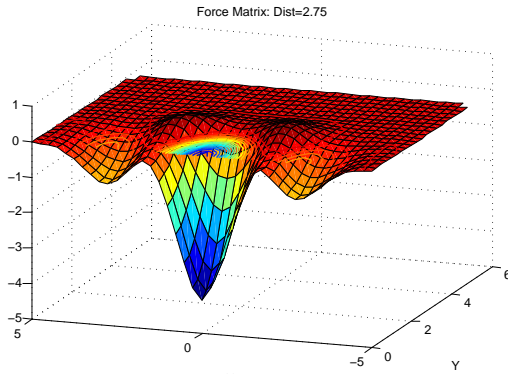


FIGURE 4.30: $\Delta f_{mel}(r_{12}; x_3, y_3)$ where $r_{12}=2.75\sigma$.

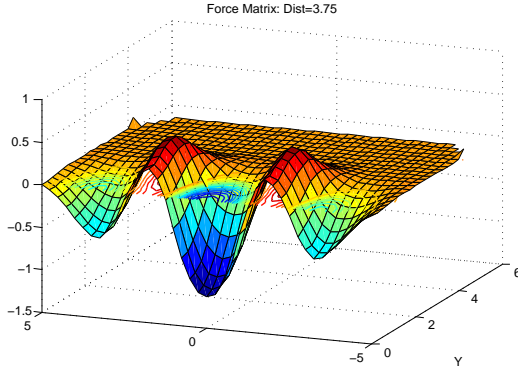


FIGURE 4.32: $\Delta f_{mel}(r_{12}; x_3, y_3)$ where $r_{12}=3.75\sigma$.

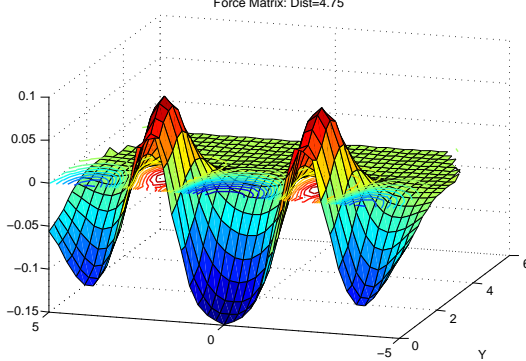


FIGURE 4.34: $\Delta f_{mel}(r_{12}; x_3, y_3)$ where $r_{12}=4.75\sigma$.

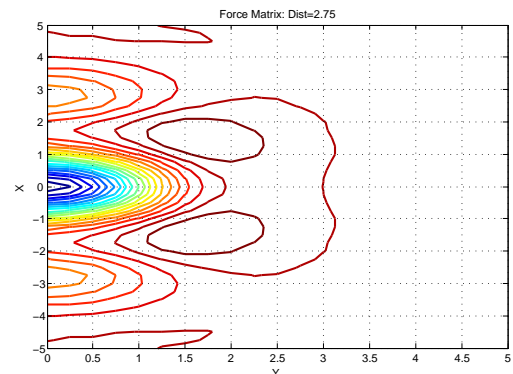


FIGURE 4.31: $\Delta f_{mel}(r_{12}; x_3, y_3)$ in contour where $r_{12}=2.75\sigma$.

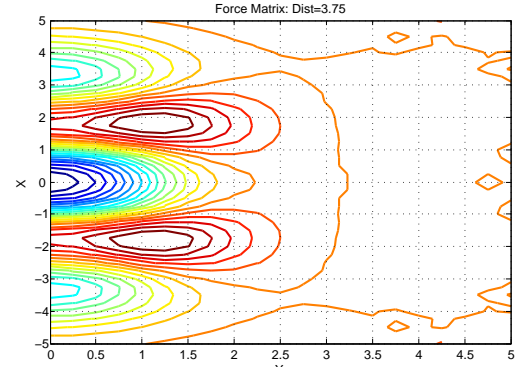


FIGURE 4.33: $\Delta f_{mel}(r_{12}; x_3, y_3)$ in contour where $r_{12}=3.75\sigma$.

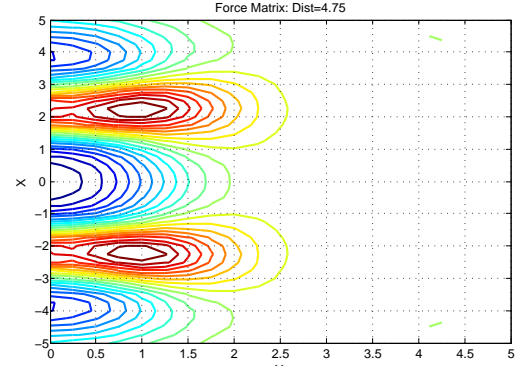


FIGURE 4.35: $\Delta f_{mel}(r_{12}; x_3, y_3)$ in contour where $r_{12}=4.75\sigma$.

$r_{12}=1.75\sigma$ in Fig.4.36, $\Delta f_{mel}(1.75; x_3, 0)$ has no maximum although there is a clear maximum in vacuum, which can be explained by the “screening” in the melts. We can also see that for large r_{12} the rescaled correction forces in the melts are quite similar to the one in vacuum.

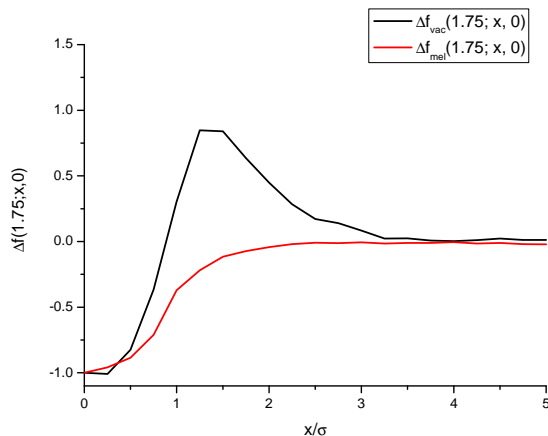


FIGURE 4.36: Three-body correction forces $\Delta f(1.75; x, 0)$ in vacuum and the melts.

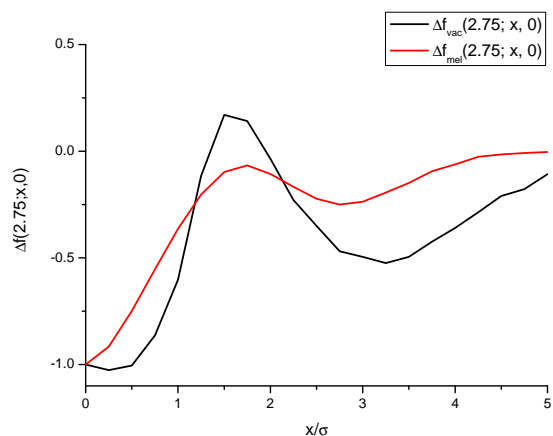


FIGURE 4.37: Three-body correction forces $\Delta f(2.75; x, 0)$ in vacuum and the melts.

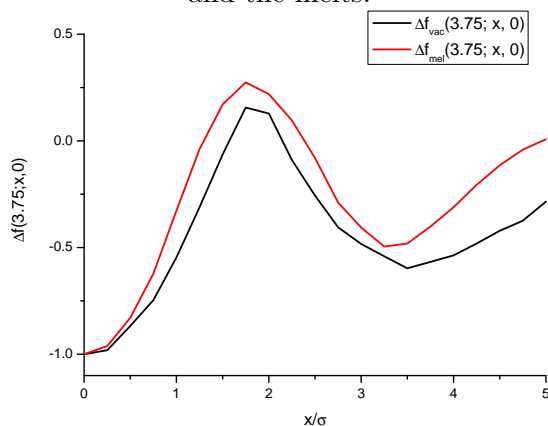


FIGURE 4.38: Three-body correction forces $\Delta f(3.75; x, 0)$ in vacuum and the melts.

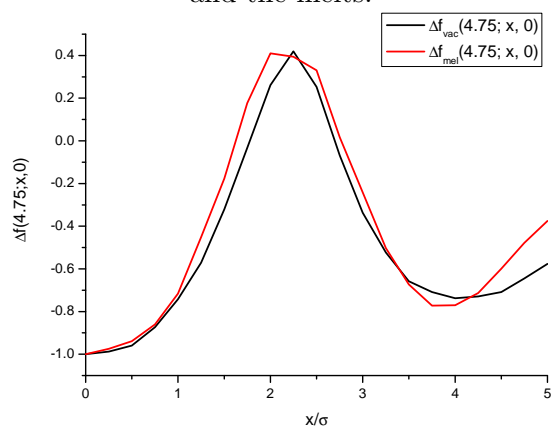


FIGURE 4.39: Three-body correction forces $\Delta f(4.75; x, 0)$ in vacuum and the melts.

4.6.4 Four-body effects

As there are more relative configurations of four bodies as compared with three bodies, we will only concentrate on one case of four-body effect in polymer melts in this section. We consider a case where chains 1 and 2 are fixed on the x -axis in the simulation box, whose centers-of-mass are 2.0σ away from each other and have the same distance from the point of origin, which means one is located at $(-1, 0, 0)$, and the other is located at $(1, 0, 0)$. Then we put both chains 3 and 4 on the x -axis too. The distance between the centers-of-mass of chains 3 and 4 is set to 2.5σ . During the simulation, we move chains 3 and 4 along the x -axis, which means the coordinates of the centers-of-mass of chains 3 and 4 are $(x'-1.25, 0, 0)$ and $(x'+1.25, 0, 0)$, where x' is the middle point between chains 3 and 4. Other chains move freely around these four chains. The force $f_{4b}(r_{12}; x_3, y_3, z_3, x_4, y_4, z_4)$

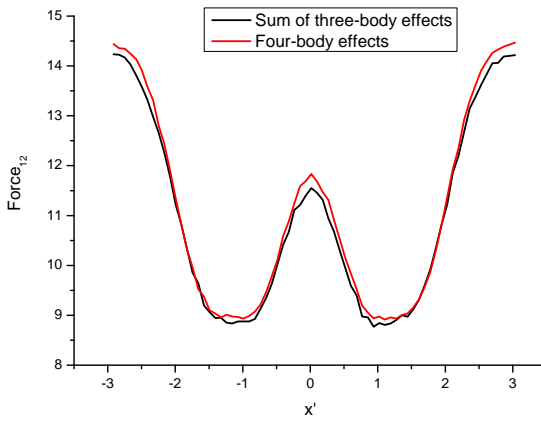


FIGURE 4.40: Four-body effects in polymer melt.

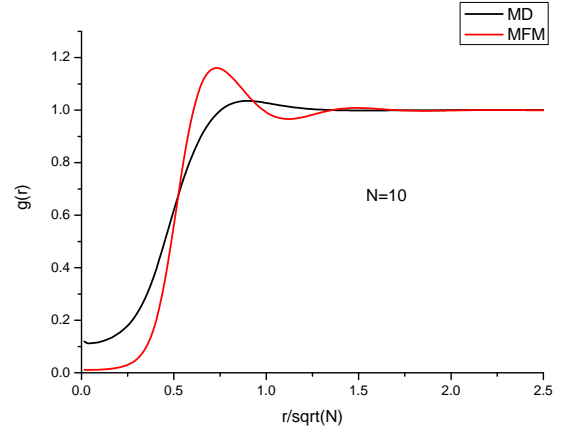


FIGURE 4.41: $g(r)$ obtained from MD simulation and from mean field method in coarse-grained simulation.

between chains 1 and 2 will be affected by the positions of chains 3 and 4 which is called the four-body effect. As all these four chain are on the x -axis, and the distance between chains 3 and 4 is fixed, the correction force function can be simplified to $\Delta f_{4b}(r_{12}; x'-1.25, 0, 0, x'+1.25, 0, 0)$. As the distance between chains 1 and 2 r_{12} is also fixed to 2σ , the force function depends only on one variable x' . We compare this result to the sum of two three-body effects which has the expression as following:(Fig.4.40)

$$\begin{aligned} & \Delta f_{mel}(r_{12}; x_3, 0) + \Delta f_{mel}(r_{12}; x_4, 0) \\ &= \Delta f_{mel}(r_{12}; x'-1.25, 0) + \Delta f_{mel}(r_{12}; x'+1.25, 0) \end{aligned}$$

These two curves overlap with each other quite well, which means that we can use three-body effects to approximate many-body effects in the melts. Now we have the effective interactions between two polymer chains from microscopic simulations. The question is can we apply these forces or potentials to the coarse-grained simulations to get a similar objective function $g(r)$ which is consistent with the one from the microscopic simulations.

4.7 Coarse-Grained Simulations in Melts

In this section, we will test different pairwise interactions between blobs and then add three-body effects into the coarse-grained simulations. The comparison of the radial distribution function of the blobs between original microscopic simulations and the coarse-grained simulations will be performed. In sections 4.7.1, 4.7.2 and 4.7.3, only pairwise interactions are studied. In section 4.7.4, three-body effects will be considered in the coarse-grained simulations.

4.7.1 Mean field method

The radial distribution function $g(r)$ of the center-of-mass of the polymer chains is calculated in microscopic MD simulations (black line in Fig.4.41). Each chain consists of 10 particles and the particle number density is $0.85\sigma^{-3}$. The mean field potential is obtained from $g(r)$ as

$$\varphi(r) = -\frac{1}{k_B T} \ln g(r) \quad (4.13)$$

where r is the distance between the center-of-mass of two chains. Then we introduce this mean field potential $\varphi(r)$ into our coarse-grained simulation. Normally, this mean field potential is a starting point of a series of iterations, but we did not repeat the iterations in this thesis. The radial distribution function $g(r)$ of the polymer chains in coarse-grained simulation is measured and plotted together with the one from the microscopic simulation in Fig.4.41. We can see that the two distribution functions are very different due to many-body effects in the melts. The mean field method provides a stronger pairwise interaction than it should be. Now we would like to apply our projection force from the vacuum and the melts to the coarse-grained simulations.

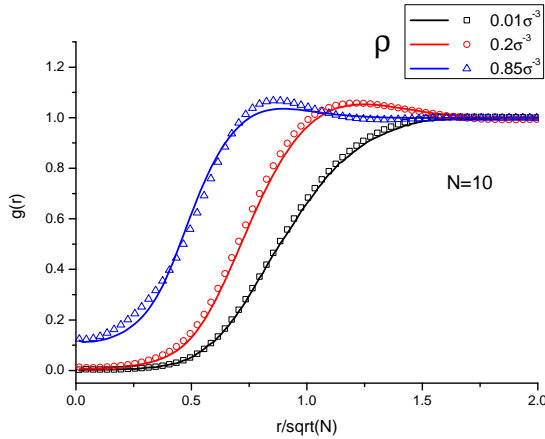


FIGURE 4.42: $g(r)$ from microscopic (lines) and coarse-grained (open symbols) simulations at different densities with $N=10$ by using vacuum projection force.

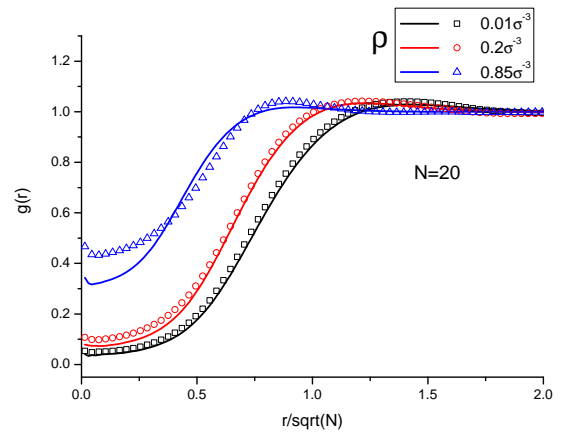


FIGURE 4.43: $g(r)$ from microscopic (lines) and coarse-grained (open symbols) simulations at different densities with $N=20$ by using vacuum projection force.

4.7.2 Vacuum projection force method

We use the projection force (Eq.4.9) in the vacuum from microscopic simulation to run the coarse-grained simulations at different densities ranging from $0.01\sigma^{-3}$ to $0.85\sigma^{-3}$. Corresponding $g(r)$ are shown in Fig.4.42 and Fig.4.43. From the microscopic simulations, $g(r)$ is a monotonically increasing function at low density (black lines in Figs.4.42 and 4.43). The chains tend not to overlap with each other at short distance. The range of the correlation hole is around $1.5\sqrt{N}$. If we increase the density of the system, $g(0)$ is not zero anymore which means that the chains start to overlap with each other and the maximum in $g(r)$ appears. The range of the correlation hole becomes smaller with increasing density. At lower densities, our vacuum projection force can reproduce $g(r)$ in coarse-grained simulations accurately, but $g(r)$ deviates from the one from microscopic simulation at high density $\rho=0.85\sigma^{-3}$ as the many-body effects start to play an important role. However, the agreement is quite good comparing to the mean field method even at high densities (Fig.4.41).

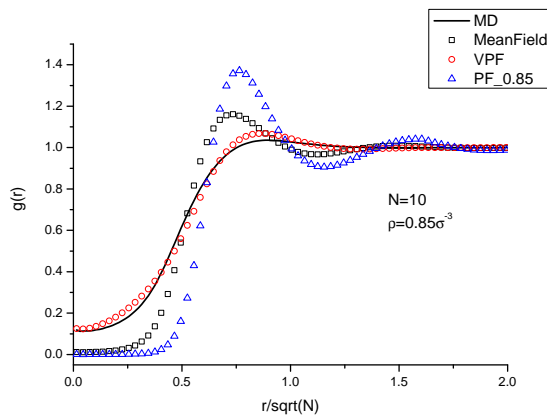


FIGURE 4.44: $g(r)$ in microscopic (line) and coarse-grained simulations. Square symbols are from mean field method. Circle symbols are from projection force in vacuum. Triangle symbols are from the projection force at $\rho=0.85\sigma^{-3}$.

4.7.3 Melts projection force method

In this section, we apply the force projection procedure at different densities with the same chain length ($N=10$). The forces are shown in Fig.4.20. We can see that the forces converge to the vacuum projection force as the density of the system decreases.

Now we would like to apply these projection forces to the coarse-grained simulations at the same system density where it was obtained. The $g(r)$ of the chains based on this projection force is plotted in Fig.4.44 together with the ones obtained from the mean field method, vacuum projection force method and the original microscopic simulations. The black line in Fig.4.44 is from microscopic simulation with $\rho=0.85\sigma^{-3}$. The symbols are from coarse-grained simulations with different methods. It shows that if we use the projection force obtained at $\rho=0.85\sigma^{-3}$ directly, the result is worse than that obtained using the vacuum projection force method. The reason is that the pressure of high density system is much larger than the pressure in the lower density system, which results in much higher forces. We conclude that the vacuum projection force is the best to reproduce the radial distribution function $g(r)$ if only pairwise interactions are considered.

4.7.4 Pairwise force plus three-body effects

In this section, we will try to add many-body effects into the coarse-grained simulations. In section 4.5.2, we showed the impact of the position of a third chain on the force between the two chains (Figs.[4.10-4.16]). We now introduce these force corrections into the coarse-grained simulations. The monomer density of the system is $0.85\sigma^{-3}$. We pre-calculate these force correction tables $\Delta f_{vac}(r_{12}; x_3, y_3)$ and $\Delta f_{mel}(r_{12}; x_3, y_3)$, where $r_{12} = \frac{i}{2} - \frac{1}{4}, i \in N, i \in [1, 10]$. In the new coarse-grained simulations, we select all triple chains and add force corrections to every chain.

$$f_1 = f_{pair}(r_{12}) + \Delta f(r_{12}; x_3, y_3) + f_{pair}(r_{13}) + \Delta f(r_{13}; x_2, y_2) \quad (4.14)$$

$$f_2 = f_{pair}(r_{23}) + \Delta f(r_{23}; x_1, y_1) + f_{pair}(r_{21}) + \Delta f(r_{21}; x_3, y_3) \quad (4.15)$$

$$f_3 = f_{pair}(r_{31}) + \Delta f(r_{31}; x_2, y_2) + f_{pair}(r_{32}) + \Delta f(r_{32}; x_1, y_1) \quad (4.16)$$

$\Delta f(r; x, y)$ is obtained by using linear interpolation of discrete force correction tables.

$$\Delta f(r_{12}; x_3, y_3) = \frac{\frac{2i+1}{4} - r_{12}}{1/2} \Delta f_{vac}\left(\frac{2i-1}{4}; x_3, y_3\right) + \frac{r_{12} - \frac{2i-1}{4}}{1/2} \Delta f_{vac}\left(\frac{2i+1}{4}; x_3, y_3\right) \quad (4.17)$$

where $\frac{2i-1}{4} \leq r_{12} \leq \frac{2i+1}{4}$.

The obtained radial distribution function $g(r)$ is shown in Fig.4.45 if the pairwise force and the three-body correction force are derived from vacuum. After introducing twice more fine-grained correction tables, we still got the same result. It shows that our correction force from the vacuum overestimates the many-body effects.

Then we would wonder whether the prediction will be better if we use the pairwise force and three-body correction force from the melt. The results are shown in Fig.4.46, demonstrating even larger discrepancy from the microscopic simulations. As the pressure in the melt is very different from the one in the vacuum, we would like to erase this effect from the melt. We have measured

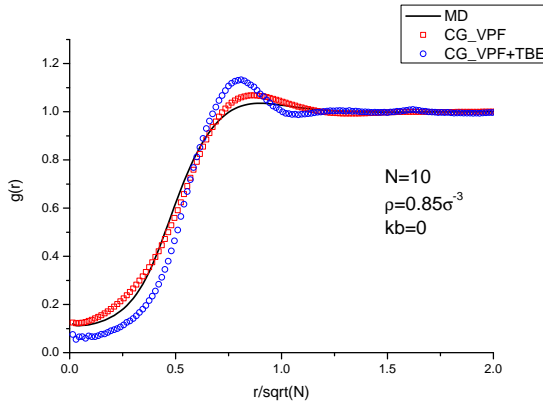


FIGURE 4.45: $g(r)$ in microscopic(line) and coarse-grained simulations with(blue circle) and without(red square) three-body effects from the vacuum.

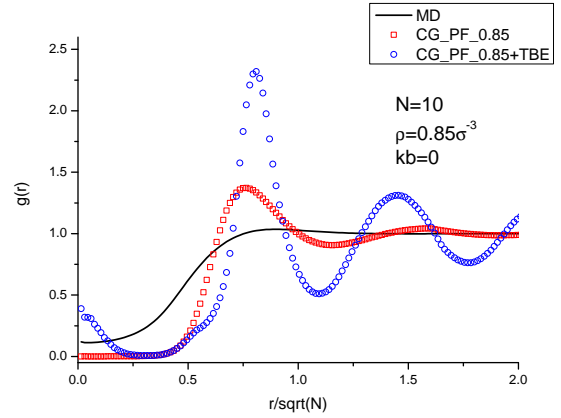


FIGURE 4.46: $g(r)$ in microscopic(line) and coarse-grained simulations with(blue circle) and without(red square) three-body effect from the melt.

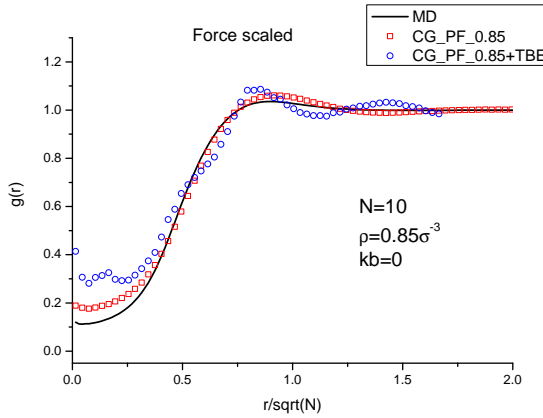


FIGURE 4.47: $g(r)$ in microscopic(line) and coarse-grained simulations with(blue circle) and without(red square) scaled three-body effects from the melts.

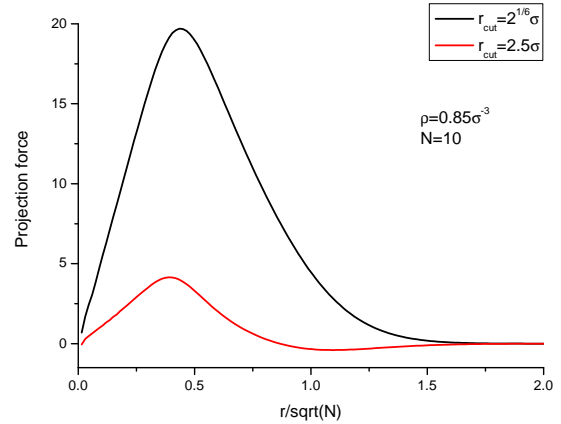


FIGURE 4.48: Projection force from pure repulsive Lennard-Jones potential(black line) and attractive Lennard-Jones potential(red line).

the pressure of the system at different densities in section 4.6.2, and derived the maximal pairwise force $f_{max}(\rho)$ as a function of the density. The forces at high densities can be scaled down to the same amplitude of the force in vacuum. In our case the scaling ratio is chosen to be $f_{max}(0.01)/f_{max}(0.85)=0.1375$ and is applied to both pairwise force and three-body correction force. The RHS of Eqs.(4.14)-(4.16) were multiplied by this scaling ratio. The coarse-grained simulation results are shown in Fig.4.47. Again, the three-body correction makes the agreement worse.

In order to erase the pressure effect from the system, we also tried to increase the cut-off length of Lennard-Jones potential to 2.5σ to introduce an attractive

part. The amplitude of projection force derived from this attractive system is smaller than in the purely repulsive system (Fig.4.48) and there is an attractive undershoot around $r \approx 1.0\sqrt{N}$. Furthermore $g(r)$ from both purely repulsive and attractive Lennard-Jones potentials are almost exactly the same. If we apply this force to the coarse-grained simulations, the system will be phase separated due to the attractive force.

We also applied Percus-Yevick and Hypernetted-chain closure to derive the pairwise potentials. We found that $g(r)$ in coarse-grained simulations using these potentials are exactly the same as the one from the mean field method. Derivation details are shown in Appendix B.

4.8 Conclusions

In this chapter, we have investigated the coarse-grained modelling of polymer melts. Blobs were introduced whose positions were defined as the center-of-mass of the whole chain. A procedure called force projection method was proposed to obtain the direct interaction force between the two molecules. First, we applied this method between a Rouse chain and two repulsive walls. The distribution of the chain between the walls and the force on the Rouse chain from the wall were calculated in microscopic simulations. Then we applied this force into coarse-grained simulations and obtained the same distribution function of the blobs as in the microscopic simulations, which indicates that the force projection method is a valid routine to coarse-grain the microscopic variables to mesoscopic variables. Then we replaced the Rouse chain by a single Kremer-Grest chain. The same conclusion was obtained, which means that in these simple situations the force projection method does not depend on the local structure of the chains.

Then we applied the force projection method to the two chains in vacuum to measure the direct interaction force between them as a function of their separation, which was called vacuum projection force in this thesis. This force was applied to coarse-grained simulations at different densities. $g(r)$ from these coarse-grained

simulations was in good agreement with the one from microscopic simulations even at high densities. Later on the three-body effects in vacuum were investigated and then added to the coarse-grained simulations. However, the inclusion of three-body effects did not improve the quality of $g(r)$. The force projection method and three-body effects were also investigated in melts. As the pressures were very different at different densities, we had tried to erase the effect due to pressure but still we can not improve $g(r)$ by simply adding the three-body contribution. Surprisingly, we found that in one example the four-body effect can be expressed as a sum of two three-body effects in the melts(Fig.4.40), which indicated that the many-body effect can be approximated by the three-body effect in the melts. Further study is still needed.

Chapter 5

Conclusions

In this thesis we investigated three different aspects of polymer dynamics using molecular dynamics simulations: orientation relaxation in equilibrium, shear flows and possible ways of coarse-graining.

5.1 Orientation relaxation in monodisperse and bidisperse melts

The Rouse[4] and tube theories[14][1] are regarded as successful theories to describe the dynamics of monodisperse unentangled and entangled linear polymers. However, both of them can not describe polydisperse melts perfectly. Thus a deep understanding of polydisperse melts is required in the field. We simulated the simplest polydisperse melts, i.e. binary blends of linear chains, and investigated the dynamics of different components. A universal time-dependent coupling parameter was derived to build the bridge between the monodisperse and bidisperse melts, which facilitates application of the theory of monodisperse melts to polydisperse samples.

5.2 Start-up shear in the melts

As discussed before there is no successful theory to describe dynamics of entangled polymers in non-linear regime. In this thesis the MD simulations were used to bridge the gap between experiments and future theories. Mapping coefficients between the experiments and our simulations were carefully chosen. A possible shear banding was observed in a mildly entangled system, which is in contradiction with experimental observation. In the thesis, we prescribe the velocity profile as a linear function of the distance to the origin, which allows us to measure the true bulk constitutive equations. However, the shear banding normally causes the non-linear velocity profiles. In future, a different algorithm[70] will be applied to compare with the current algorithm and directly observe shear banding in MD.

5.3 Coarse-grained simulations in the melts

All macroscopic properties of the material, i.e. pressure, temperature, etc., are related to the microscopic molecular properties, i.e. stress, kinetic energy, which means that if we want to understand the macroscopic properties, the investigation of small world is essential. However, due to the limit of computer power and number of particles, we normally can not predict a macroscopic measurement by using microscopic simulations, which encourages the development of coarse-graining procedures. A systematic method was developed in this thesis to derive the effective interaction forces between polymer chains in the melts. If we apply the pairwise interaction obtained from vacuum to the melts, a reasonable agreement between the original MD simulations and the coarse-grained simulations can be achieved. However, if many-body effects were introduced, the agreement became worse. Several effects were neglected in our procedure. In order to obtain a better agreement between simulations of two levels, we would like to add these effects back in the future work.

Appendix A

Normal modes

The main content in this appendix was derived in Doi and Edwards book[1]. In order to find the normal coordinates, we are using the linear transformation of $\mathbf{R}_n(t)$

$$\mathbf{X}_p(t) = \int_0^N \phi_{pn} \mathbf{R}_n(t) dn \quad (\text{A.1})$$

We need to choose ϕ_{pn} to make the equation of motion for $\mathbf{X}_p(t)$ to have the same formula as the Ornstein-Uhlenbeck processes

$$\xi_p \frac{\partial \mathbf{X}_p}{\partial t} = -k_p \mathbf{X}_p + \mathbf{f}_p \quad (\text{A.2})$$

From Eq.(1.49) and Eq.(A.2), we can see that

$$\begin{aligned} \xi_p \frac{\partial \mathbf{X}_p(t)}{\partial t} &= \xi_p \int_0^N dn \phi_{pn} \frac{\partial \mathbf{R}_n(t)}{\partial t} \\ &= \frac{\xi_p}{\xi} \int_0^N dn \phi_{pn} \left(k \frac{\partial^2 \mathbf{R}_n}{\partial n^2} + \mathbf{f}_n \right) \\ &= \frac{\xi_p}{\xi} \int_0^N dn \phi_{pn} \left(k \frac{\partial^2 \mathbf{R}_n}{\partial n^2} \right) + \frac{\xi_p}{\xi} \int_0^N dn \phi_{pn} \mathbf{f}_n \\ &= \frac{\xi_p}{\xi} \left(\left[\phi_{pn} k \frac{\partial \mathbf{R}_n}{\partial n} \right]_0^N - \int_0^N dn \frac{\partial \phi_{pn}}{\partial n} k \frac{\partial \mathbf{R}_n}{\partial n} \right) + \frac{\xi_p}{\xi} \int_0^N dn \phi_{pn} \mathbf{f}_n \end{aligned} \quad (\text{A.3})$$

By using Eq.(1.50)

$$\begin{aligned}
\xi_p \frac{\partial \mathbf{X}_p(t)}{\partial t} &= -\frac{\xi_p}{\xi} \int_0^N dn \frac{\partial \phi_{pn}}{\partial n} k \frac{\partial \mathbf{R}_n}{\partial n} + \frac{\xi_p}{\xi} \int_0^N dn \phi_{pn} \mathbf{f}_n \\
&= -\frac{\xi_p}{\xi} \left(k \frac{\partial \phi_{pn}}{\partial n} \mathbf{R}_n \Big|_0^N - \int_0^N dn k \frac{\partial^2 \phi_{pn}}{\partial n^2} \mathbf{R}_n \right) + \frac{\xi_p}{\xi} \int_0^N dn \phi_{pn} \mathbf{f}_n \\
&= -\frac{\xi_p}{\xi} k \frac{\partial \phi_{pn}}{\partial n} \mathbf{R}_n \Big|_0^N + \frac{\xi_p}{\xi} \int_0^N dn \left(k \frac{\partial^2 \phi_{pn}}{\partial n^2} \mathbf{R}_n + \phi_{pn} \mathbf{f}_n \right) \quad (\text{A.4})
\end{aligned}$$

The RHS of Eq.(A.2) can be expressed as following:

$$-k_p \mathbf{X}_p + \mathbf{f}_p = \int_0^N dn (-k_p \phi_{pn} \mathbf{R}_n) + \mathbf{f}_p \quad (\text{A.5})$$

From Eq.(A.4) and Eq.(A.5), the following equation is achieved:

$$-\frac{\xi_p}{\xi} k \frac{\partial \phi_{pn}}{\partial n} \mathbf{R}_n \Big|_0^N + \frac{\xi_p}{\xi} \int_0^N dn \left(k \frac{\partial^2 \phi_{pn}}{\partial n^2} \mathbf{R}_n + \phi_{pn} \mathbf{f}_n \right) = \int_0^N dn (-k_p \phi_{pn} \mathbf{R}_n) + \mathbf{f}_p \quad (\text{A.6})$$

For Eq.(A.6) to hold, we must have

$$-k_p \phi_{pn} = \frac{\xi_p}{\xi} k \frac{\partial^2 \phi_{pn}}{\partial n^2} \quad (\text{A.7})$$

$$\frac{\partial \phi_{pn}}{\partial n} \Big|_{n=0} = 0, \quad \frac{\partial \phi_{pn}}{\partial n} \Big|_{n=N} = 0 \quad (\text{A.8})$$

$$\mathbf{f}_p = \frac{\xi_p}{\xi} \int_0^N dn \phi_{pn} \mathbf{f}_n \quad (\text{A.9})$$

Eq.(A.7) and Eq.(A.8) define the eigenfunctions ϕ_{pn} . We can get the solution as following:

$$\phi_{pn} = \frac{1}{N} \cos\left(\frac{p\pi n}{N}\right) \quad (p = 0, 1, 2, \dots) \quad (\text{A.10})$$

and

$$k_p = \frac{\xi_p}{\xi} k \left(\frac{p\pi}{N}\right)^2 \quad (\text{A.11})$$

Now we can choose ξ_p such that \mathbf{f}_p satisfies $\langle \mathbf{f}_{p\alpha}(t) \mathbf{f}_{p\alpha}(0) \rangle = 2\xi_p k_B T \delta(t)$.

From Eq.(A.9)

$$\begin{aligned}
\langle \mathbf{f}_{p\alpha}(t) \mathbf{f}_{q\beta}(0) \rangle &= \frac{\xi_p \xi_q}{N^2 \xi^2} \int_0^N dn \int_0^N dm \cos\left(\frac{p\pi n}{N}\right) \cos\left(\frac{q\pi m}{N}\right) \langle \mathbf{f}_{n\alpha}(t) \mathbf{f}_{m\beta}(0) \rangle \\
&= \frac{\xi_p \xi_q}{N^2 \xi^2} \int_0^N dn \cos\left(\frac{p\pi n}{N}\right) \cos\left(\frac{q\pi n}{N}\right) 2\xi k_B T \delta_{\alpha\beta} \delta(t) \\
&= \frac{\xi_p^2}{N^2 \xi^2} (1 + \delta_{p0}) N \delta_{pq} \xi k_B T \delta_{\alpha\beta} \delta(t)
\end{aligned}$$

Thus the discrete and continuous normal coordinates for Rouse model are as follow:

$$\mathbf{X}_p = \frac{1}{N+1} \sum_{i=0}^N \mathbf{R}_i \cos\left(\frac{\pi p(i+1/2)}{N+1}\right) \quad (\text{A.12})$$

$$\mathbf{X}_p = \frac{1}{N} \int_0^N \mathbf{R}(i) \cos\left(\frac{\pi p i}{N}\right) di \quad (\text{A.13})$$

with inverse transformation

$$\mathbf{R}_i = \mathbf{X}_0 + 2 \sum_{p=1}^N \mathbf{X}_p \cos\left(\frac{\pi p(i+1/2)}{N+1}\right) \quad (\text{A.14})$$

$$\mathbf{R}_i = \mathbf{X}_0 + 2 \sum_{p=1}^N \mathbf{X}_p \cos\left(\frac{\pi p i}{N}\right) \quad (\text{A.15})$$

where p is the normal mode, and i is the bead number. Note that the zeroth mode $\mathbf{X}_0 = \frac{1}{N+1} \sum_{i=0}^N \mathbf{R}_i = \mathbf{R}_{cm}$ corresponds to the center of mass motion.

The equation of motion after transformation to normal coordinates is

$$\xi_p \frac{d\mathbf{X}_p}{dt} = -k_p \mathbf{X}_p + \mathbf{f}_p \quad (\text{A.16})$$

$$\langle \mathbf{f}_p(t) \mathbf{f}_q(t') \rangle = 6k_B T \xi_p \delta_{pq} \delta(t-t') \quad (\text{A.17})$$

where for the center of mass mode $\xi_0 = (N+1)\xi$ and $k_p = 0$, for all the other modes in case of discrete transformation $\xi_p = 2(N+1)\xi$ and $k_p = \frac{24k_B T(N+1)}{b^2} \sin^2\left(\frac{\pi p}{2(N+1)}\right)$.

This means that the spectrum of relaxation times is given by

$$\tau_p = \frac{\xi_p}{k_p} = \frac{\xi b^2}{12k_B T} \sin^{-2} \left(\frac{\pi p}{2(N+1)} \right); \quad p = 1 \dots N \quad (\text{A.18})$$

Thus, the longest relaxation time is

$$\tau_R = \tau_1 = \frac{\xi b^2}{12k_B T} \sin^{-2} \left(\frac{\pi}{2(N+1)} \right) \approx \frac{\xi b^2 (N+1)^2}{3\pi^2 k_B T} \quad (\text{A.19})$$

which is also called **Rouse time**.

Eq.(A.16) describes free diffusion of the center of mass and N independent Ornstein-Uhlenbeck processes. The formal solution of these equations are

$$\mathbf{X}_0(t) = \mathbf{X}_0(0) + \frac{1}{\xi_0} \int_0^t \mathbf{f}_0(t') dt' \quad (\text{A.20})$$

$$= \mathbf{X}_0(0) + \frac{1}{\xi_0} \int_0^t \sqrt{2k_B T \xi_0} d\mathbf{W}' \quad (\text{A.21})$$

$$\mathbf{X}_p(t) = \mathbf{X}_p(0) \exp\left(-\frac{t}{\tau_p}\right) + \frac{1}{\xi_p} \int_0^t \mathbf{f}_p(t') \exp\left(-\frac{t-t'}{\tau_p}\right) dt' \quad (\text{A.22})$$

$$= \mathbf{X}_p(0) \exp\left(-\frac{t}{\tau_p}\right) + \frac{1}{\xi_p} \int_0^t \sqrt{2k_B T \xi_p} \exp\left(-\frac{t-t'}{\tau_p}\right) d\mathbf{W}' \quad (\text{A.23})$$

And we can obtain the mean-square displacement of center-of-mass and the modes correlation function as following:

$$\langle (\mathbf{X}_0(t) - \mathbf{X}_0(0))^2 \rangle = \frac{2k_B T}{\xi(N+1)} t \quad (\text{A.24})$$

$$\langle \mathbf{X}_p(t) \mathbf{X}_q(t') \rangle = \delta_{pq} \frac{1}{24(N+1)} \sin^{-2} \left(\frac{\pi p}{2(N+1)} \right) \exp\left(-\frac{|t-t'|}{\tau_p}\right) \quad (\text{A.25})$$

This means that the time correlation function of the end-to-end vector $\mathbf{R}_e(t) = \mathbf{R}_N(t) - \mathbf{R}_0(t)$ is

$$\begin{aligned}
 \langle \mathbf{R}_e(t) \cdot \mathbf{R}_e(0) \rangle &= 16 \sum_{p=\text{odd}} \langle \mathbf{X}_p(t) \cdot \mathbf{X}_p(0) \rangle \\
 &= 16 \sum_{p=\text{odd}} \frac{3k_B T}{k_p} \exp\left(-\frac{t}{\tau_p}\right) \\
 &\approx Nb^2 \sum_{p=\text{odd}} \frac{8}{p^2 \pi^2} \exp\left(-\frac{p^2 t}{\tau_R}\right). \tag{A.26}
 \end{aligned}$$

Appendix B

Percus-Yevick and Hypernetted-chain closure

B.1 Ornstein-Zernike equation

In statistical mechanics the **Ornstein-Zernike equation** is an integral equation for defining the direct correlation function. It basically describes how the correlations between two molecules can be calculated.

It is convenient to define the total correlation function:

$$h(r_{12}) = g(r_{12}) - 1$$

which is a measure for the “influence” of molecule 1 on molecule 2 at distance r_{12} away with $g(r_{12})$ as the radial distribution function. In 1914 Ornstein and Zernike proposed to split this influence into two contributions, a direct and indirect part. The direct contribution is defined to be given by the direct correlation function, denoted $c(r_{12})$. The indirect part is due to the influence of molecule 1 on a third molecule, labeled 3, which in turn affects molecule 2, directly and indirectly. This indirect effect is weighted by the density and averaged over all possible positions

of particle 3. This decomposition can be written down mathematically as:

$$h(r_{12}) = c(r_{12}) + \rho \int c(r_{13})h(r_{32})dr_3 \quad (\text{B.1})$$

which is called **Ornstein-Zernike(OZ) equation**. The total correlation at r_{12} is the sum of a direct correlation plus an indirect contribution coming from all surrounding points.

The OZ equation has the interesting property that if one multiplies Eq.(B.1) by $e^{i\vec{k}\cdot\vec{r}_{12}}$ and integrate with respect to $d\vec{r}_1$ and $d\vec{r}_2$ one obtains:

$$\iint d\vec{r}_1 d\vec{r}_2 h(r_{12})e^{i\vec{k}\cdot\vec{r}_{12}} = \iint d\vec{r}_1 d\vec{r}_2 c(r_{12})e^{i\vec{k}\cdot\vec{r}_{12}} + \rho \iiint d\vec{r}_1 d\vec{r}_2 d\vec{r}_3 c(r_{13})e^{i\vec{k}\cdot\vec{r}_{12}} h(r_{23})$$

If we denote the Fourier transform of $h(r)$ and $c(r)$ by $\widehat{H}(k)$ and $\widehat{C}(k)$ this rearranges to

$$\widehat{H}(k) = \widehat{C}(k) + \rho\widehat{H}(k)\widehat{C}(k) \quad (\text{B.2})$$

from which we obtain that

$$\widehat{C}(k) = \frac{\widehat{H}(k)}{1 + \rho\widehat{H}(k)}$$

$$\widehat{H}(k) = \frac{\widehat{C}(k)}{1 - \rho\widehat{C}(k)}$$

And

$$\begin{aligned}
\widehat{H}(k) &= \int d\vec{r}_1 d\vec{r}_2 h(r_{12}) e^{i\vec{k}\cdot\vec{r}_{12}} = \int d\vec{r}_1 d\vec{r}_{12} h(r_{12}) e^{i\vec{k}\cdot\vec{r}_{12}} = V \int d\vec{r}_{12} h(r_{12}) e^{i\vec{k}\cdot\vec{r}_{12}} \\
&= V \int_0^{2\pi} d\varphi \int_0^\pi d\theta \int_0^{+\infty} h(r_{12}) e^{ik \cdot r_{12} \cos \theta} r_{12}^2 \sin \theta dr_{12} \\
&= 2\pi V \int_0^{+\infty} dr_{12} \int_0^\pi h(r_{12}) e^{ik \cdot r_{12} \cos \theta} r_{12}^2 \sin \theta d\theta \\
&= 2\pi V \int_0^{+\infty} dr_{12} \int_0^\pi -h(r_{12}) e^{ik \cdot r_{12} \cos \theta} r_{12}^2 d \cos \theta \\
&= 2\pi V \int_0^{+\infty} dr \int_{-1}^1 h(r) e^{ik \cdot r \cdot y} r^2 dy = 2\pi V \int_0^{+\infty} h(r) r^2 dr \int_{-1}^1 e^{ik \cdot r \cdot y} dy \\
&= 2\pi V \int_0^{+\infty} h(r) r^2 \frac{e^{ikr} - e^{-ikr}}{ikr} dr = 4\pi V \int_0^{+\infty} h(r) r^2 \frac{\sin kr}{kr} dr \\
&= 4\pi V \int_0^{+\infty} h(r) r \frac{\sin kr}{k} dr = \frac{4\pi}{k} V \int_0^{+\infty} rh(r) \sin kr dr \\
&= \frac{4\pi}{k} V \mathcal{F}_{\sin}(rh(r))
\end{aligned} \tag{B.3}$$

where $\mathcal{F}_{\sin}(f(r)) = \int_0^{+\infty} f(r) \sin kr dr$ is a sin-Fourier transform of $f(r)$. Put Eq.(B.3) into Eq.(B.2), we get

$$\mathcal{F}_{\sin}(r \cdot c(r)) = \frac{\mathcal{F}_{\sin}(r \cdot h(r))}{1 + \frac{4\pi\rho}{k} \mathcal{F}_{\sin}(r \cdot h(r))} \tag{B.4}$$

B.2 Percus-Yevick equation

Percus-Yevick equation is a closure relation to solve the Ornstein-Zernike equation which relates the direct correlation function to the total correlation function. The direct correlation function represents the direct correlation between two particles in a system containing $N - 2$ other particles. It can be represented by

$$c(r) = g_{total}(r) - g_{indirect}(r)$$

where $g_{total}(r)$ is the radial distribution function, i.e. $g_{total}(r) = \exp\{-\beta\varphi(r)\}$ (with $\varphi(r)$ the potential of mean force, $\beta = 1/k_B T$) and $g_{indirect}(r)$ is the radial distribution function without the effective interaction potential $u(r)$ between pairs

included, i.e. we write $g_{indirect}(r) = \exp\{-\beta(\varphi(r) - u(r))\}$. Thus we can approximate $c(r)$ by

$$c(r) = e^{-\beta\varphi(r)} - e^{-\beta(\varphi(r)-u(r))} \quad (\text{B.5})$$

$$u(r) = \frac{1}{\beta} \ln \left[1 - \frac{c(r)}{h(r) + 1} \right] \quad (\text{B.6})$$

which means we can obtain effective interaction potential $u(r)$ if $h(r)$ and $c(r)$ are known.

B.3 Hypernetted-chain equation

Hypernetted-chain equation is also a closure relation to solve the Ornstein-Zernike equation which relates the direct correlation function to the total correlation function. By expanding $g_{indirect}(r)$ in the Eq.(B.5) and introducing the function

$$g(r) = h(r) + 1 = \exp\{-\beta\varphi(r)\} \quad (\text{B.7})$$

we can approximate $c(r)$ by writing:

$$\begin{aligned} c(r) &= e^{-\beta\varphi(r)} - 1 + \beta(\varphi(r) - u(r)) \\ &= g(r) - 1 - \ln g(r) - \beta u(r) \\ &= h(r) - \ln g(r) - \beta u(r) \\ &= h(r) - \ln(h(r) + 1) - \beta u(r) \end{aligned} \quad (\text{B.8})$$

$$u(r) = \frac{1}{\beta} [h(r) - \ln(h(r) + 1) - c(r)] \quad (\text{B.9})$$

which again means that we can obtain effective interaction potential $u(r)$ if $h(r)$ and $c(r)$ are known.

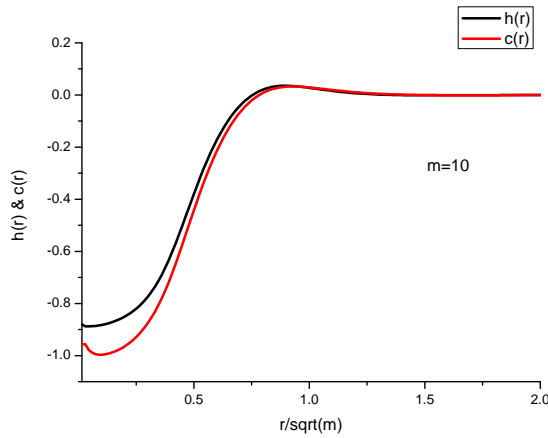


FIGURE B.1: $h(r)$ and $c(r)$ of the “blobs” in the system with $\rho = 0.85\sigma^{-3}$.

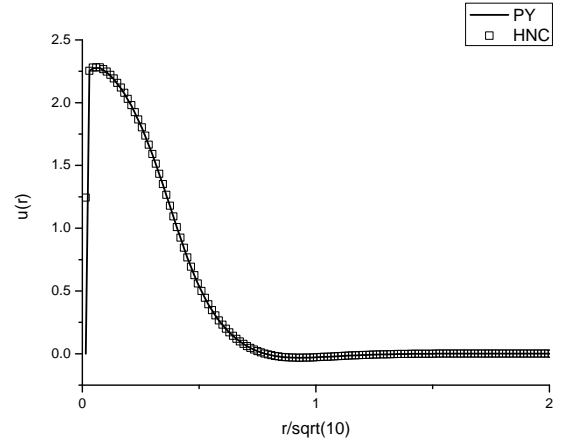


FIGURE B.2: Direct interaction potential in PY and HNC closure.

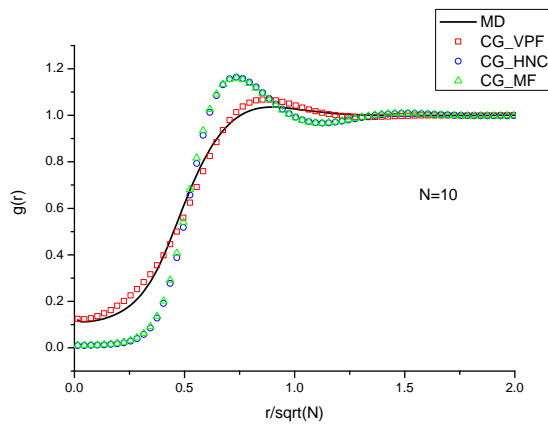


FIGURE B.3: $g(r)$ in microscopic simulation, coarse-grained simulation by using vacuum projection force, mean force and the potential obtained from HNC closure.

B.4 Coarse-grained simulation by using potentials obtained from PY and HNC closure

Now we try to get effective interaction potential for “blobs”. We can get $c(r)$ if $h(r)$ is known by using Eq.(B.4). $h(r)$ can be obtained from microscopic simulation. In Fig.B.1, we show $h(r)$ and $c(r)$ in the system with monomer density equal to $0.85\sigma^{-3}$. Thus, we can derive the direct interaction potential by using Eq.(B.6) and (B.9)(Fig.B.2). $g(r)$ in the coarse-grained simulation with this pairwise interaction is shown in Fig.B.3 together with the desired one. The result is exactly the same as the one from the mean field method in section 4.7.1, and is much worse than the one from the vacuum projection force method.

Bibliography

- [1] M. Doi and S. F. Edwards. *The Theory of Polymer Dynamics*. Oxford University Press, New York, USA, 1986.
- [2] M. Rubinstein and R. H. Colby. *Polymer Physics*. Oxford University Press, New York, USA, 2003.
- [3] Fima C Klebaner. *Introduction to Stochastic Calculus with Applications*. Imperial College Press, London, UK, 1998.
- [4] P. E. Rouse. A theory of the linear viscoelastic properties of dilute solutions of coiling polymers. *J. Chem. Phys.*, 21(7):1272–1280, 1953. doi: 10.1063/1.1699180. URL <http://link.aip.org/link/?JCP/21/1272/1>.
- [5] G. C. Berry and T. G. Fox. *Adv. Polym. Sci.*, 5(261), 1968.
- [6] R. H. Colby, L. J. Fetters, and W. W. Graessley. Melt viscosity-molecular weight relationship for linear polymers. *Macromolecules*, 20:2226–2237, 1987.
- [7] P. G. de Gennes. Reptation of a polymer chain in the presence of fixed obstacles. *J. Chem. Phys.*, 55(2):572–579, 1971. doi: 10.1063/1.1675789. URL <http://link.aip.org/link/?JCP/55/572/1>.
- [8] M. Doi and S. F. Edwards. Dynamics Of Concentrated Polymer Systems .1. Brownian-Motion In Equilibrium State. *Journal of the Chemical Society-Faraday Transactions II*, 74(Part 10):1789–1801, 1978. ISSN 0300-9238.
- [9] W.W. Merrill, M. Tirrell, J-F. Tassin, and L. Monnerie. Diffusion and relaxation in oriented polymer media. *Macromolecules*, 22:896–908, 1989.

- [10] M DOI. EXPLANATION FOR THE 3.4 POWER LAW OF VISCOSITY OF POLYMERIC LIQUIDS ON THE BASIS OF THE TUBE MODEL. *JOURNAL OF POLYMER SCIENCE PART C-POLYMER LETTERS*, 19(5):265–273, 1981. ISSN 0887-6258.
- [11] B. D. Todd and Peter J. Daivis. Homogeneous non-equilibrium molecular dynamics simulations of viscous flow: techniques and applications. *MOLECULAR SIMULATION*, 33(3):189–229, 2007. ISSN 0892-7022. doi: {10.1080/08927020601026629}.
- [12] Kurt Kremer and Gary S. Grest. Dynamics of entangled linear polymer melts: A molecular-dynamics simulation. *J. Chem. Phys.*, 92(8):5057–5086, 1990. doi: 10.1063/1.458541. URL <http://link.aip.org/link/?JCP/92/5057/1>.
- [13] Rolf Auhl, Ralf Everaers, Gary S. Grest, Kurt Kremer, and Steven J. Plimpton. Equilibration of long chain polymer melts in computer simulations. *J. Chem. Phys.*, 119(24):12718–12728, 2003. doi: 10.1063/1.1628670. URL <http://link.aip.org/link/?JCP/119/12718/1>.
- [14] P. G. de Gennes. *Scaling Concepts in Polymer Physics*. Cornell University Press, 1979.
- [15] M DOI. EXPLANATION FOR THE 3.4-POWER LAW FOR VISCOSITY OF POLYMERIC LIQUIDS ON THE BASIS OF THE TUBE MODEL. *JOURNAL OF POLYMER SCIENCE PART B-POLYMER PHYSICS*, 21(5):667–684, 1983. ISSN 0887-6266.
- [16] M. Rubinstein and R. H. Colby. Self-consistent theory of polydisperse entangled polymers: Linear viscoelasticity of binary blends. *J. Chem. Phys.*, 89:5291–5306, 1988.
- [17] A. E. Likhtman and T. C. B. McLeish. Quantitative theory for linear dynamics of linear entangled polymers. *Macromolecules*, 35:6332–6343, 2002.

- [18] Alexei E. Likhtman. Single-chain slip-link model of entangled polymers: Simultaneous description of neutron spin-echo, rheology, and diffusion. *Macromolecules*, 38(14):6128–6139, 2005. doi: 10.1021/ma050399h. URL <http://pubs.acs.org/doi/abs/10.1021/ma050399h>.
- [19] R. C. Ball and T. C. B. McLeish. Dynamic dilution and the viscosity of star polymer melts. *Macromolecules*, 22:1911–1913, 1989.
- [20] ST Milner and TCB McLeish. Arm-length dependence of stress relaxation in star polymer melts. *MACROMOLECULES*, 31(21):7479–7482, OCT 20 1998. ISSN 0024-9297.
- [21] G MARRUCCI. RELAXATION BY REPTATION AND TUBE ENLARGEMENT - A MODEL FOR POLYDISPERSE POLYMERS. *JOURNAL OF POLYMER SCIENCE PART B-POLYMER PHYSICS*, 23(1):159–177, 1985. ISSN 0887-6266.
- [22] M DOI, WW GRAESSLEY, E HELFAND, and DS PEARSON. DYNAMICS OF POLYMERS IN POLYDISPERSE MELTS. *MACROMOLECULES*, 20(8):1900–1906, AUG 1987. ISSN 0024-9297.
- [23] M. J. Struglinski and W. W. Graessley. Effects of polydispersity on the linear viscoelastic properties of entangled polymers. 1. experimental observations for binary mixtures of linear polybutadiene. *Macromolecules*, 18:2630–2643, 1985.
- [24] XP Yang, SQ Wang, and H Ishida. A solution approach to component dynamics of A/B miscible blends. 1. Tube dilation, reptation, and segmental friction of polymer A. *MACROMOLECULES*, 32(8):2638–2645, APR 20 1999. ISSN 0024-9297.
- [25] XP Yang, A Halasa, WL Hsu, and SQ Wang. A solution rheology approach to component dynamics in A/B miscible blends. 2. Friction coefficients of polymers A and B. *MACROMOLECULES*, 34(24):8532–8540, NOV 20 2001. ISSN 0024-9297.

- [26] S. Wang, S.-Q. Wang, A. Halasa, and W.-L. Hsu. Relaxation dynamics in mixtures of long and short chains: Tube dilation and impeded curvilinear diffusion. *Macromolecules*, 36:5355–5371, 2003.
- [27] JL VIOVY, M RUBINSTEIN, and RH COLBY. CONSTRAINT RELEASE IN POLYMER MELTS - TUBE REORGANIZATION VERSUS TUBE DILATION. *MACROMOLECULES*, 24(12):3587–3596, JUN 10 1991. ISSN 0024-9297.
- [28] Zuowei Wang and Ronald G. Larson. Constraint release in entangled binary blends of linear polymers: A molecular dynamics study. *MACROMOLECULES*, 41(13):4945–4960, JUL 8 2008. ISSN 0024-9297. doi: {10.1021/ma800680b}.
- [29] Jorge Ramirez, Sathish K. Sukumaran, Bart Vorselaars, and Alexei E. Likhtman. Efficient on the fly calculation of time correlation functions in computer simulations. *JOURNAL OF CHEMICAL PHYSICS*, 133(15), OCT 21 2010. ISSN 0021-9606. doi: {10.1063/1.3491098}.
- [30] Alexei E. Likhtman, Sathish K. Sukumaran, and Jorge Ramirez. Linear viscoelasticity from molecular dynamics simulation of entangled polymers. *Macromolecules*, 40(18):6748–6757, 2007. doi: 10.1021/ma070843b. URL <http://pubs.acs.org/doi/abs/10.1021/ma070843b>.
- [31] C. M. Ylitalo, J. A. Kornfield, G. G. Fuller, and Dale S. Pearson. Molecular weight dependence of component dynamics in bidisperse melt rheology. *Macromolecules*, 24(3):749–758, 1991. doi: 10.1021/ma00003a019. URL <http://pubs.acs.org/doi/abs/10.1021/ma00003a019>.
- [32] Jorge Ramírez, Sathish K. Sukumaran, and Alexei E. Likhtman. Significance of cross correlations in the stress relaxation of polymer melts. *J. Chem. Phys.*, 126(24):244904, 2007. doi: 10.1063/1.2746867. URL <http://link.aip.org/link/?JCP/126/244904/1>.

- [33] M. Doi, D. Pearson, J. Kornfield, and G. Fuller. Effect of nematic interaction in the orientational relaxation of polymer melts. *Macromolecules*, 22(3):1488–1490, 1989. doi: 10.1021/ma00193a082. URL <http://pubs.acs.org/doi/abs/10.1021/ma00193a082>.
- [34] M. Doi and H. Watanabe. Effect of nematic interaction on the rouse dynamics. *Macromolecules*, 24(3):740–744, 1991. ISSN 0024-9297. doi: 10.1021/ma00003a017. URL <http://dx.doi.org/10.1021/ma00003a017>.
- [35] R. Graf, A. Heuer, and H. W. Spiess. Chain-order effects in polymer melts probed by $h1$ double-quantum nmr spectroscopy. *Phys. Rev. Lett.*, 80(26):5738–5741, 1998. doi: 10.1103/PhysRevLett.80.5738.
- [36] A. R. C. Baljon, G. S. Grest, and T. A. Witten. Simulations of induced orientation in stretched polymer melts. *Macromolecules*, 28(6):1835–1840, 1995. doi: 10.1021/ma00110a017. URL <http://pubs.acs.org/doi/abs/10.1021/ma00110a017>.
- [37] J. M. Deutsch and J. H. Pixley. Induced orientational effects in relaxation of polymer melts. *Phys. Rev. E*, 80(1):011803, Jul 2009. doi: 10.1103/PhysRevE.80.011803.
- [38] H. Watanabe. Viscoelasticity and dynamics of entangled polymers. *Prog. Polym. Sci.*, 24:12531403, 1999.
- [39] A. N. Semenov. Bond-Vector Correlation Functions in Dense Polymer Systems. *MACROMOLECULES*, 43(21):9139–9154, NOV 9 2010. ISSN 0024-9297. doi: {10.1021/ma101465z}.
- [40] LA ARCHER, YL CHEN, and RG LARSON. DELAYED SLIP AFTER STEP STRAINS IN HIGHLY ENTANGLED POLYSTYRENE SOLUTIONS. *JOURNAL OF RHEOLOGY*, 39(3):519–525, MAY-JUN 1995. ISSN 0148-6055.

- [41] J Sanchez-Reyes and LA Archer. Steady shear rheology of entangled polymer liquids: Implications of interfacial slip. *JOURNAL OF RHEOLOGY*, 46(5): 1239–1262, SEP-OCT 2002. ISSN 0148-6055. doi: {10.1122/1.1498283}.
- [42] T Schweizer and A Bardow. The role of instrument compliance in normal force measurements of polymer melts. *RHEOLOGICA ACTA*, 45(4):393–402, APR 2006. ISSN 0035-4511. doi: {10.1007/s00397-005-0056-0}. 2nd Annual European Rheology Conference (AERC 2005), Grenoble, FRANCE, APR 21-23, 2005.
- [43] P Tapadia and SQ Wang. Direct visualization of continuous simple shear in non-newtonian polymeric fluids. *PHYSICAL REVIEW LETTERS*, 96(1), JAN 13 2006. ISSN 0031-9007. doi: {10.1103/PhysRevLett.96.016001}.
- [44] Pouyan E. Boukany and Shi-Qing Wang. Shear Banding or Not in Entangled DNA Solutions. *MACROMOLECULES*, 43(17):6950–6952, SEP 14 2010. ISSN 0024-9297. doi: {10.1021/ma101267b}.
- [45] G. Marrucci. Dynamics of entanglements: A nonlinear model consistent with the cox-merz rule. *Journal of Non-Newtonian Fluid Mechanics*, 62(2-3):279 – 289, 1996. ISSN 0377-0257. doi: DOI:10.1016/0377-0257(95)01407-1. URL <http://www.sciencedirect.com/science/article/B6TGV-3TKMMG1-9/2/2e101e37ab46debf140bd02a9e434a05>.
- [46] G Marrucci and G Ianniruberto. Effect of flow on topological interactions polymers. *MACROMOLECULAR SYMPOSIA*, 117:233–240, MAY 1997. ISSN 1022-1360. NATO Advanced Research Workshop on Manipulation of Organization in Polymers Using Tandem Molecular Interactions, IL CIOCCO, ITALY, MAY 29-JUN 02, 1996.
- [47] G MARRUCCI and N GRIZZUTI. FAST FLOWS OF CONCENTRATED POLYMERS - PREDICTIONS OF THE TUBE MODEL ON CHAIN STRETCHING. *GAZZETTA CHIMICA ITALIANA*, 118(3):179–185, MAR 1988. ISSN 0016-5603.

- [48] D PEARSON, E HERBOLZHEIMER, N GRIZZUTI, and G MARRUCCI. TRANSIENT-BEHAVIOR OF ENTANGLED POLYMERS AT HIGH SHEAR RATES. *JOURNAL OF POLYMER SCIENCE PART B-POLYMER PHYSICS*, 29(13):1589–1597, DEC 1991. ISSN 0887-6266.
- [49] DW MEAD and LG LEAL. THE REPTATION MODEL WITH SEGMENTAL STRETCH .1. BASIC EQUATIONS AND GENERAL-PROPERTIES. *RHEOLOGICA ACTA*, 34(4):339–359, JUL-AUG 1995. ISSN 0035-4511.
- [50] A.W Lees and S.F Edwards. The computer study of transport processes under extreme conditions. *J. Phys. C*, 5:1921, 1972.
- [51] WG HOOVER, DJ EVANS, RB HICKMAN, AJC LADD, WT ASHURST, and B MORAN. LENNARD-JONES TRIPLE-POINT BULK AND SHEAR VISCOSITIES - GREEN-KUBO THEORY, HAMILTONIAN-MECHANICS, AND NON-EQUILIBRIUM MOLECULAR-DYNAMICS. *PHYSICAL REVIEW A*, 22(4):1690–1697, 1980. ISSN 1050-2947.
- [52] Denis J. Evans and G. P. Morriss. Non-newtonian molecular dynamics. *Computer Physics reports*, 1(6):297 – 343, 1984. ISSN 0167-7977. doi: DOI:10.1016/0167-7977(84)90001-7. URL <http://www.sciencedirect.com/science/article/B6X3V-46R022X-W/2/ade10d33775022ca919c30ba79f3288c>.
- [53] DJ EVANS and GP MORRISS. NONLINEAR-RESPONSE THEORY FOR STEADY PLANAR COUETTE-FLOW. *PHYSICAL REVIEW A*, 30(3): 1528–1530, 1984. ISSN 1050-2947.
- [54] Denis J. Evans and Gary P. Morriss. *Statistical Mechanics of NonEquilibrium Liquids*. Cambridge University Press, Academic Press, London, 1990.
- [55] AM KRAYNIK and DA REINELT. EXTENSIONAL MOTIONS OF SPATIALLY PERIODIC LATTICES. *INTERNATIONAL JOURNAL OF MULTIPHASE FLOW*, 18(6):1045–1059, NOV 1992. ISSN 0301-9322.

- [56] H. C. Andersen. Molecular dynamics simulations at constant pressure and/or temperature. *J. Chem. Phys.*, 72(4):2384–2393, 1980. doi: 10.1063/1.439486. URL <http://link.aip.org/link/?JCP/72/2384/1>.
- [57] P ESPANOL and P WARREN. STATISTICAL-MECHANICS OF DISSIPATIVE PARTICLE DYNAMICS. *EUROPHYSICS LETTERS*, 30(4):191–196, MAY 1 1995. ISSN 0295-5075.
- [58] EV MENEZES and WW GRAESSLEY. NON-LINEAR RHEOLOGICAL BEHAVIOR OF POLYMER SYSTEMS FOR SEVERAL SHEAR-FLOW HISTORIES. *JOURNAL OF POLYMER SCIENCE PART B-POLYMER PHYSICS*, 20(10):1817–1833, 1982. ISSN 0887-6266.
- [59] T Schweizer, J van Meerveld, and HC Ottinger. Nonlinear shear rheology of polystyrene melt with narrow molecular weight distribution - Experiment and theory. *JOURNAL OF RHEOLOGY*, 48(6):1345–1363, NOV-DEC 2004. ISSN 0148-6055. doi: {10.1122/1.1803577}.
- [60] Rodrigo E. Teixeira, Hazen P. Babcock, Eric S. G. Shaqfeh, and Steven Chu. Shear thinning and tumbling dynamics of single polymers in the flow-gradient plane. *Macromolecules*, 38(2):581–592, 2005. doi: 10.1021/ma048077l. URL <http://pubs.acs.org/doi/abs/10.1021/ma048077l>.
- [61] Pouyan E. Boukany, Orin Hemminger, Shi-Qing Wang, and L. J. Lee. Molecular Imaging of Slip in Entangled DNA Solution. *PHYSICAL REVIEW LETTERS*, 105(2), JUL 9 2010. ISSN 0031-9007. doi: {10.1103/PhysRevLett.105.027802}.
- [62] Richard S. Graham, Alexei E. Likhtman, Tom C. B. McLeish, and Scott T. Milner. Microscopic theory of linear, entangled polymer chains under rapid deformation including chain stretch and convective constraint release. *J. Rheol.*, 47(5):1171–1200, 2003. doi: 10.1122/1.1595099. URL <http://link.aip.org/link/?JOR/47/1171/1>.

- [63] Dietmar Auhl, Jorge Ramirez, Alexei E. Likhtman, Pierre Chambon, and Christine Fernyhough. Linear and nonlinear shear flow behavior of monodisperse polyisoprene melts with a large range of molecular weights. *JOURNAL OF RHEOLOGY*, 52(3):801–835, MAY-JUN 2008. ISSN 0148-6055. doi: {10.1122/1.2890780}.
- [64] P Espanol, M Serrano, and I Zuniga. Coarse-graining of a fluid and its relation with dissipative particle dynamics and smoothed particle dynamics. *INTERNATIONAL JOURNAL OF MODERN PHYSICS C*, 8(4):899–908, AUG 1997. ISSN 0129-1831. 6th International Conference on Discrete Models for Fluid Mechanics, BOSTON, MA, AUG 26-28, 1996.
- [65] AK Soper. Empirical potential Monte Carlo simulation of fluid structure. *CHEMICAL PHYSICS*, 202(2-3):295–306, JAN 15 1996. ISSN 0301-0104.
- [66] D LEVESQUE, JJ WEIS, and L REATTO. PAIR INTERACTION FROM STRUCTURAL DATA FOR DENSE CLASSICAL LIQUIDS. *PHYSICAL REVIEW LETTERS*, 54(5):451–454, 1985. ISSN 0031-9007.
- [67] CD BERWEGER, WF VANGUNSTEREN, and F MULLERPLATHE. FORCE-FIELD PARAMETRIZATION BY WEAK-COUPLED REENGINEERING SPC WATER. *CHEMICAL PHYSICS LETTERS*, 232(5-6):429–436, JAN 27 1995. ISSN 0009-2614.
- [68] Reinier L. C. Akkermans and W. J. Briels. A structure-based coarse-grained model for polymer melts. *J. Chem. Phys.*, 114(2):1020–1031, 2001. doi: 10.1063/1.1330744. URL <http://link.aip.org/link/?JCP/114/1020/1>.
- [69] Reinier L. C. Akkermans and W. J. Briels. Coarse-grained dynamics of one chain in a polymer melt. *J. Chem. Phys.*, 113(15):6409–6422, 2000. doi: 10.1063/1.1308513. URL <http://link.aip.org/link/?JCP/113/6409/1>.
- [70] Florian Müller-Plathe. Reversing the perturbation in nonequilibrium molecular dynamics: An easy way to calculate the shear viscosity of fluids. *Phys. Rev. E*, 59(5):4894–4898, May 1999. doi: 10.1103/PhysRevE.59.4894.